Relativistic Electron Beam Transport for Fast Ignition Relevant Scenarios

By

Larissa A. Cottrill

B.S., Nuclear and Radiological Engineering (2003)
Georgia Institute of Technology

SUBMITTED TO THE DEPARTMENT OF NUCLEAR SCIENCE AND ENGINEERING
IN PARTIAL FULFILLMENT OF THE REQUIREMENTS FOR THE DEGREE OF

DOCTOR OF PHILOSOPHY IN NUCLEAR SCIENCE AND ENGINEERING
AT THE
MASSACHUSETTS INSTITUTE OF TECHNOLOGY

FEBRUARY 2009

Signature of Author: _____

Larissa A. Cottrill
Department of Nuclear Science and Engineering
January 27, 2009

Certified by: _____

Kim Molvig
Professor of Nuclear Science and Engineering
Thesis Supervisor

Certified by: _____

Chikang Li
Research Scientist, Plasma Science and Fusion Center
Thesis Reader

Certified by: _____

Jacquelyn C. Yanch
Professor of Nuclear Science and Engineering
Chair, Department Committee on Graduate Students

Relativistic Electron Beam Transport for Fast Ignition Relevant Scenarios

By

Larissa A. Cottrill

Submitted to the Department of Nuclear Science and Engineering
on January 8, 2009 in Partial Fulfillment of the Requirements for the Degree of
Doctor of Philosophy in Nuclear Science and Engineering

ABSTRACT

A crucial issue surrounding the feasibility of fast ignition, an alternative inertial confinement fusion scheme, is the ability to efficiently couple energy from an incident short-pulse laser to a high-density, pre-compressed fuel core. Energy transfer will involve the generation and transport of a relativistic electron beam, which may be subject to a number of instabilities such as the two-stream, Weibel, and filamentary instabilities that act to inhibit energy transport. This research addressed these issues by investigating the three main phases of the electron transport process: hot electron generation in the cone and the extent of confinement along the cone surface, linear instability growth in the outer plasma corona, and the nonlinear saturated state in the inner plasma corona. Analytical and computational models were constructed to include relevant physics that had been excluded from previous models, such as kinetic and collisional effects, and included use of a sophisticated particle-in-cell code (LSP).

During the initial phase of transport, our simulation results showed that contrary to experimental claims, hot electron surface confinement is only a minor effect and the cone target angle is a minimal concern for design considerations. The discrepancy was attributed to a phenomenon known as escaping electrons and the enhanced intensity of electrons measured along the surface was attributed to target geometry, rather than surface confinement. The second phase of transport was modeled analytically with the Vlasov-Krook-Maxwell formulation, which included collisional effects, various assumed theoretical distributions, and a data fit obtained from a simulation of the laser-plasma interaction. Our primary results indicated that collisions generally suppress growth but do tend to enhance filamentary instability growth at some wavelengths; however, due to the large temperature of the data fit, the overall growth rates are relatively small for fast ignition considerations. Analysis of the saturated regime, including particle orbits, revealed similar conclusions that instabilities can be safely neglected for fast ignition conditions, especially in the high density region of the fuel, which would otherwise need to resolved at great computational expense.

Thesis Supervisor: Kim Molvig

Title: Professor of Nuclear Science and Engineering

Acknowledgements

First and foremost, I would like to thank Max Tabak for giving me the opportunity to pursue my thesis research at Lawrence Livermore National Laboratory. I will remain indebted to him for his patience, advice, and the countless hours he spent with me over the course of my thesis research. More importantly, though, I have and will always appreciate his continual support throughout my thesis, even when others turned their back on me.

I would like to thank Kim Molvig for agreeing to be my thesis advisor and also Chikang Li from the Plasma Science and Fusion Center for reading my thesis. I am also very grateful to Steven Lerman, Dean of Graduate students at MIT, for his time and effort in resolving my fellowship funding problems, which allowed me to finish my thesis undeterred.

There were a number of technical contributions to this thesis from the Short Pulse Theory Group and the PIC/LSP Group at LLNL and I would like to express my appreciation to its many contributors for their advice and technical support.

There are many others who have made notable contributions throughout the course of this thesis and are deserving of special thanks. In 2005 I, by some miracle, managed to pass my doctoral qualifying exams while immeasurable odds were stacked against me. This required more motivation than even I was normally accustomed to. I would credit Richard Town as being largely responsible for this success and will always be grateful for his extraordinary kindness, advice, and any and all knowledge he imparted to me. I would also like to thank Denise Hinkel for her support and advice, which I have continued to use on a regular basis and will always carry with me.

Lastly, I would like to thank Mark and Jessica Adams. I could not even begin to repay them for their advice and support over the course of my thesis in both good times and bad.

Table of Contents

List of Figures

List of Tables

Chapter 1

Introduction

1.1 The Case for Fusion Energy

The quest for an abundant and environmentally safe source of energy for future generations has existed in the scientific community for many years, but only in the last half century has this issue begun to pervade social, economic, and political arenas. Initially, mankind required energy only to sustain life, the sun being a sufficient source for the first 5-10 million years of human existence. However, secondary energy sources have gradually evolved throughout societies to not only help sustain life, but to also enhance it. Beginning with the first controlled fire, these energy sources have advanced in number and sophistication to match the growing demand and energy consumption of world populations. As a result, secondary energy sources have now become essential for the security and economic well-being of nations across the globe.

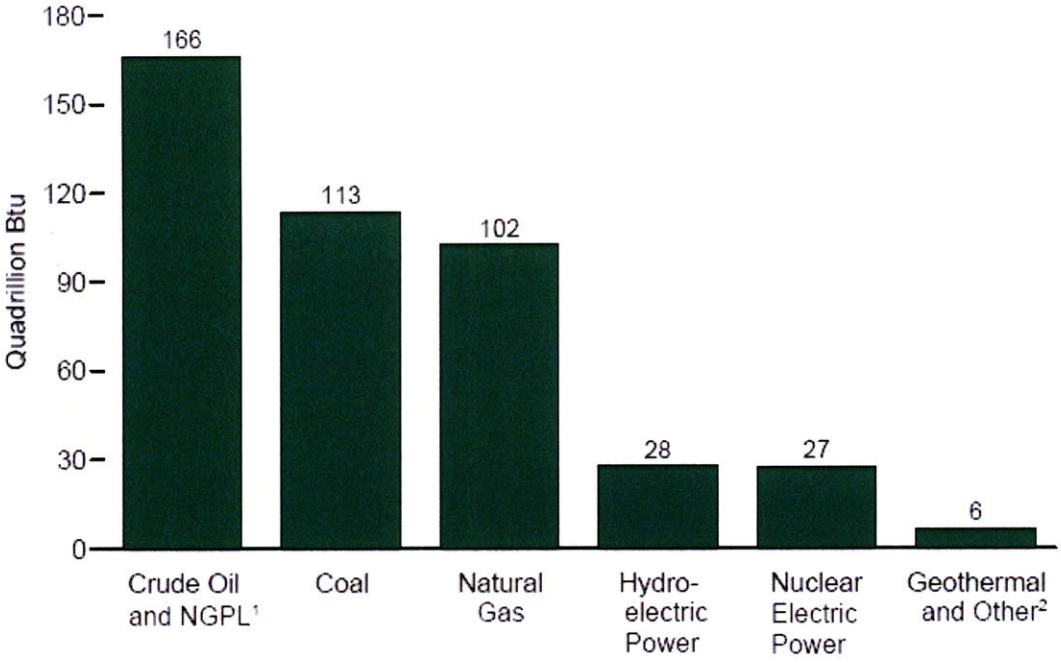

Fig. 1.1. World primary energy production by source (2004) [1].

Currently, approximately 85% of the world's energy production and consumption is in the form of fossil fuels, such as coal, oil, and natural gas (see **Fig. 1.1**). Although this form of energy has much appeal in its ability to be efficiently converted to commercial power, it has the shortcoming of being a non-renewable or exhaustible energy source. More specifically, if world nations were to continue to consume energy at the current rate, oil and gas could only supply all energy needs for approximately the next 100 years and coal for about the next 200 years. Although one might initially infer from this statement that fossil fuel depletion is more of a long term problem, there are some important underlying issues to consider. For example, not only is the world population ever increasing, but society is also always looking for ways to improve its quality of life, both of which will result in an increasing rate of energy consumption per capita and, consequently, shrinking the already bleak window available for fossil fuel use. Finally, one must also be aware of the ever increasing damage that fossil fuel emissions have on the environment. Not only has rising atmospheric concentrations of CO_2 and other greenhouse gases from the burning of fossil fuels contributed directly to pollution and global warming, it has also caused significant unwanted changes in global climate, further diminishing the appeal of fossil fuels [2].

Given the rather long and disapproving list of attributes ascribed to fossil fuels as an energy source, one might look to renewable sources of energy such as solar radiation, wind, and hydro. Although these alternative forms of energy do contribute to the world energy consumption and are substantially less harmful to the environment, their contribution is only less than 8% due to their inability to be converted efficiently to commercial electricity (see **Fig. 1.1**). Unlike fossil fuels, which can be easily burned, converted, and transported to any location, renewable forms of energy require the source, such as the sun, wind, or water, to exist near the site requiring power, making them currently somewhat less efficient and useful [2].

An alternative to the non-renewable and renewable sources of energy that makes up the final 6.5% of current world energy consumption is nuclear fission (see **Fig. 1.1**). Unlike the more conventional energy sources, nuclear fission cannot be easily classified as a renewable or non-renewable energy source. Nuclear fission power utilizes uranium as its primary fuel, and given the United States' current policy of a once-through cycle with no fuel reprocessing, reactors are currently designed only for exhaustible energy production. Because of these political constraints, only about 2.3% of the uranium fuel that is of the fissionable type (^{235}U) is able to be utilized. Granted, one might argue that if fuel reprocessing were implemented, the energy content of the uranium could be substantially increased and this, combined with the absence of greenhouse gases that contribute to pollution and global warming, might make nuclear fission an appealing energy source. However, nuclear fission power does produce significant amounts of radioactive waste that has created additional political and societal objections [2].

So based on this analysis of current world energy production, one might cast a seemingly grim outlook on alternative energy sources for future generations. However, one promising energy source remains for which a strong case can be made...nuclear fusion energy. Nuclear fusion is the process by which light nuclei combine to form a heavier nucleus, releasing energy proportional to the mass difference of the reactant nuclei and the product nuclei, according to the formula $E = \Delta mc^2$. The primary fuel components for fusion consist of deuterium and tritium, both isotopes of hydrogen that can be extracted from sea water. Although tritium makes up only about 10^{-15}% of sea water, deuterium is readily abundant, making up about 0.015% and endowing the world's oceans with a seemingly infinite source of fuel for fusion power. To add to its list of attributes, fusion energy is not only free of

greenhouse gases that contribute to pollution and global warming but is also relatively low in radioactive waste products. So the only challenge that remains is how to produce and harness fusion energy in a controlled way and to efficiently distribute it as commercial power to world nations [2].

1.2 Basic Fusion Principles

The most fundamental attribute that makes fusion superior to other energy sources, such as fossil fuels, is the process by which energy is released. Whereas fossil fuels utilize chemical processes that achieve energy gain through the rearrangement of outer valence electrons, fusion achieves energy gain through the rearrangement of nucleons in the nuclei of the interacting species. Because this rearrangement of nucleons is due to the strong force over distances of a few Fermi compared to electromagnetic forces over distances of a an angstrom for electron rearrangement, the typical energy release from fusion reactions, which is around several MeV, is approximately six orders of magnitude larger than the chemical reactions that make up the burning of fossil fuels. More specifically, if one were to translate these energy equivalences into fuel,

Fossil Fuels	≈	Fusion
(10^6 tons of oil)		(0.2 tons of Deuterium)

This enormous difference in energy release will similarly translate into fuel recovery, transportation, and the generation of waste [2].

Of the many different fusion processes by which light nuclei could fuse into heavier nuclei and release energy, only a few could be considered feasible for energy production [3]; namely,

$$D + T \rightarrow {}^4He\ (3.5\ MeV) + n\ (14.1\ MeV) \tag{1.1}$$

$$D + D \rightarrow {}^3He\ (0.82\ MeV) + n\ (2.45\ MeV) \tag{1.2}$$

$$D + D \rightarrow T(1.01\ MeV) + p\ (3.02\ MeV) \tag{1.3}$$

$$n + {}^{6}Li \rightarrow {}^{4}He\ (2.1\ MeV) + T\ (2.7\ MeV) \qquad (1.4)$$

At first glance, one might consider producing fusion energy using the above reactions by shooting a beam of nuclei, such as deuterium, at a target made up of, say tritium. Although this approach, which is commonly referred to as beam fusion, does trigger fusion reactions, it also allows for a significant amount of Coulomb scattering, causing many of the beam particles to lose their energy in the target before achieving fusion [4]. As a result, this approach is not a feasible option for power production.

However, one can instead achieve net energy production by a process known as thermonuclear fusion, in which a plasma of light nuclei from the above reactions is heated to a sufficiently high temperature. Through this approach, if one is able to keep the plasma confined for a sufficient period of time and at a certain temperature and density, the particles will be able to undergo Coulomb collisions such that their kinetic energy gets redistributed and fusion reactions will occur after a sequence of collisions. For thermonuclear fusion to be a feasible source of power, though, the fuel must advance through a series of stages: ignition, burn, and then break-even. Ignition occurs when a certain temperature is reached such that no further external energy input is required to sustain internal heating by fusion reactions. This temperature, though, will depend on the fusion fuel, as well as relevant loss mechanisms such as bremsstrahlung. Once the fuel reaches ignition, it will continue to burn without external aid until conditions are no longer feasible. If the fuel is able to burn long enough such that the total energy produced is equivalent to that needed to initiate ignition and burn, then break-even is achieved [4].

In order to evaluate the efficiency of a fusion reactor or process, one defines a fundamental quantity known as the gain of the process. The gain consists of the ratio of the total energy produced by the reaction to the total external energy needed to trigger ignition. For all types of thermonuclear fusion processes, the gain is normally a function of the density of the fuel and the amount of time it is contained. More specifically, higher densities will allow the fuel to retain a high enough system energy to sustain fusion burn than lower densities, while longer containment times will allow more fuel to undergo fusion burn than would shorter containment times. At present there are two main approaches to plasma confinement that seek to satisfy these parameters: magnetic confinement and inertial confinement [4].

Magnetic confinement is an approach to controlled fusion by which strong magnetic fields are used to confine particles and force them to move only in the direction of field lines while heating occurs. In order to achieve high gains, this approach utilizes relatively long confinement times (0.1 seconds), while the densities for magnetically confined plasmas are relatively low (10^{15} cm^{-3}). One typically refers to the Lawson criteria as the condition for sustained operation in a magnetic confinement fusion device

$$n\tau \cong 2\times 10^{14} cm^{-3} s, \tag{1.5}$$

where n is the density and τ is the confinement time. Because plasma confinement is largely dependent on the magnetic field configuration, many magnetic fusion devices have been explored, such as tokamaks, spheromaks, stellerators, reversed field pinches, etc. [4].

In contrast, inertial confinement fusion is an approach to controlled fusion by which confinement is achieved through mass inertia, rather than any external means. A plasma is assembled in a small spherical volume while high power lasers are used to compress and ignite the assembled fuel. Unlike magnetic confinement fusion, this approach utilizes very high densities ($10^{25}$$cm^{-3}$) to achieve high gain, while confinement times are relatively short (10^{-10} seconds). One can derive a condition for sustained operation in an inertial fusion device analogous to the Lawson criterion

$$\rho R \cong 0.2 - 0.5 g/cm^2, \tag{1.6}$$

where ρ is the fuel density and R is the hot spot radius, which will be discussed in more detail in the section that follows [4].

1.3 Inertial Confinement Fusion

The scheme now known as inertial confinement fusion was originally proposed by Knuckles et al. in 1972, marking the year zero of inertial fusion research [5]. Although variations and advancements have been made on this original scheme in the past several

decades, all are still based on the fundamental idea of using a laser driven implosion of a cryogenic fuel sphere to achieve the necessary compression and heating needed for ignition [5]. Although some early schemes for inertial confinement fusion considered volume ignition, in which a solid fuel target is heated to necessary fusion conditions, large external energy requirements led to the abandonment of this method in favor of "hot spot ignition." Whereas volume ignition consists of heating an entire solid fuel sphere, hot spot ignition relies on heating a hollow shell of fuel such that only a small part of the target, the hot spot, is heated to fusion conditions and a burn wave propagates outward to heat the surrounding fuel, leading to higher gains [4].

A typical fuel target designed for hot spot ignition using the D-T fusion reaction, depicted in **Fig. 1.2,** consists of a hollow spherical shell of plastic with an inner layer of cryogenic D-T and a D-T gas fill.

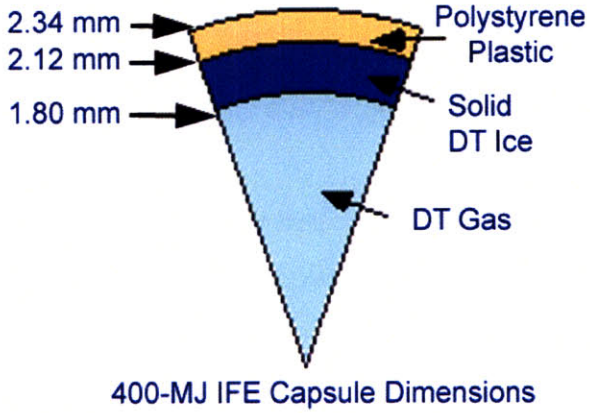

Fig 1.2. Fuel composition and geometry for a typical spherical ICF target [6].

In a typical implosion, the target will undergo four phases to achieve hot spot ignition: ablation, compression, ignition and burn. During the initial phase, laser beams are launched at the target with the goal of heating the outer surface such that energy is delivered to the target uniformly. As the outer surface then expands, or ablates, outward, an inward, rocket-like effect drives the fuel towards the center in order to conserve momentum. As the fuel travels inward and the remaining fuel is compressed, shock waves act to equalize pressure throughout the target. More specifically, in this final stage of compression, the fuel consists of two distinct regions, as

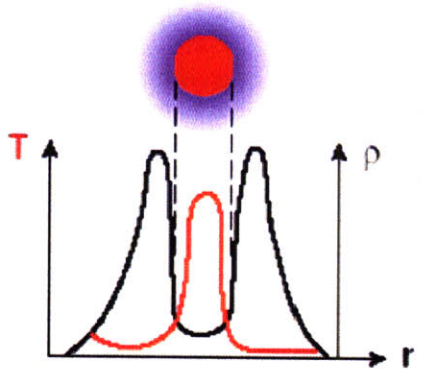

Fig.1.3. Fuel density and temperature configuration at the final stage of compression consisting of a low-density central hot spot and a high-density cold shell [6].

shown in **Fig. 1.3**, an outer region of dense, cold fuel and a central region of hot fuel, containing the remaining 2-5% of the fuel mass. For ignition to occur, the equivalent Lawson criteria and temperature for inertial confinement must be reached: a hot spot with an areal density of ρR_{hot} ~ 0.2-0.5 g/cm^2 and a temperature of 5-10 keV. At these conditions, the 3.6 MeV alpha particles produced from the D-T fusion reactions have a range just large enough to stop within the hot spot to raise the surrounding fuel temperature and trigger a burn wave to propagate into the outer region of cold fuel [6].

This process by which the fuel is compressed to a state of pressure equilibrium is known as isobaric compression. At present, there are two existing approaches to inertial confinement fusion that seek to utilize isobaric compression to achieve ignition: direct drive and indirect drive. The direct drive approach to ICF, shown in **Fig. 1.4(a)**, consists of shining laser beams directly onto the surface of the fuel capsule, relying on the laser energy to be transferred to the target via a number of absorption mechanisms such as inverse bremsstrahlung. Although direct drive is currently one of the primary approaches being explored, it does place rather stringent requirements on high precision drive symmetry and compression [6]. On the other hand,

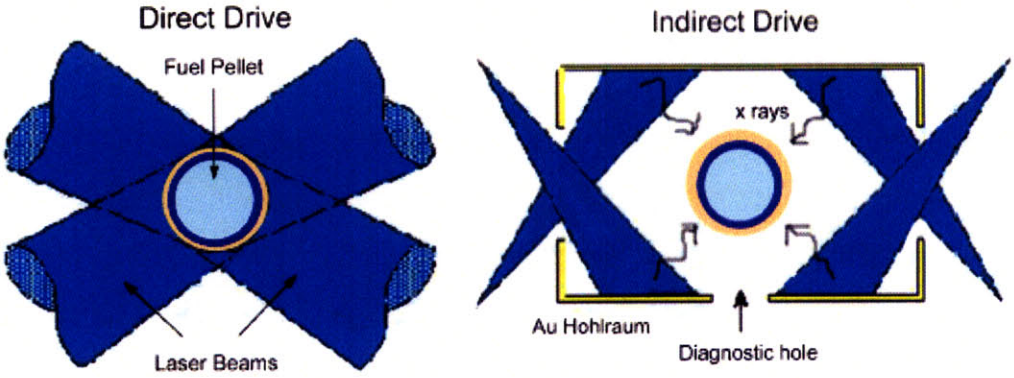

(a) **(b)**

Fig.1.4. Two main approaches to conventional ICF. (a) Direct Drive relies on uniform laser irradiation onto the fuel pellet. (b) Indirect Drive relies on x-rays produced from laser interactions with the inner walls of a hohlraum [6].

indirect drive, shown in **Fig. 1.4(b)**, seeks to achieve capsule implosion indirectly using thermal radiation inside a cavity, known as a hohlraum. The most common hohlraum geometry consists of a cylindrically symmetric cavity made of a high-Z material such as gold with laser entrance holes at each end. When laser beams enter the entrance holes on the axis, they interact with the inner surface of the wall, where they are then converted to x rays that reradiate to drive the capsule implosion. Because black body radiation is uniform and isotropic, this method ensures symmetric capsule drive. However, like direct drive, this scheme does have its drawbacks. By indirectly driving the capsule implosion, one incurs a significant loss in coupling efficiency from heating the hohlraum [6].

1.4 Fast Ignition

To evade the subsequent problems with isobaric compression that have plagued conventional methods of inertial confinement fusion, an alternative scheme known as fast ignition was proposed by Tabak et al. in 1992 that would instead utilize isochoric compression [7]. The central theme of fast ignition consists of igniting a pre-compressed fuel core with a separate external trigger. Although the idea had existed as early as the 1960s, the advancement of petawatt laser technology in recent years has sparked new interest in the fast ignition concept.

Until recently, a suitable trigger with the capabilities for ignition had not been available until the recent development of short, high-intensity laser pulses [4].

The fundamental appeal of the fast ignition concept is its innate ability to decouple target compression from fuel ignition. With the conventional method of inertial confinement fusion, the necessity of formation of a central hot spot and its ensuing isobaric conditions require the entire target to be raised to a given pressure for ignition (see **Fig. 1.5(a)**). For this to occur, the two stages of ignition and compression must be coupled together by a spherical implosion. Although this method has been relatively successful, the coupling of compression and ignition places extreme requirements on high-precision target design and drive symmetry. In addition, the subsequent hot spot that is formed is highly hydrodynamically unstable. Alternatively, fast ignition allows the separation of target compression and ignition into two separate stages. Whereas fast ignition still requires the target to be compressed to high densities, as in the conventional method of ICF, it relies on isochoric, or constant density, conditions, such that the pressure and temperature within the target are relatively constant, as depicted in **Fig. 1.5(b)**. As one can see, a lower peak fuel density is needed compared to conventional ICF, allowing for lower driver energies, more fuel mass available for burn, and

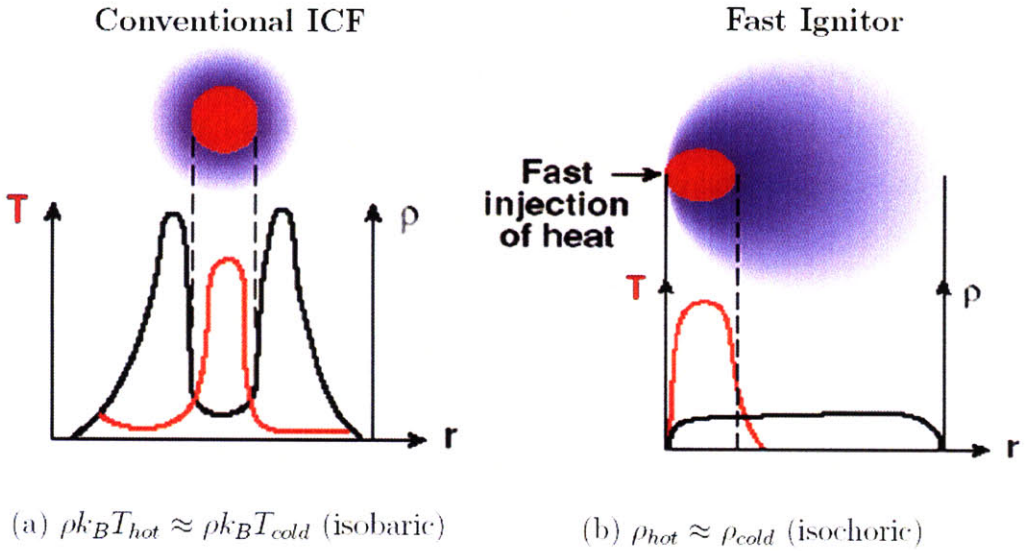

(a) $\rho k_B T_{hot} \approx \rho k_B T_{cold}$ (isobaric) (b) $\rho_{hot} \approx \rho_{cold}$ (isochoric)

Fig. 1.5. Comparison between conventional ICF and the Fast Ignitor approach. (a) Conventional ICF relies on isobaric compression of the fuel pellet. (b) Fast Ignition relies on isochoric compression of a pre-compressed fuel core [6].

subsequently higher gains. This approach dramatically reduces the symmetry requirements and may even permit the use of non-spherical fuel configurations [4].

For fast ignition to be scientifically feasible, though, a sufficient amount of laser energy must be deposited to ignite the pre-compressed fuel before pressure equilibrium can reestablish itself. Using a 1-D isochoric model, one can estimate the required energy and other parameters needed for a fast ignition trigger. Namely, consider a sphere of DT fuel that has been pre-compressed by conventional driver methods to uniform density ρ, after which the short, ultra-intense laser pulse is applied that heats a small volume at the fuel surface very rapidly (in a time t ~ 10-50 ps) to ignition temperature T_h. Since this rapid heating is faster than hydrodynamic expansion, the density of the small ignition volume where the energy has been deposited remains almost the same as that of the other pre-compressed fuel. As a result, one can, to a first approximation, model fast ignition with isochoric conditions. Calculations for an isochoric hot spot located in the center of a uniform fuel sphere with typical isochoric conditions of $\rho R \geq 0.5$ g/cm^2 and $T_h \geq 12keV$ have shown that the ignition energy scales like

$$E_{ign} = 72/(\rho^*)^2 \text{ kJ}, \tag{1.7}$$

where ρ^* is the fuel density in units of 100 g/cm^3 [4]. This energy has to be focused to a spot radius less than the hot spot radius, R_h, in a time shorter than $t_c \approx R_h/c_s$, where $c_s \approx 2.8 \times 10^7 T_h^{1/2}$ cm/s is the sound speed and T_h the temperature in units of keV. Taking a fuel density $\rho = 500$ g/cm^3, typical of the fast ignitor approach, we find that we need to deliver $E_{ign} = 8\ kJ$ in a pulse shorter than 20 picoseconds onto a spot of $r_p \approx 15\mu m$. The corresponding power of the ignitor pulse is $W_{ign} \approx E_{ign}/t_p \approx 5 \times 10^{14}\ W$ and the intensity $I_{ign} \approx P_{ign}/\pi R_h^2 \approx 7 \times 10^{19}\ W/cm^2$ [4]. With the advent of short, high intensity laser pulses, achieving these parameters is no longer an impossible task.

The final challenge that remains is how to efficiently transport this energy to the pre-compressed fuel core. Based on the previous calculations, if the igniting pulse were to be delivered by charged particles, they should have a range comparable to or somewhat smaller than the areal density of the required hot spot, i.e., $R < 2\rho R_h$. At present, both electron and ion pulse scenarios are being considered as potential candidates to carry the laser energy to the

compressed fuel core. Because of their high coupling efficiency to the fuel at the end of their range, intense laser-accelerated proton beams have emerged as a popular option for energy transport. Several variations of this technique are currently being considered, but the primary technical difficulty is how to deliver these beams in the small spot sizes and short pulse lengths necessary for fast ignition [4]. Alternatively, energy transport via relativistic electron beams is also an option being considered. Like the proton driven scheme, electron-driven fast ignition faces a number of challenges, which will be addressed in the section that follows; however, this option is still a viable candidate for providing the necessary vehicle to spark ignition.

1.5 Electron Transport Issues

For electrons to transport the necessary energy estimated in the previous sections to the pre-compressed fuel core, relativistic electron beams with currents of the order of 100MA are required. Although currents of this magnitude are not unheard of, the major challenge to be addressed is how efficiently these beams can be produced and transported the approximately 100 μm distance from a density of 10^{21} cm^{-3} to $10^{26}cm^{-3}$. At present, the behavior of electrons in overdense plasmas is not well understood. As a result, there are a number of issues to consider, namely, the laser-to-electron conversion efficiency, the collimation of the beam, and electron stopping in the core.

The idea currently being explored for electron-driven fast ignition is the cone-guided scheme, depicted in **Fig. 1.6**. More specifically, recent research has found that electron transport can be substantially improved by embedding a guiding cone into the side of the fuel target. The purpose of the cone is to keep a small corridor free of plasma during the initial compression stage, thus reducing the distance over which the electron beam must be transported. After an initial stage of compression via conventional long pulse, moderate intensity lasers, a short-pulse, high-intensity laser is shined into the cone corridor where it undergoes a laser-plasma interaction. Near the inner edges and partially ablated tip of the cone, relativistic electrons are produced and accelerated from the point of creation. The hope is that these electrons will be sufficiently collimated that they can transport the laser energy the approximately 50-100 μm distance to the compressed fuel core, where they will be stopped and deposit their energy [4].

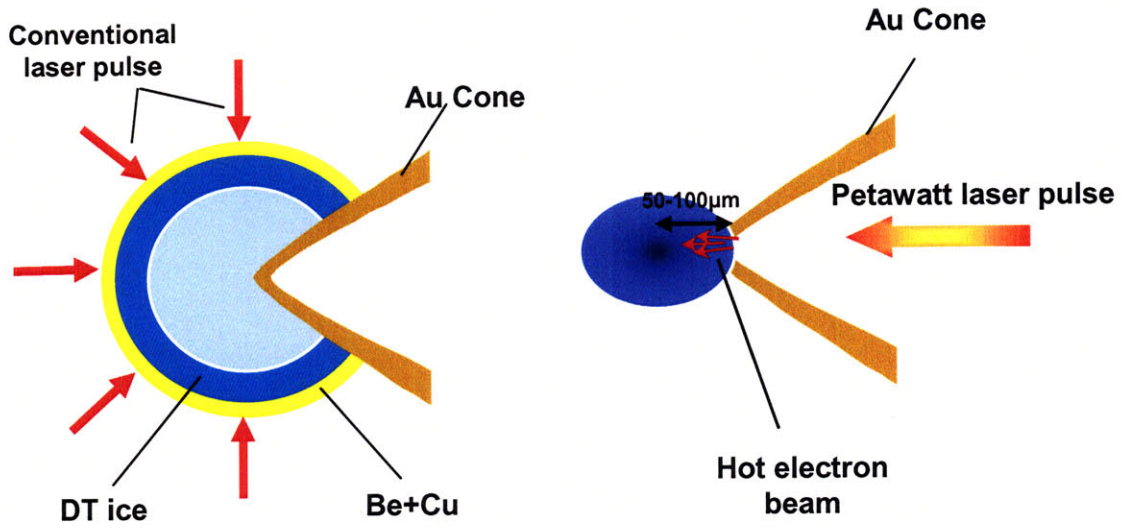

Fig. 1.6. Cone-guided fast ignition approach. (a) Compression of the fuel pellet via conventional long pulse, moderate intensity laser beams (b) A petawatt laser pulse produces a relativistic electron beam which carries the laser energy to the fuel core.

Although the insertion of the cone does improve the relativistic electron beam transport, the beam will still be subject to a number of micro-instabilities such as the two-stream, Weibel, and filamentary that act to inhibit energy transport. The initial linear and later nonlinear growth phases of these instabilities will evolve differently depending on the initial conditions, the shape of the electron distribution, and collisional effects. Although there is a vast volume of literature in this area spanning several decades, there has not been an extensive analytical model including all of the relevant physics necessary to analyze the evolution of these instabilities, nor has there been comparison of analytical results with a sufficiently robust computer code. This research will attempt to provide the necessary theoretical and computational tools to analyze these instabilities for fast ignition relevant conditions.

Chapter 2

Short Pulse, High Intensity Laser Plasma Interactions

2.1 Ultra-Intense Laser Technology

It was shown in Chapter 1 that to achieve ignition conditions for the fast ignitor scheme, approximately 8 kJ of energy must be delivered in a pulse shorter than 20 ps onto a spot of 15μm. In other words, for fast ignition to be feasible, a laser pulse power of approximately $5x10^{14}$ W and an intensity of $7x10^{19}$ W/cm^2 would be needed. Although petawatt-scale lasers of this type are becoming rather commonplace in the laser fusion field nowadays, peak intensities of this magnitude have only been made available in the last couple of decades with the development of chirped pulse amplification (CPA) [4].

As one can see in **Fig. 2.1**, advances in laser technology have occurred in spurts, beginning with the first optical kW-scale laser in 1960 [8]. As innovations such as Q-switching (MW) and mode-locking (GW) were developed in the years that followed, peak intensities

steadily increased until they leveled off in the mid-1970's [9]. Finally, in 1985, a new technique known as chirped pulse amplification was first applied to lasers and combined with Kerr-lens mode locking, a technique for accurately generating short fs-scale pulses, which gave laser technology the needed boost into the uncharted territory of the ultra-high intensity (10^{18}-10^{21} W/cm^2) regime [10,11].

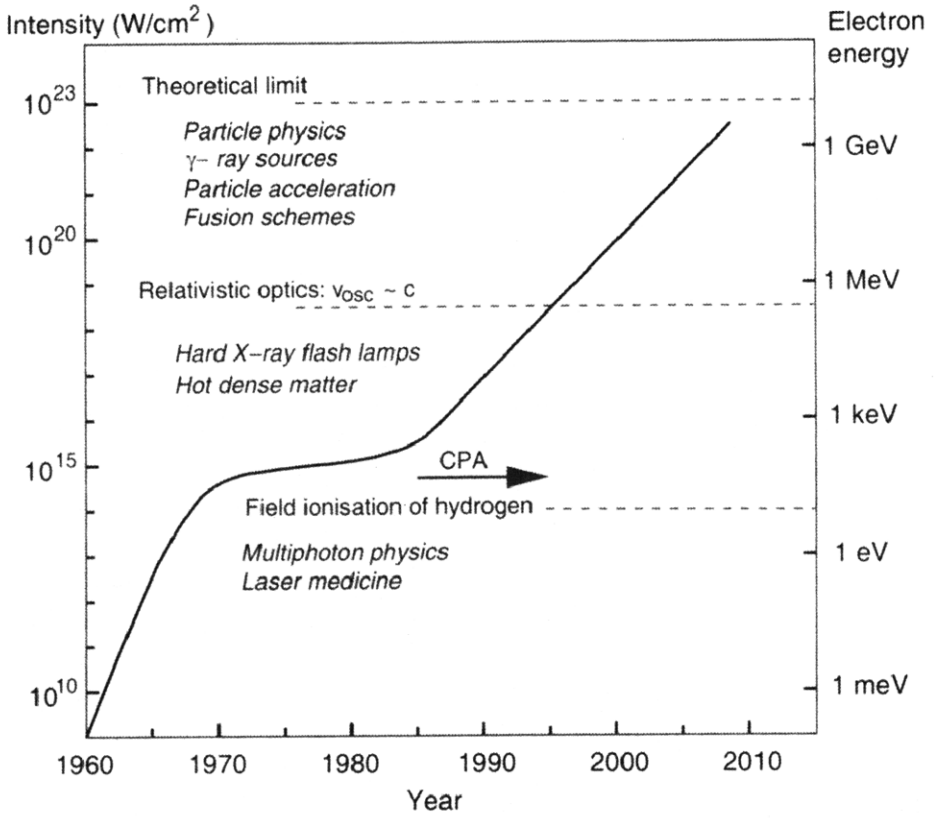

Fig. 2.1. Advances in laser peak intensity and electron energy [8].

Since peak intensities could, in theory, be boosted simply by increasing the laser power after it has been generated by adding amplifiers to the chain, one might ask why there is a need for such advanced technology. The answer lies in the optical components of the laser system, which can become damaged and/or overheated if the fluence exceeds a level of approximately 0.16 Jcm$^{-2}\tau_{ps}^{1/2}$, where τ_{ps} is the pulse length in picoseconds. Although this fluence level is quite limiting, one would still hope to achieve maximum efficiency, which occurs when the fluence approaches the saturation level of the amplifying medium. For Ti:sapphire, this occurs

at 1 Jcm^{-2}; therefore, to allow the optical components sufficient time to cool by thermal conduction, one would use a pulse length of at least 40 ps throughout the amplifier chain. So to achieve the desired high power without incurring optical damage to the laser components, ultra-short pulses are first generated in the oscillator, after which they are temporarily stretched before amplification so that the intensity is low enough in the gain medium so as not to induce damage. After amplification, the high energy pulse is then recompressed to its original sub-picosecond length, thus creating the short, ultra-high intensities needed for fast ignition [8]. In fact, several laser facilities utilizing this technique have even reached intensities as high as 10^{21} W/cm^2 [12].

Although chirped pulse amplification does allow lasers to attain an impressive range of peak intensities beneficial to fast ignition and many other applications, this technique is not without its vices. Because of amplified spontaneous emission that can occur with the use of CPA, a lower-intensity pre-pulse is emitted approximately 100's of picoseconds to nanoseconds before the main pulse. For classical, moderate-intensity long pulse lasers, this pre-pulse is insignificant because the intensity is low enough ($< 10^{12}$ W/cm^2) such that it does not induce ionization in the target material before the main pulse arrives. However, the pre-pulse for short-pulse ultra-intense laser systems can actually exceed the threshold for ionization, depending on laser system's contrast, which is the ratio of intensity of the pre-pulse to the main pulse, and can range from 10^{-9} to 10^{-4}. If the contrast is low enough, a "pre-plasma" is created in front of the target that the main pulse will interact with, instead of the original high density target surface. The scale length of this pre-plasma can be approximated by

$$L_{pre} = \frac{n}{dn/dx} \approx c_s \tau_{pre} \tag{2.1}$$

where τ_{pre} is the pulse length of the pre-pulse, n is the plasma density, dn/dx is the slope of the density profile, and c_s is the ion sound speed, i.e,

$$c_s = \sqrt{\frac{Z(T_e + T_{ion})}{M_{ion}}}. \tag{2.2}$$

High contrast (< 10^{-8}) lasers tend to generate short scale-length pre-plasmas on the front surface of targets of approximately 2-5 microns; however, as the contrast increases into a range greater than 10^{-4}, pre-plasmas as long as 100's of microns can be created [13]. For fast ignition relevant schemes, high contrast laser pulses are preferred because a reduction in pre-pulse/pre-plasma will allow the main laser pulse to interact directly with the solid high-density target, which has been used to extrapolate to the high densities relevant to fast ignition configurations [4].

2.2 Relativistic Effects on Ultra-Short Pulse Laser Plasma Interactions

The fast ignition scenario will rely on the short pulse laser-plasma interaction to efficiently couple energy to the compressed plasma core. This transfer of energy will take place via electrons that oscillate in the electric field of the laser pulse, E_0. If one were to write the dimensionless velocity of these electrons in terms of this field amplitude, as follows

$$\beta = \frac{v_{osc}}{c} = \frac{p_{osc}}{m_e c} = \frac{eE_0}{\omega_L m_e c}, \tag{2.3}$$

where ω_L is the frequency of the laser, this can then be further expressed in terms of the laser irradiance, $I\lambda^2$,

$$\beta = \sqrt{\frac{I\lambda^2 (W\mu m^2 / cm^2)}{1.37\times 10^{18}}}. \tag{2.4}$$

As one can see, for $\lambda_L \sim 1\mu m$ light, electrons acquire relativistic velocities ($\beta \sim 1$) for intensities greater than 10^{18} W/cm^2. Since it was previously shown that fast ignition will require peak intensities of the order of $10^{19} - 10^{20}$ W/cm^2, relativistic dynamics are essential for proper consideration of the laser plasma interaction [4]. With this in mind, one might ask what immediate implications these relativistic effects might have on the laser plasma interaction. For starters, the usual plasma parameters such as the plasma frequency, the critical density, and the index of refraction will be modified, as well as the onset of a few new phenomena.

As the laser pulse propagates through the plasma, electrons that are exposed to the laser's electric field will acquire a relativistically enhanced mass at high intensities. As a result, the local plasma frequency is modified such that m_e gets replaced by γm_e, given by

$$\omega_{pe}^{rel} = \sqrt{\frac{4\pi e^2 n_{pe}}{\gamma m_e}} = \frac{\omega_{pe}}{\sqrt{\gamma}}. \tag{2.5}$$

So in the absence of collisions, if one were to re-derive the dispersion relation for the propagation of an electromagnetic wave in a plasma, the modified expression would become

$$\omega = \sqrt{k^2 c^2 + \frac{\omega_{pe}^2}{\gamma}} \tag{2.6}$$

As one can see in **Fig. 2.2(a)**, the relativistically enhanced mass has created an "induced transparency." Whereas in the non-relativistic limit, a laser pulse with frequency ω_L could not propagate, the plasma becomes transparent to the same laser pulse for relativistic intensities due to a local lowering of the plasma frequency [4].

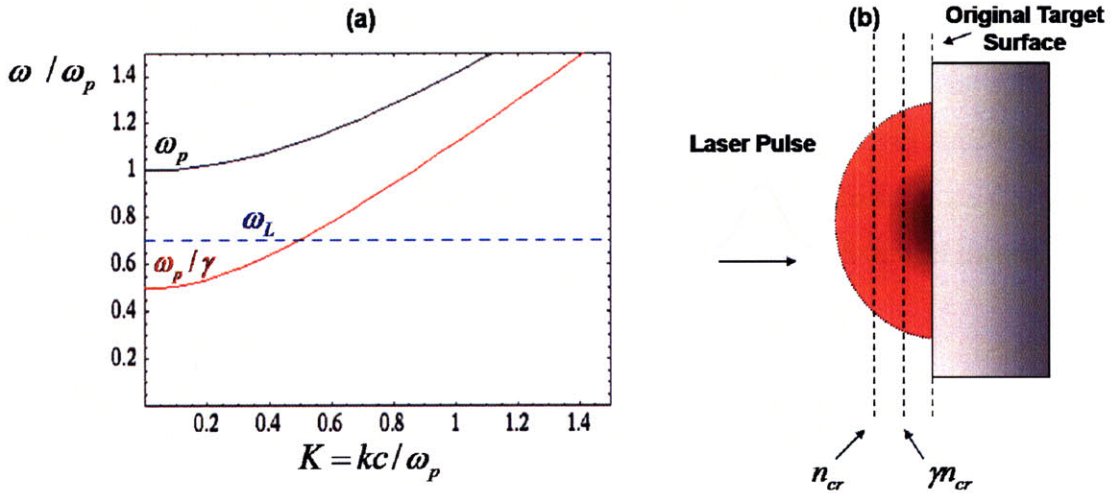

Fig. 2.2 (a) Induced transparency of the plasma [4] and (b) laser access to higher density regions with relativistic effects ($\gamma > 1$).

This relativistically enhanced electron mass has a similar effect on the critical density of the plasma. As the laser pulse propagates up the density gradient of the underdense plasma, it eventually reaches a point (density) at which the wave number becomes imaginary and the laser pulse can no longer propagate. This is conventionally defined as the critical density, n_c, which can be derived by setting the laser frequency equal to the plasma frequency, i.e.,

$$\omega_L^2 = \frac{4\pi e^2 n_{cr}}{\gamma m_e}, \tag{2.7}$$

which can be re-expressed in terms of the critical density as

$$n_c = \gamma \frac{1.1\times 10^{21}}{\lambda_\mu^2} cm^{-3}. \tag{2.8}$$

As one can see in **Fig. 2.2(b)** and equation 2.8, the implication of the gamma factor is that for relativistic intensities ($\gamma > 1$), the laser pulse can penetrate deeper into the plasma to higher density regions [13].

In addition to plasma parameter modifications, other nonlinear optical effects can arise when relativistic dynamics are included, such as self-focusing of the laser pulse [14,15,16]. In other words, as laser intensities are increased, the plasma is able to act on the beam like a positive lens with a tendency to focus it. However, because diffraction, a competing effect, can act to defocus the beam, there exists a critical power above which relativistic self-focusing will dominate. A rough estimate of the critical power can be derived from simple geometrical arguments [8] (shown in **Fig. 2.3**) and by also assuming the laser beam has a radial profile given by

$$a(r) = a_0 e^{-r^2/2\sigma_0^2}, \tag{2.9}$$

where a_0 is the dimensionless light amplitude, $eA_0/m_e c^2$, and σ_0 is the radial spot size to which

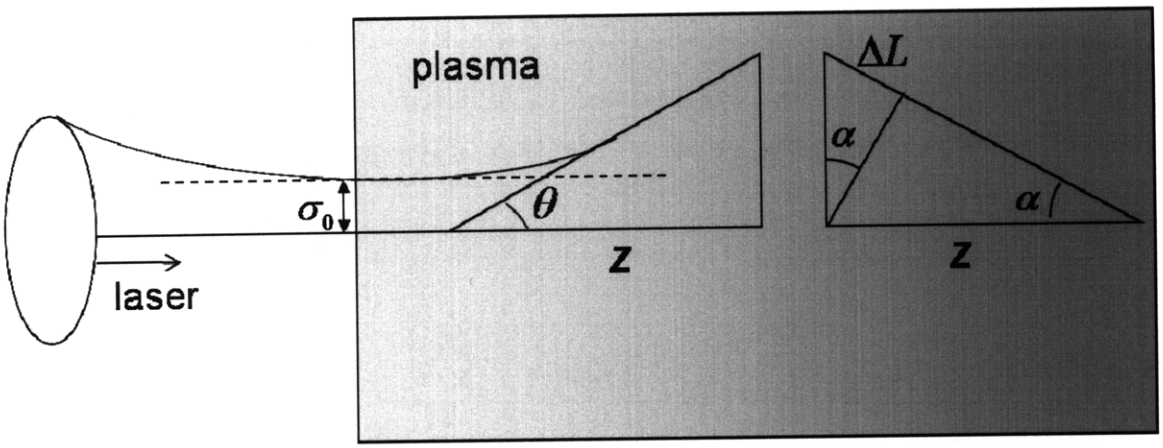

Fig. 2.3 Geometry of relativistic self-focusing versus defocusing due to diffraction [8].

the laser has been focused. From the standpoint of defocusing due to diffraction, one can estimate the divergence angle of the beam from the geometrical picture by [17]

$$\theta_d = \frac{dR}{dZ} = \frac{\sigma_0}{Z_R} = \frac{1}{k\sigma_0}, \tag{2.10}$$

where Z_R is the Rayleigh length, which is defined in this geometry as

$$Z_R = \frac{2\pi\sigma_0^2}{\lambda}. \tag{2.11}$$

Focusing, on the other hand, can be derived by first considering the modification of the index of refraction of the plasma due to the relativistic mass increase. As was mentioned previously, the local plasma frequency is reduced at high intensities, shown by the extra gamma factor in its formulation. The corresponding effect on the index of refraction of the medium can be computed by

$$\eta(r) \equiv \frac{ck}{\omega} = \left\{1 - \frac{\omega_p^2}{\omega^2 \gamma(r)}\right\}^{1/2} \tag{2.12}$$

As one can see from this expression, for $\gamma > 1$, $d\eta/dr < 0$, which is the classical optical definition of a "positive" focusing medium. To put this into more geometrical terms, one can re-express this in terms of the phase velocity of the wave fronts passing through the focusing medium as

$$\frac{v_p(r)}{c} = \frac{1}{\eta} \cong 1 + \frac{\omega_p^2}{2\omega^2}\left(1 - \frac{a^2(r)}{4}\right) \tag{2.13}$$

where $\gamma(r)$ has been approximated by $\sqrt{1 + a^2(r)/2}$. Geometrically, one can see from both this expression and **Fig. 2.4** that the phase fronts will travel more slowly at the center, giving a difference in phase velocity of

$$\frac{\Delta v_p(r)}{c} = \frac{\omega_p^2}{8\omega^2} a_0^2 e^{-r^2/\sigma_0^2} \tag{2.14}$$

One can compute the maximum focusing angle of the beam by recognizing from **Fig. 2.4** that the rays of the phase front will bend by an amount determined by their relative path difference, i.e.,

$$\Delta L = \left|\Delta v_p\right|_{\max} t = \left|\frac{\Delta v_p}{c}\right| Z = \alpha R \tag{2.15}$$

which can be solved for a maximum focusing angle, α, of

$$\alpha = \frac{\omega_p a_0}{\sqrt{8}\omega}. \tag{2.16}$$

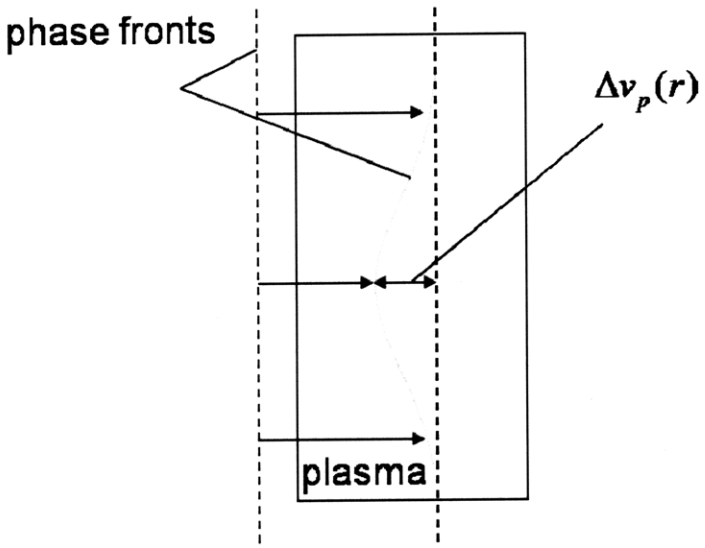

Figure 2.4 Bending of the phase fronts near the central peak intensity due to relativistic self-focusing [8].

So one can deduce that self-focusing will cancel diffraction when $\alpha = \theta$, yielding the inequality

$$a_0^2\left(\frac{\omega_p \sigma_0}{c}\right)^2 \geq 8. \tag{2.17}$$

Since power is proportional to $a_0^2\sigma_0^2$, this yields an approximate critical power threshold [8]. Although this derivation is somewhat simplistic, it is in reasonable agreement with more exhaustive derivations that utilize the nonlinear Schrödinger equation that can be found in the literature and quote a critical power of [14,15,16]

$$P_c \cong 17.5\left(\frac{\omega}{\omega_p}\right)^2 GW\,. \tag{2.18}$$

The ponderomotive force is yet another phenomenon in laser plasma interactions that must be revisited in the short pulse high intensity laser regime. In general, the ponderomotive The non-relativistic (v << c) form of this force is normally expressed as [8]

$$F_{p,nonrel} = -\frac{1}{2}\frac{\omega_{pe}^2}{\omega_0^2}\varepsilon_0 \nabla E^2, \tag{2.19}$$

where ω_{pe} is the local plasma frequency, ω_0 is the laser frequency, and E is the local electric field. As one can see in **Fig. 2.5**, the physical implications of this force are to push electrons away from regions of high intensity. In other words, an electron that initially sits near the peak of the radial intensity profile of the laser will experience a force to lower intensity regions. However, this idea of a purely transverse acceleration does not exist when relativistic effects are included. At higher intensities, the relativistically correct expression becomes [18,19]

$$F_{p,rel} = -mc^2 \nabla(\gamma - 1), \tag{2.20}$$

where $\gamma = \sqrt{1 + p^2 / m_e^2 c^2}$. As one can see in **Fig. 2.5**, what this means physically is that at relativistic intensities, the ponderomotive force develops a longitudinal component such that electrons acquire a forward motion in the direction of the laser, in addition to their transverse motion.

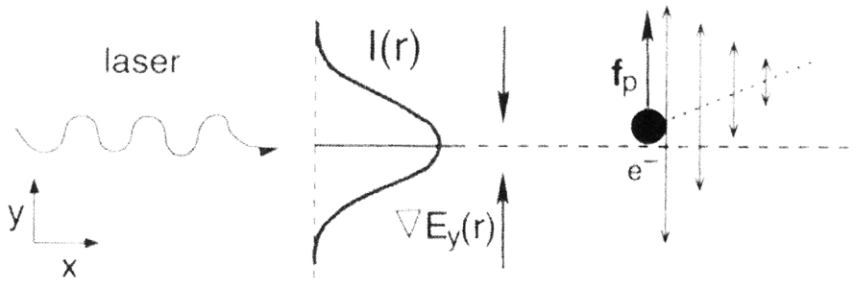

Fig. 2.5 Physical depiction of the ponderomotive force due to a focused beam [8].

Laser hole boring is another effect that can arise for relativistic intensities. However, unlike the other phenomena that have been mentioned, it does not occur solely from relativistic effects and can arise due to other situations such as final focal spot sizes. In sum, hole boring is an effect due to pressure balance first studied by Wilks et al. that occurs when tightly focused light bores a hole through overdense plasma on an ultra-short timescale [20]. For this to occur,

the light pressure must be much greater than the plasma pressure, which then causes the plasma to be pushed inwards toward the focal spot. The end result is the formation of an electrostatic bow-shock and a density discontinuity that moves inward with approximately constant velocity [8]. Laser hole boring has been verified both in 2D PIC simulations and also in short pulse high intensity laser experiments [20,21].

2.3 Ultra-Intense Laser Plasma Energy Coupling

One of the key issues critical to the success of fast ignition is the efficient coupling of energy from the short, high intensity laser pulse to the pre-compressed core. However, the laser energy deposition in short pulse, high intensity laser plasma interactions is starkly different from that of classical long-pulse, moderate intensity lasers. Specifically, during the usual long-pulse interactions well-known to the ICF community, the laser heats the plasma such that the impending pressure causes it to blow off or ablate away at approximately the sound speed, $c_s = \sqrt{Z^* T_e / m_i}$. As the plasma expands, a region of coronal plasma is formed in front of the target with an exponentially decreasing density profile whose scale length can be approximated by

$$L = c_s \tau_L \cong 3\left(\frac{T_e}{keV}\right)^{1/2}\left(\frac{Z^*}{A}\right)^{1/2} \tau_{fs}\ \text{Å} \qquad (2.21)$$

In typical ICF experiments, this scale length can be quite long, with coronas extending 100s of microns in front of the plasma and is where most of the laser absorption will take place. For classical long pulse lasers of this type, energy transfer will occur via collisions by the well-known and dominant absorption mechanism of inverse bremsstrahlung. Specifically, as the laser propagates up to the critical surface, its electric field accelerates electrons within the beam volume, though for a given laser cycle, there is no net acceleration. However, in reality, stochastic effects will prevent electrons from completing a full cycle, which will then allow them to acquire a net acceleration. This net acceleration can be translated into a temperature, after which the electrons will then couple to the ions and subsequently transfer energy [8].

Unlike the classical long-pulse laser plasma interaction, energy absorption for short pulse, ultra-intense lasers is not quite so simple. Because of their short pulse length, these laser pulses do not have time to produce the long scale-length plasma corona in front of the target. For example, if a 100 fs Ti:sapphire laser pulse, which is typical of short-pulse laser systems today, were to heat the target to a few hundred eV, one could deduce from equation 2.21 that a pre-plasma of the order of 0.01-0.1 microns would form in front of the target, which is quite steep compared to the 100 micron or so coronas that form in front of the long-pulse targets. As a result, laser energy can be deposited much closer to the target surface at higher densities. However, unlike the classical long-pulse systems, absorption does not occur via collisions. Because the temperature rise in these interactions occurs on such a short time scale, the collision rate is rapidly reduced. More specifically, using simple physical arguments based on classical heat flow and assuming a constant intensity, one can derive an expression for the surface temperature of the target which scales like [22]

$$T_e \propto I^{4/9} t^{2/9}. \tag{2.22}$$

So assuming the collision frequency can be approximated with the Spitzer expression which scales like $T_e^{-3/2}$, the collision frequency is found to fall off quite rapidly, i.e.,

$$\nu_{ei} \sim I^{-2/3} t^{-1/3}. \tag{2.23}$$

In addition, a secondary limiting effect noted by Pert can suppress the collision frequency even further when the electron quiver velocity becomes comparable to the thermal velocity [23]. More specifically, one can derive an effective collision frequency that takes this effect into account, giving

$$\nu_{eff} \cong \nu_{ei} \frac{v_{te}^2}{(v_{os}^2 + v_{te}^2)^{3/2}} \tag{2.24}$$

where v_{te} is the thermal velocity and v_{os} is the oscillation velocity. So given these two limiting effects, laser absorption in the short-pulse high intensity regime cannot rely on collisions. Even though the usual mechanisms, such as inverse bremsstrahlung, that dominate classical long-pulse moderate intensity lasers are dwarfed in the short pulse high intensity regime, a number of collisionless absorption processes turn on in this regime that are capable of coupling laser energy to the plasma [8].

2.4 Collisionless Absorption Mechanisms

As one moves into the short-pulse, high intensity regime, the highly nonlinear and complex nature of the laser plasma interactions give rise to a number of collisionless absorption mechanisms. However, unlike the classical long-pulse, moderate intensity regime, this complexity makes it rather difficult to determine which mechanisms are dominant and where the energy actually gets absorbed. As will be described in the paragraphs that follow, collisionless absorption mechanisms in this regime depend on a number of issues such as laser intensity, pre-plasma scale length, angle of incidence, etc.

One of the oldest and well-known forms of collisionless absorption that can arise in laser plasma interactions is resonant absorption [24]. Although this absorption mechanism can also exist in the classical long pulse moderate intensity regime, it is not quite as dominant as inverse bremsstrahlung. The physical picture normally associated with this mechanism is that of a p-polarized laser pulse that propagates up to the critical surface of the plasma where it then resonantly excites electron plasma waves. These waves will then grow for a few laser periods, after which they will be damped by collisions at low intensities characteristic of conventional ICF experiments or by particle trapping and wave breaking at high intensities characteristic of the fast ignitor scheme [25]. Resonance absorption tends to be a maximum at oblique angles of laser incidence and for long pre-plasma density scale-lengths [8]. As a result, it is unclear how dominant this mechanism is for the short laser pulses relevant to fast ignition since these laser plasma interactions tend to have rather steep density gradients, as explained previously.

Another mechanism known as Brunel absorption or vacuum heating can arise in the short pulse high intensity regime that is quite similar to classical resonant absorption, the main difference being that it arises in short-scale length pre-plasmas [26]. Like resonant absorption,

electrons are driven into the plasma by the electric field of the laser pulse along the density gradient. However, for scale lengths less than the laser wavelength, resonance cannot exist, though there is still a way to couple the laser energy to the plasma. More specifically, the physical picture of Brunel absorption is one in which the short scale length of the plasma allows electrons near the edge to be directly exposed to the laser electric field. In other words, a thermal electron near the vacuum-plasma interface at the right moment of the laser cycle may be accelerated into vacuum by the laser electric field and as the field reverses direction, it will then be accelerated back into the plasma. However, because the laser electric field only penetrates into the plasma to within a skin depth of the overdense plasma, the electron can traverse the remainder of the target unaffected by the laser electric field, after which it will be absorbed by collisions [8]. So for the short scale length plasmas expected for fast ignition scenarios, Brunel absorption may be of great significance.

As was mentioned previously, intensities greater than 10^{18} W/cm^2 give rise to relativistic effects which can affect the electron trajectory in the laser fields. It was shown in Section 2.2 that for intensities in this regime, the ponderomotive force develops a longitudinal component that will push electrons in the direction of the laser. Physically, this occurs when the $\vec{v} \times \vec{B}$ term begins to exceed the electrostatic term, which results in purely transverse motion. The mechanism of energy coupling that arises from this longitudinal component of the ponderomotive force is known as $\vec{J} \times \vec{B}$ heating. Unlike Brunel absorption, which utilizes the electric field of the laser to accelerate electrons, $\vec{J} \times \vec{B}$ heating utilizes the oscillating component of the ponderomotive force to accelerate electrons into the plasma at the critical surface. Given that this absorption mechanism tends to be dominant for laser pulses at normal incidence and high intensities, it is of particular significance for fast ignition applications [8].

2.5 Hot Electron Generation

As has been shown, a wide range of absorption mechanisms can arise as laser intensities transition into the high intensity regime relevant to fast ignition. However, because the interaction physics surrounding each mechanism is so highly dependent on conditions such as laser intensity, target material, contrast ratio, angle of incidence, pre-plasma scale-length,

etc., isolating a single dominant mechanism in an experiment or simulation could be quite challenging. Despite the rather lengthy list of competing effects, though, one can safely assume that the combination of these effects will result in the superheating of some fraction of the plasma electrons to energies much higher than the initial bulk temperature [8]. Because ultra-intense laser applications such as fast ignition rely on efficient coupling the laser energy to the plasma, determination of this hot electron temperature is a crucial issue.

Although a comprehensive theoretical model for determining the hot electron temperature is not yet possible, a number of authors have derived theoretical scaling laws based on the assumption of a single dominant absorption mechanism or a single physical concept. For example, if one were to assume that Brunel absorption (vacuum heating) were dominant for a given configuration, a simple electrostatic model of the electrons being accelerated directly by the laser field would yield the scaling law

$$T_h^B(keV) \cong 3.17 I_{16} \lambda_\mu^2, \tag{2.25}$$

where I_{16} is the intensity in units of $10^{16}\mathrm{Wcm}^{-2}$ and λ_μ is the wavelength in microns [27]. However, Gibbon and Bell extended this model to include electromagnetic effects with support from PIC simulations to yield the slightly improved scaling law [28]

$$T_h^{GB}(keV) \cong 7(I_{16}\lambda^2)^{1/3}. \tag{2.26}$$

Other authors have derived scaling laws based on an assumption of pressure balance between the laser and plasma, though this is more applicable to long laser pulse configurations. Specifically, Forslund, Kindel, and Lee used this concept, along with the support of PIC simulations that ensured an initial pressure balance, to derive the scaling law [29]

$$T_h^{FKL}(keV) \cong 14(I_{16}\lambda_\mu^2)^{1/3} T_e^{1/3}. \tag{2.27}$$

A similar scaling was also formulated by Beg et al. [30] from experimental data, known as the Beg scaling law, and is given by

$$T_h^{Beg}(keV) \cong 100(I_{17}\lambda_\mu^2)^{1/3} . \tag{2.28}$$

Although this scaling law is phenomenological, rather than theoretical, in nature, it has been widely used for estimating hot electron temperatures for lasers with peak intensities in the moderate to high intensity regimes.

Finally, one of the more successful scaling laws that has been derived is that of Wilks et al. and is based on the assumption that $\vec{J} \times \vec{B}$ heating is the dominant absorption mechanism for intensities above 10^{18} W/cm^2. Because the longitudinal component of the ponderomotive force is the driving mechanism for this type of absorption mechanism, Wilks et al. [20] used the argument that the hot electron temperature takes the form, $T_h \propto e\phi_p$, where ϕ_p is the ponderomotive potential. Using this assumption and the relativistic form of the ponderomotive force, one can write

$$T_h^W \cong mc^2(\gamma - 1) . \tag{2.29}$$

Since the relativistic gamma factor can be easily re-expressed in terms of the oscillation momentum, $\gamma = \sqrt{1 + p_{osc}^2 / m^2c^2}$, the scaling law then becomes

$$T_h^W \cong mc^2\left(\sqrt{1 + \frac{p_{osc}^2}{m^2c^2}} - 1\right). \tag{2.30}$$

This can be written more conveniently in terms of the laser intensity as

$$T_h^W(keV) \cong 511\left[(1 + 0.73I_{18}\lambda_\mu^2)^{1/2} - 1\right] \tag{2.31}$$

and is conventionally known as the ponderomotive scaling.

In **Fig. 2.6** below, one can see the theoretical scaling laws described above (with the exception of the Beg Scaling law) which have been superimposed onto experimental data points from hot electron measurements performed over the last decade. As one can see, there is a clear

dependence on $I\lambda^2$, as was predicted by theory. Additionally, there appears to be two distinct intensity regimes: a moderate intensity regime ($I\lambda^2 = 10^{15} - 10^{17} Wcm^{-2}\mu m^2$), in which the Brunel/vacuum heating scaling laws apply, and a high intensity regime ($I\lambda^2 > 10^{18} Wcm^{-2}\mu m^2$), where the ponderomotive scaling applies [8]. In fact, the accuracy of the ponderomotive scaling at relativistic intensities is quite good.

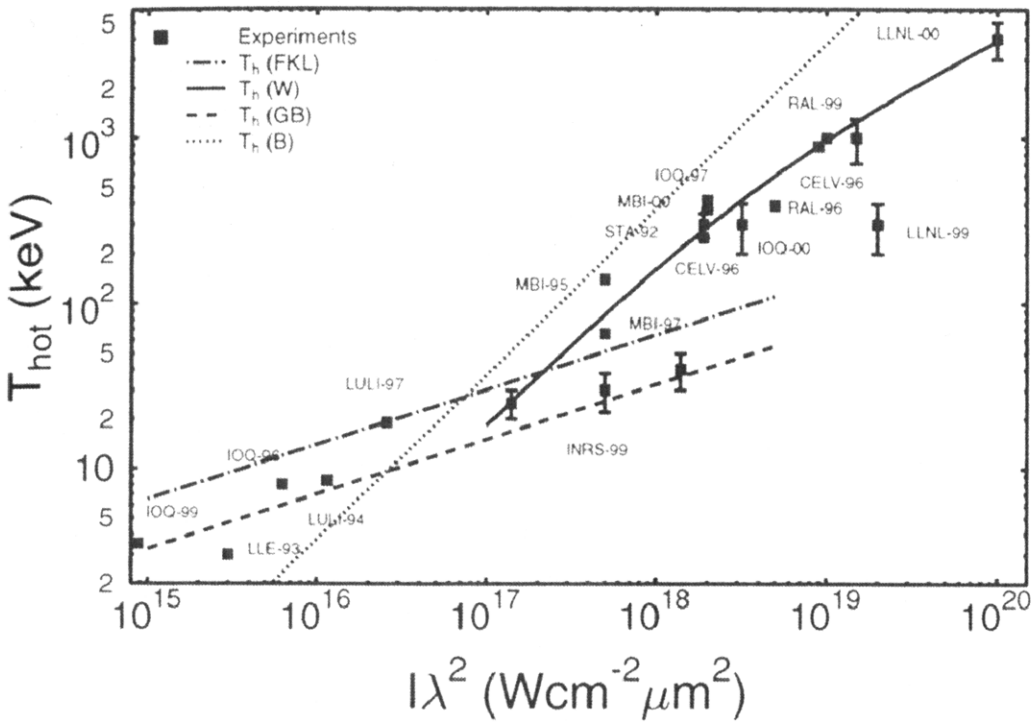

Fig. 2.6. Measurements of hot electron temperature from short-pulse, high intensity laser experiments performed over the last decade overlaid with theoretical scaling laws [8].

2.6 Hot Electron Transport

In order to satisfy the ignition requirements for fast ignition, it has been shown that laser pulses of the order of a petawatt will be needed. Translated to particle beam requirements, this would correspond to electron currents of the order of 100's of mega-amps to 1 giga-amp and/or electrons of the order of an MeV. When dealing with currents of such extreme magnitude, a number of transport issues such as resistive inhibition, beam-plasma instabilities, and other current limitations can arise that can act to inhibit efficient energy transport.

Although the transport of laser energy to the fuel core via a giga-amp electron beam is an appealing prospect, it is not a realistic one. As Bell et al. pointed out, a beam of this magnitude cannot exist because the magnetic field it would produce would become unphysical [31]. What occurs instead is the generation of a return current. As the electrons are rapidly accelerated by the laser from the focal spot, a large charge imbalance is created since the ions are essentially immobile on this time scale. Before any more electrons can be accelerated from the region, the charge imbalance must be compensated. The plasma provides this compensation in the form of a return current in the opposite direction to approximately cancel the forward hot electron current and establish current neutrality. As a result, the magnetic field is reduced to physically reasonable quantities. However, in a cold, solid-density plasma, a finite resistivity will exist, resulting in the generation of an electric field. Because this electric field is in the direction opposite of the hot electron beam, it can inhibit transport of the beam.

Another shortcoming to this return current is that the counter-streaming current configuration it creates is vulnerable to a number of beam-plasma instabilities, namely, the two-stream, Weibel [32], and filamentary instabilities. These instabilities will evolve through a linear growth phase, followed by a nonlinear saturated state. For clarity, it suffices to outline the basic physics and geometry of each instability. The two-stream instability, the simplest of the three, is a 1D electrostatic instability with the wave vector **k** aligned parallel to the beam direction, as shown in **Fig. 2.7**. When an initial perturbation is applied in the direction of the counter-streaming beams, a charge density perturbation , $\delta\rho$, is created that then leads to a longitudinal electric field perturbation, $\boldsymbol{\delta E}$, subsequently reinforcing the initial perturbation and creating the longitudinal "electron bunching" phenomenon. The filamentary instability, which

is more of a concern for relativistic beams, is an electromagnetic instability with **k** aligned perpendicular to the beam direction (see **Fig. 2.7**). When an initial perturbation is applied perpendicular to the counter-streaming beams, a current density perturbation, **δJ**, is created that then leads to a magnetic field perturbation, **δB**, subsequently reinforcing the initial perturbation and creating the familiar effect of current filaments. Unlike the two-stream and filamentary instabilities, the Weibel instability, in its original derivation, is not driven by the counter-streaming motion of the beams, but is an electromagnetic instability driven by the temperature anisotropy of the beam distributions [32]. When a beam distribution is initiated with a perpendicular temperature, $T_\perp \geq T_\parallel$, a preponderance of electrons will exist with $v_{th\perp}$ that will lead to a perturbed current density, **δJ**, perpendicular to the beams. This current density will then generate a magnetic field perturbation, **δB**, that reinforces the perturbation along the beam direction.

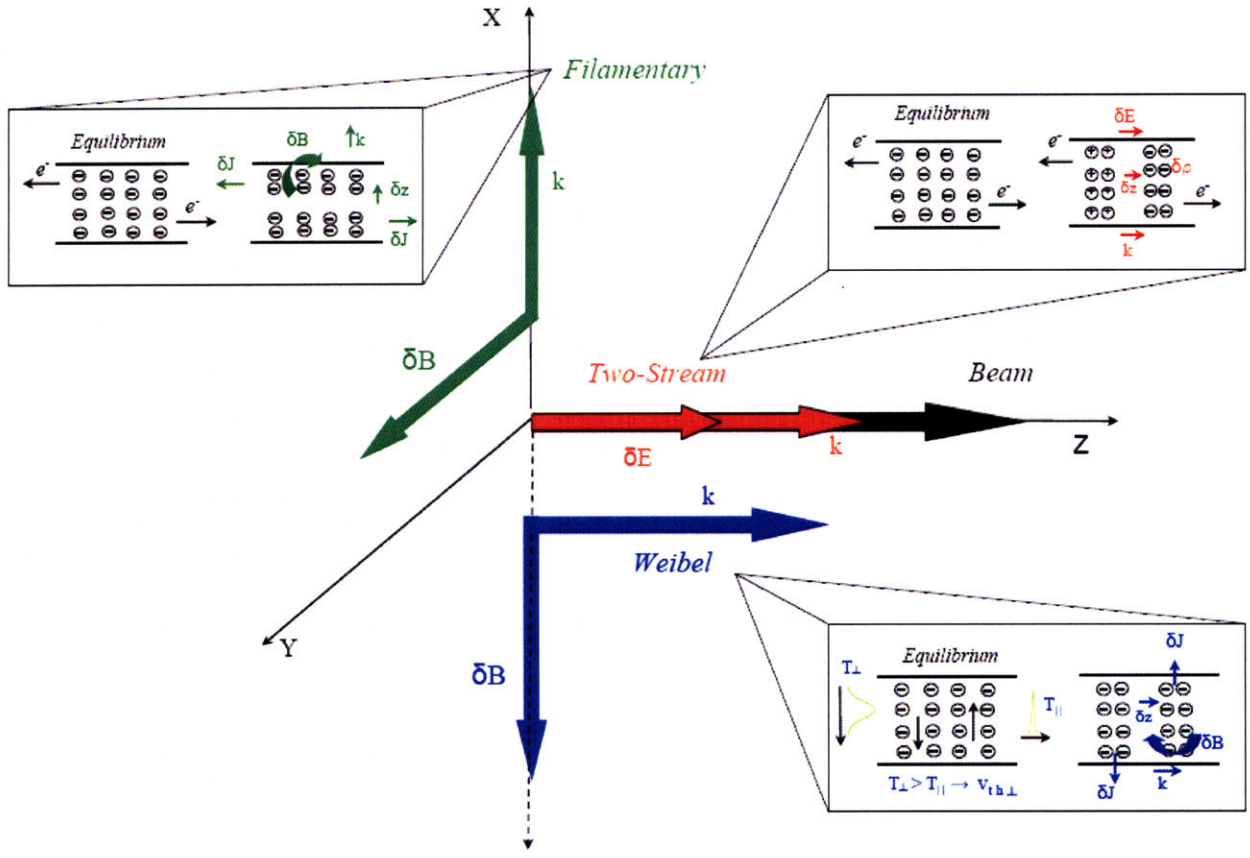

Fig. 2.7. Critical beam instabilities for fast ignition

Another obstacle to hot electron beam transport for fast ignition applications is the Alfvén current limit [33]. As was mentioned previously, currents of the order of a giga-amp and energies of the order of an MeV will be required to reach ignition conditions for the fast ignitor scheme. In general, charged currents transported in vacuum face a current limit known as the Alfvén limit. When this limit is exceeded, the current is capable of generating magnetic fields large enough such that the Larmor radius of the electrons become smaller than the beam radius. At this point, the beam electrons are no longer transported in the original direction of the beam. Quantitatively, this limit is given by

$$I_A = 17\beta\gamma \ \ kA. \tag{2.32}$$

So for the 1 MeV electrons required for the fast ignition scheme, the Alfvén limit would be approximately 47 kA, which is over 20,000 times smaller than the giga-amp currents required for ignition.

Because beam filamentation is an inevitable phenomenon that can arise in the counter-streaming current scenario, a number of related transport issues begin to develop. As was mentioned previously, return currents will act to screen the local magnetic field by enveloping each beam filament. However, because this screening is not perfect, the filaments will eventually begin to attract one another and coalesce into larger filaments [34]. Although this coalescence might initially seem like an appealing feature, problems can arise when these larger filaments approach the Alfvén current limit. The Alfvén limit does not apply globally, but locally, to beam transport and each current filament is not able to exceed this limit by a rather large factor. As a result, when the filaments begin to merge, the combined current can become larger than I_A. To rid itself of directed current, the filament then disperses some of its beam power into transverse energy. Because the filaments loose directed beam power with each coalescence event, the beam's directed power decreases with time [4]. This phenomenon has yet to be understood completely and will be one of the issues to be examined in this thesis in the chapters that follow that will investigate beam transport in the collisionless and collisional limits.

Chapter 3

Numerical Simulations

Because of the complex, highly nonlinear nature of the conditions expected for fast ignition, fluid models are insufficient for analyzing hot electron generation and transport. Thus, in order to incorporate all of the necessary physics, a self-consistent kinetic model is essential. The simplest kinetic model one could construct for numerical analysis would be that of the Vlasov equation in which particle species are represented by a six dimensional distribution function $f(\vec{x},\vec{\mathrm{p}})$ and evolve according to

$$\frac{\partial f}{\partial t}+\vec{\mathrm{v}}\cdot\frac{\partial \mathrm{f}}{\partial \vec{\mathrm{x}}}+q(\vec{E}+\frac{\vec{\mathrm{v}}}{\mathrm{c}}\times\vec{B})\cdot\frac{\partial f}{\partial \vec{p}}=0 \qquad (3.1)$$

via continuum methods. However, for most practical purposes, this model is rather unappealing for numerical simulation due to its intractability for multidimensional problems. Even for one-

dimensional space geometries, several velocity components normally must be retained in order to properly couple to Maxwell's equations, making the numerical integration still rather cumbersome [8].

On the contrary, a much more appealing alternative is that of particle-in-cell (PIC) simulation. Developed in the 1950's and 60's, PIC simulation has become an invaluable tool for understanding plasmas, specifically in the field of laser-plasma interactions and particle transport [35]. In addition to enabling one to model kinetic (non-Maxwellian) effects, this technique has the added appeal of easier numerical implementation. Like continuum Vlasov codes, PIC codes also solve the Vlasov equation, but rather than discretize in all dimensions, they only discretize in space and sample the momentum space coordinates by convecting PIC particles. In the last several decades, PIC codes have evolved in both sophistication and availability in this field. In fact, these types of numerical experiments are commonly relied upon before actual (more expensive) laboratory experiments are performed. For the purposes of this document, results and discussion will be limited to a sophisticated PIC code known as LSP (Large-Scale-Plasma), though many of its features can be found in several other codes that exist throughout the research community [36]. The LSP code, which was originally developed by Mission Research Corporation for use in the ion beam community, is one of the few PIC codes capable of including all the relevant physics necessary to model the fast ignition transport problem of interest. LSP is a fully 3D/3V electromagnetic hybrid particle-in-cell (PIC) code which includes relativistic effects, as well as collisional effects. The code can also be used for single and multi-dimensional geometries, in either Cartesian or cylindrical coordinate systems, and has a user settable option of using either an explicit or implicit particle push algorithm, as will be explained.

3.1 Introduction to PIC simulation

The basic idea behind the PIC method of plasma simulation is the discretization of a real laboratory plasma in space and time such that its numerical evolution captures the essential physics of that of the real laboratory plasma. In addition, each charged particle in the system becomes a homogeneous collection of a large number of real-plasma charges, or macro-particle, always multiply charged and greater in mass, but with a charge-to-mass ratio that remains the

same as that of the real charge. So unlike a real laboratory plasma, a PIC-simulated plasma evolves discontinuously using temporal and spatial grids, with the field and particle physics being recomputed each time step at each spatial grid point using Maxwell's equations and the Newton-Lorentz equation of motion, respectively. The appeal of PIC simulation lies in the ability to make mathematical simplifications that are not necessarily physical but allow for extraction of the essential physics of the problem at hand. For example, the temporal grid is normally chosen such that it is sufficiently fine grained so as to resolve only the plasma or cyclotron frequencies of the species of interest for a given problem. Although higher frequencies may be present, the finer grained behavior can safely be omitted if their information is not vital to the problem at hand. Similarly, nearly all of the plasma physics that is done requires only knowledge down to some spatial scale, such as the Debye length, allowing one to neglect finer grained behavior. So in sum, PIC simulation relies on many mathematical simplifications that allow for ease of implementation. Although some of these simplifications can lead to nonphysical effects, one can avoid many of these issues by ensuring that numerical methods maintain both accuracy and stability and parameters are chosen with care [37].

Although PIC schemes may vary from one code to another, one of the more common and easily understandable PIC cycles is outlined in **Fig.3.1**. Each simulation begins with some set of initial conditions for the plasma, such as particle positions and velocities. Particles are normally kept track of with some type of serial number or index, such as i in the figure, and may take on any value in v and x space. Field quantities, on the other hand, are known only at discrete points located on the spatial grid, which are indexed as j in the figure. So to begin the cycle, the code must map the local particle positions to the grid in order to compute an initial charge and current density to be used in Maxwell's equations. This is done with a type of weighting function which depends on particle positions and describes the effective shape of the particles. With this weighting, charge and current densities can be used to solve Maxwell's equations in order to obtain the electric and magnetic fields at the grid points. However, because the fields are only known at the grid points and the particles are scattered throughout phase space, the fields must be interpolated from the grid to the local particle positions using the same type of weighting function. Finally, the particles are then "pushed" and their new

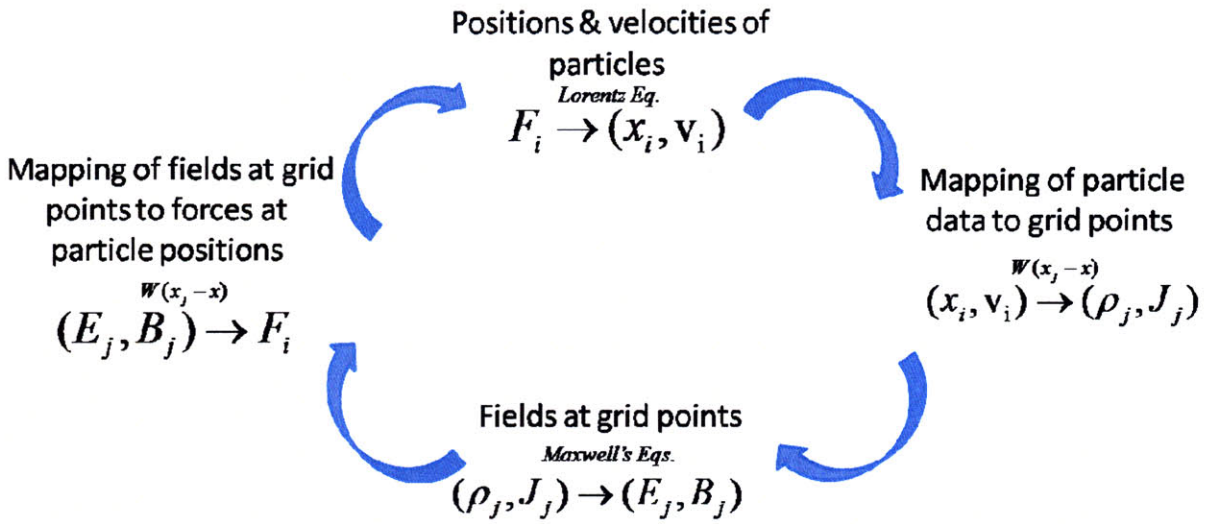

Fig. 3.1. Schematic of the PIC cycle.

positions and velocities are computed, after which the cycle repeats itself for each time step until the simulation runs to completion [8,37].

Because the interpolation between the continuous particle positions and the discrete grid points plays such an important role in computing the particle forces and fields, an accurate weighting function is desirable. The simplest weighting scheme one could implement consists of "zero-order" or "nearest-grid-point" weighting. The basic idea behind this type of weighting is that all particles within one cell width of a given grid point are included in the calculation of the charge density at that point, resulting in particles of rectangular shape. Although this scheme is computationally efficient, as it requires only one grid look-up, it has the disadvantage that density and fields are relatively noisy in space and time due to the abrupt jump in density as particles pass through the cell boundaries. A more accurate weighting scheme used in most PIC codes is that of "first-order" or "cloud-in-cell" weighting [38]. In brief, this weighting scheme linearly distributes particles between grid points such that a larger fraction gets associated with the nearest grid point. Although this type of weighting does require additional computational work, it allows for a smoothing of the density and field fluctuations, thus reducing the noise, compared to zero-order weighting [37]. Higher order schemes are also used, such as the novel 4^{th} order scheme by Y. Sentoku that allows for larger spatial scales compared to the Debye length, but those are beyond the scope of this work [39].

3.2 Explicit PIC Algorithm

One of the essential elements of the PIC scheme is the method by which the equations of motion and Maxwell's equations are solved to both push the particles and solve for the electromagnetic fields. For an algorithm to be suitable for plasma simulation, it must be both efficient and accurate. One of the most commonly used PIC algorithms is known as the explicit or "leap-frog" scheme [37]. The appeal of this scheme is that it is not only simple and accurate, but also requires minimum computational storage. The basic idea behind the explicit PIC algorithm revolves around the use of finite differencing. In other words, approximations to derivatives of a function, f, such as $\partial f / \partial x$, $\partial^2 f / \partial x^2$, etc., enable one to solve equations algebraically. More specifically, finite differencing allows functional derivatives to be computed at a grid point, i, as

$$\frac{\partial f}{\partial x}|_i = \frac{f_{i+1} - f_{i-1}}{2\Delta x} + O(\Delta x^2) \tag{3.2}$$

where Δx is the grid spacing. Although this is second order accurate, it has the disadvantage of being decoupled from adjacent grid points, so a more commonly used technique for PIC defines gradients at the midpoints of the mesh, i.e.,

$$\frac{\partial f}{\partial x}|_{i+1/2} = \frac{f_{i+1} - f_i}{\Delta x} + O(\Delta x^2) \tag{3.3}$$

which allows for "centering" about the grid point of interest [8].

With this in mind, one can reconstruct both the Lorentz equation and Maxwell's equation using finite differencing. As a simple example, one can begin with the 1D-1V electrostatic configuration [8]

$$\frac{d\vec{v}_i}{dt} = \frac{q_i}{m_i}\vec{E} \tag{3.4}$$

$$\frac{d\vec{x}_i}{dt} = \vec{v}_i \tag{3.5}$$

which can be re-expressed using finite differencing as

$$\mathrm{v}_{\mathrm{i}}^{\mathrm{n+1/2}} = \mathrm{v}_{\mathrm{i}}^{\mathrm{n-1/2}} + \frac{q_i}{m_i} E_i^n \Delta t \tag{3.6}$$

$$x_i^{n+1} = x_i^n + \mathrm{v}_{\mathrm{i}}^{\mathrm{n+1/2}} \Delta t \tag{3.7}$$

$$E_{j+1/2}^{n+1} = E_{j-1/2}^{n+1} + \rho_j^{n+1} \Delta x \,, \tag{3.8}$$

where ρ_j^{n+1} is the charge density obtained from the linear area weighting function W by

$$\rho_j^{n+1} = \sum_i q_i W(x_i - x_j) \tag{3.9}$$

$$W = 1 - \frac{|x_i - x_j|}{\Delta x} \,. \tag{3.10}$$

A schematic of this differencing scheme is shown in **Fig.3.2**. As one can see, velocity and position are not known at the same time, which is a result of the centering restriction. One can extend this to an electromagnetic configuration using a centered explicit difference scheme known as the Boris pusher, which is the heart of most explicit PIC codes used today. The trick used by Boris consists of splitting the electromagnetic forces acting on the particle into a linear acceleration (electric field) and a rotation (magnetic field) component [8]. Although the details are beyond the scope of this document, an overview of the Boris pusher has been detailed in Appendix A for interested readers.

Although the explicit algorithm is an attractive scheme due to its simplicity and accuracy, it does have the disadvantage of requiring high spatial and temporal resolution. More specifically, explicit algorithms such as the leap-frog scheme are numerically stable only if the

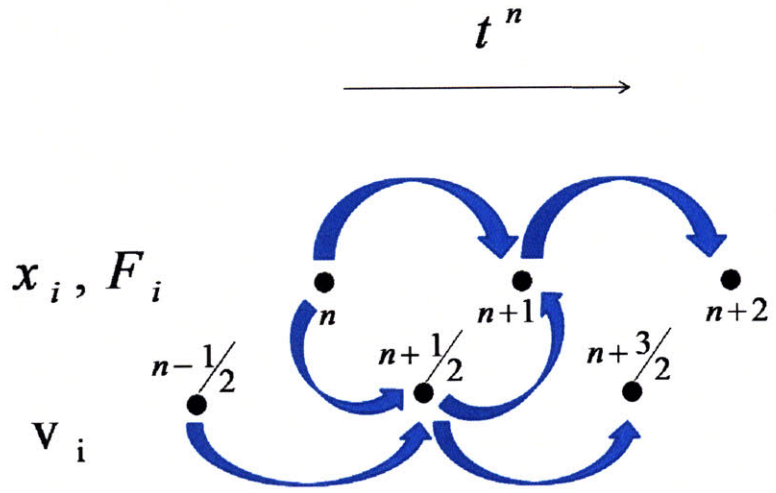

Fig. 3.2. Schematic of the explicit PIC leap frog algorithm.

fastest physical time scales of waves are resolved, such as ω_p^{-1} and ω_c^{-1}, not to mention the fastest particle motion time scale, which is the transit time for electrons or light to cross a characteristic distance. In addition, spatial scales are limited to the resolution of the Debye length to prevent non-physical effects, such as numerically heating, that arise when the cell size is less than this spatial scale [37]. However, as will be discussed in the section that follows, alternative schemes have been developed that will allow one to sidestep these limitations.

3.3 Implicit PIC Algorithm

The explicit algorithm outlined in the previous section has and continues to play an invaluable role in plasma simulation with its ability to simply and accurately model the kinetic evolution of plasmas on fast time scales. However, it is often the case that one would like to extract physics that evolve on slower time scales without having to resolve other high frequency effects that are not of interest. Because of the temporal and spatial constraints of explicit PIC algorithms, they are not adequate for extracting these types of physics, as they would require long simulation runs. On the other hand, "implicit" algorithms, as they are often referred, have

been developed such that unwanted high frequency modes are selectively damped and are numerically stable for large time steps and long simulation times [40].

One of the initial challenges of the implicit algorithm is choosing a set of finite difference equations for particle advance that can both accurately resolve the physics of interest at low frequency and are stable for large time steps. One of the more popular schemes in use is referred to as the D_1 algorithm, which was originally developed by Cohen, Langdon, and Friedman in 1982 [41]. The finite difference equations are as follows:

$$x_{n+1} = x_n + \Delta t * \mathrm{v}_{\mathrm{n+1/2}} \tag{3.11}$$

$$\mathrm{v}_{\mathrm{n+1/2}} = \mathrm{v}_{\mathrm{n-1/2}} + \Delta t a_n + \frac{\Delta t}{2}\left(\mathrm{v}_{\mathrm{n+1}} - \mathrm{v}_{\mathrm{n-1/2}}\right) \times \frac{qB_n}{mc} \tag{3.12}$$

where

$$a_n = \frac{1}{2}\left[a_{n-1} + \frac{q}{m} E_{n+1}(x_{n+1})\right]. \tag{3.13}$$

As one can see in the acceleration term, the future electric field term, E_{n+1}, depends on the future particle positions. However, because these positions are currently unknown, a large system of coupled nonlinear equations must be solved. So unlike the explicit scheme, which neatly separates the particle push and field calculations, implementation of the implicit scheme relies on first finding an accurate and efficient way to solve this complex system of equations [37].

Implicit techniques generally fall into two categories, moment and direct, which are distinguished by the method used to solve the system of coupled equations. The moment method, which is the earlier and simpler of the two, relies on the continuity and fluid equations to obtain an initial approximation of the electromagnetic field. The positions and velocities of the particles are then advanced by these approximate field quantities, after which the current and charge density source terms are then recomputed or updated with the new particle data. In contrast, the direct method, which is an improvement upon the moment method, involves computing the future electromagnetic fields "directly" with the particle and field equations by

expanding them about an estimate obtained from data at earlier times. A predictor-corrector scheme then recomputes the field quantities and adjusts the remaining data accordingly [40].

Because the LSP code utilizes the direct implicit scheme, I will provide a detailed overview of this algorithm only. In general, this scheme is very complex in its fully relativistic electromagnetic form, so for brevity, the simplest implicit scheme consisting of the 1D electrostatic limit will be examined, while the interested reader is referred to Appendix B for the more complicated multi-dimensional electromagnetic case. As mentioned previously, the particle motion and field equations are linearized about an approximation for data variables at the new time step, $n+1$. The corrections or increments of these variables depend on the unknown quantities at the new time step. So one can begin by expressing the future position of a particle by

$$x_{n+1} = \frac{1}{2}\Delta t^2 a_{n+1} + \tilde{x}_{n+1}, \tag{3.14}$$

where $\tilde{x}_{n+1}$ is the position of the particle obtained from the finite difference equations by omitting the acceleration term at the next time step, a_{n+1}. In other words,

$$\tilde{x}_{n+1} = x_n + \mathrm{v}_{\mathrm{n\text{-}1/2}}\Delta t + \frac{1}{2}a_{n-1}\Delta t^2, \tag{3.15}$$

which means that, mathematically, the particle positions will be determined by a linearization about $\tilde{x}_{n+1}$ such that $E^0_{n+1} = 0$ and $x^0_{n+1} = \tilde{x}_{n+1}$. So from these equations, the unknown quantity is the acceleration at the next time step, which can be rewritten from the particle equations of motion as

$$m_i a_{i,n+1} = q_i \Delta x \sum_i E_{j,n+1} W(X_j - \tilde{x}_{i,n+1}), \tag{3.16}$$

where W is the weighting function described previously, i refers to the individual particle, and j refers to the grid point located at $X_j = j\Delta x$. As one can see, the only remaining unknown quantity is E_{n+1}, which can be related to the charge density, ρ_{n+1}, through Gauss's Law

$$\nabla \cdot E_{n+1} = \rho_{n+1} = \tilde{\rho}_{n+1} + \delta\rho. \tag{3.17}$$

Because the extrapolated charge density, $\tilde{\rho}_{n+1}$, can be expressed as

$$\tilde{\rho}_{j,n+1} = \sum_i q_i W(X_j - \tilde{x}_{i,n+1}), \tag{3.18}$$

W can then be expanded to obtain an expression for the charge density increment, $\delta\rho_{n+1}$, as

$$\delta\rho_{n+1} = -\sum_i q_i \delta x_i W'(X_j - \tilde{x}_{i,n+1}) \tag{3.19}$$

By re-expressing equation 3.19 as,

$$\delta\rho = -\nabla \cdot (\tilde{\rho}\delta x) \tag{3.20}$$

and substituting back into Gauss's Law, one can obtain an elliptical partial differential equation for the extrapolated charge density, i.e.,

$$-\tilde{\rho} = \nabla \cdot \{[1 + \chi(x)]\nabla\varphi\}, \tag{3.21}$$

where $\chi(x) = \tilde{\rho}(x)(q/2m)\Delta t^2$ is defined as the implicit susceptibility. Finally, by rewriting the equation $\delta\rho = -\partial(\chi E)/\partial x$ as a finite difference equation, the resulting equation is

$$\tilde{\rho}_{j,n+1} = \frac{(1+\chi_{j+1/2})E_{j+1/2,n+1} - (1+\chi_{j-1/2})E_{j-1/2,n+1}}{\Delta x}. \tag{3.22}$$

As one can see, knowledge of $\tilde{\rho}$ and χ results in a system of linear equations that can then be solved for the electric field. Once this field is known, the particle positions and velocities can then be advanced. To summarize, the direct implicit method results in pushing the particles twice, the first time using an approximation for the unknown time advanced field, and the second time using a corrected field which is computed by evaluating the error in satisfying the implicit field equations [37]. Needless to say, the direct implicit algorithm is rather complicated, even for the simplest 1D electrostatic scheme. As a result, the more complex 3D relativistic electromagnetic scheme that is utilized in the LSP code has been outlined in the Appendix B for interested readers.

In sum, the direct implicit method is more complex to solve than the explicit algorithm. However, one of the main advantages of the direct implicit algorithm is that it enables larger time steps than conventional explicit PIC codes, which must resolve the plasma frequency and Debye length. This allows solid density, colder plasmas to be modeled. Such plasmas are more

collisional and so LSP incorporates inter- and intra-species collisions, which will be discussed in a later section [42].

3.4 Hybrid Fluid Kinetic Model

Implicit PIC codes exhibit numerical cooling if large timesteps are used and if particles cross more than half a cell in a time step. Introducing the fluid equation prevents this from happening and allows LSP to model dense, cold plasmas with large timesteps. In the hybrid mode, LSP permits electrons to be represented as either kinetic or fluid particles. In the fluid description, the electrons are assumed to have an internal Maxwellian distribution that can be represented by a temperature. This temperature is advanced by a separate energy equation, and a pressure gradient term is also added to the equation of motion, as shown in the equation that follows:

$$\frac{3}{2}n_e\frac{dT_e}{dt} = -n_eT_e\nabla\cdot v_e + \sum_j \frac{2m_en_e}{m_j\tau_{je}}(T_j - T_e) + \nabla\cdot\kappa\nabla T_e + Q_e - n_e\frac{dE_{ie}}{dt} \quad (3.23)$$

At present, the criteria for a fluid electron to become a kinetic one is that the particle's directed energy ($\frac{1}{2}m_e\mathrm{v}_e^2$) be much greater than its internal energy ($\frac{3}{2}kT_e$). More specifically, fluids transition to kinetic electrons if

$$\frac{1}{2}m_e\mathrm{v}_\mathrm{e}^2 >> \frac{3}{2}kT_e \quad (3.24)$$

and kinetic electrons transition to fluid electrons if

$$\frac{1}{2}m_e\mathrm{v}_\mathrm{e}^2 << \frac{3}{2}kT_e \text{ and } \omega_p\Delta t > 1. \quad (3.25)$$

Given that the fluid model is non-relativistic and breaks down as the fluid electron internal energy approaches the electron rest mass energy, fluid particles that approach such energies (generally > 10keV) are forced to transition to kinetic, regardless of energy conservation. This is for numerical convenience and is not intended to model runaway electrons [42].

3.5 Energy Conservation

Based on the implicit hybrid scheme discussed in the previous sections, LSP will conserve momentum exactly but not energy. The reason for this is a result of the numerical heating and cooling that can occur in particle-in-cell codes. More specifically, explicit PIC codes will numerically heat until the Debye length is roughly the cell size. On the other hand, implicit PIC codes, such as LSP, that do not require the Debye length to be resolved, can exhibit numerical cooling due to the large time steps and if particles are to cross more than half a cell in a time step. LSP uses the hybrid fluid model to overcome this problem. Thus, there is a balancing act between heating and cooling in LSP's numerical scheme such that there is an optimal time step for good energy conservation. In addition, we monitor the energy non-conservation as a function of simulation time to ensure that the results are still meaningful. With careful choice of spatial resolution and time step size, it is possible to maintain energy conservation to approximately 10% or less.

3.6 Collision Model

Up to this point, the discussion of PIC algorithms and their various components, both general and specific to LSP, has made no mention of collisions. However, one of the unique attributes of the LSP code is that in addition to its many other advanced features, it not only includes collisions, but also has the user option of turning them on and off. The original version of LSP contains a grid-based collision model developed by Jones et al. [43] which utilizes the Langevin formalism

$$\Delta\vec{v} = \vec{F}_d \Delta t + \sqrt{D} * N[0,1), \tag{3.26}$$

where N is a randomly chosen number from a uniformly distributed distribution between [0,1). This model uses velocity independent friction and diffusion coefficients, i.e.,

$$\vec{F}_d = -m\nu\vec{v} \tag{3.27}$$

$$D = 2\nu T / m \tag{3.28}$$

and includes inter- and intra-species collisions using Spitzer collision frequencies. According to Jones et al., this collision model was designed to statistically conserve momentum and energy, i.e., energy and momentum conservation can be improved by increasing the number of particles per cell. A more quantitative understanding of this statement was obtained by some simple tests with the LSP code. As shown in **Fig. 3.3**, energy conservation for a typical 1D benchmarking simulation is shown to be optimum in the collisionless limit; however, when collisions are turned on, it improves with increasing particles-per-cell, though little change is observed above approximately 500 particles per cell. For larger, multi-dimensional problems, this technique of boosting the number of particles-per-cell to improve energy conservation can become computationally expensive.

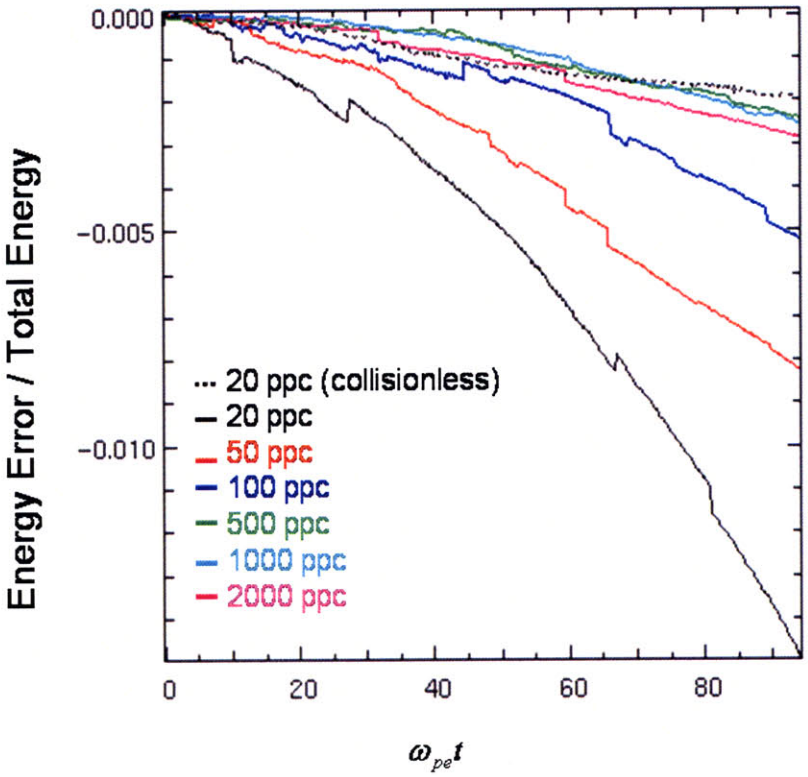

Fig. 3.3. Energy conservation for a sample 1D LSP simulation instability benchmarking case in the linear growth regime for the collisional and collisionless regimes for various particles-per-cell (ppc).

In addition to energy conservation issues, the Jones et al. collision model possesses a number of other vices that have been noted in a number of other publications throughout the literature [44]. For example, the model utilizes Spitzer collision frequencies, which, as one knows, is based on averages over an assumed Maxwellian velocity distribution for both the test and field electrons. Although this may be a reasonable approximation for many problems, Coulomb scattering is realistically a highly anisotropic process, resulting in the parallel component of the diffusion tensor, $D_{\parallel}$, being much smaller than the perpendicular component, $D_{\perp}$. Furthermore, the collision frequency has a velocity dependence that scales as v^{-3}. As a result, if one were to compute the friction coefficient, F_d, with this collision frequency and compare it with the averaged coefficients, the averaged coefficients would be overestimated by over an order of magnitude for supra-thermal electrons [44].

Because of the many issues that have plagued the Jones collision model, we have found it to be insufficient for modeling the problems relevant to this thesis [45]. Recently, we chose to replace this model with an improved Fokker-Planck equivalent Langevin formalism developed by Manheimer et al. [44]. The primary appeal of this model was that it represents the multiple small-angle Coulomb collisions with velocity dependent friction and diffusion coefficients obtained from the actual species' distributions. To begin, it suffices to outline how one goes from the Fokker-Planck equation to the Langevin formalism. For electron-electron scattering, the Fokker-Planck equation is expressed as

$$\left.\frac{\partial f}{\partial t}\right|_{ee} = -\frac{\partial}{\partial \vec{v}} \cdot F_d(\vec{v}) f(\vec{v}) + \frac{1}{2}\frac{\partial^2}{\partial \vec{v}\partial \vec{v}} : f(\vec{v}) f(\vec{v}) \tag{3.29}$$

where

$$F_d(\vec{v}) = \frac{4\pi n e^4}{m^2}\lambda \frac{\partial H}{\partial \vec{v}} \tag{3.30}$$

$$D(\vec{v}) = \frac{4\pi n e^4}{m^2}\lambda \frac{\partial^2 G}{\partial \vec{v}\partial \vec{v}} \tag{3.31}$$

$$\lambda = \ln\left(\frac{1}{2}\csc\vartheta_m\right) \tag{3.32}$$

$$\vartheta_m = 2\tan^{-1}\left(\frac{2e^2}{m\mathrm{v}_e^2\lambda_D}\right) \tag{3.33}$$

$$H(\vec{\mathrm{v}}) = 2\int d^3\tilde{\vec{\mathrm{v}}}\frac{f(\tilde{\mathrm{v}})}{\left|\vec{\mathrm{v}}-\tilde{\vec{\mathrm{v}}}\right|} \tag{3.34}$$

$$G(\vec{\mathrm{v}}) = \int d^3\tilde{\vec{\mathrm{v}}} f(\tilde{\vec{\mathrm{v}}})\left|\vec{\mathrm{v}}-\tilde{\vec{\mathrm{v}}}\right| \tag{3.35}$$

and where v is the scattering electron, or test particle, $\tilde{\mathrm{v}}$ is the scatterer electron, or field electron, and H and G are Rosenbluth potentials [44]. One key simplification that can be made with these equations involves use of the assumption that the scatterer electron distribution is isotropic in its mean frame of reference. This assumption greatly reduces the seemingly intractable integrals in the computation of the friction and diffusion coefficients, yielding

$$F_d(\mathrm{v}) = -\frac{32\pi^2 ne^4}{m^2\mathrm{v}^2}\lambda\int_0^v d\tilde{\mathrm{v}}\tilde{\mathrm{v}}^2 f(\tilde{\mathrm{v}}) \tag{3.26}$$

$$D_{\|}(\mathrm{v}) = \frac{32\pi^2 ne^4}{3m^2}\lambda\left[\frac{1}{\mathrm{v}^3}\int_0^v d\tilde{\mathrm{v}}\tilde{\mathrm{v}}^4 f(\tilde{\mathrm{v}}) + \int_v^\infty d\tilde{\mathrm{v}}\tilde{\mathrm{v}}\, \mathrm{f}(\tilde{\mathrm{v}})\right] \tag{3.37}$$

$$D_{\perp}(\mathrm{v}) = \frac{16\pi^2 ne^4}{3m^2}\lambda\left[\frac{1}{\mathrm{v}^3}\int_0^v d\tilde{\mathrm{v}}\tilde{\mathrm{v}}^2(3\mathrm{v}^2-\tilde{\mathrm{v}}^2) f(\tilde{\mathrm{v}}) + 2\int_v^\infty d\tilde{\mathrm{v}}\tilde{\mathrm{v}}\, \mathrm{f}(\tilde{\mathrm{v}})\right]. \tag{3.38}$$

It should be mentioned that the above assumption remains accurate when the scatterer's distribution function is single-peaked and isotropic to within a 2:1 temperature ratio. If the anisotropy is more extreme, a modified formalism can be implemented which involves representing the scatterer distribution as the superposition of several isotropic distributions displaced by one another in velocity space [44].

With the Fokker-Planck equation in this simplified form, it can then be used as part of the Langevin formalism to efficiently implement Coulomb collisions in a PIC code. In its usual form, the Langevin equation is expressed as

$$\Delta\vec{v} = \vec{F}_d \Delta t + \vec{Q}, \tag{3.39}$$

where now $\vec{Q}$ is a random velocity vector chosen from the distribution

$$P(\vec{Q}) = \frac{1}{(2\pi\Delta t)^{3/2} D_\perp D_\parallel^{1/2}} \exp\left(-\frac{Q_\parallel^2}{2D_\parallel \Delta t} - \frac{Q_\perp^2}{2D_\perp \Delta t} \right). \tag{3.40}$$

In addition, because errors of the order of $(\Delta t)^2$ are inherent in the Langevin equation, energy conservation can be restored by re-expressing the friction coefficient as

$$F_d = F_d \left[1 - F_d \Delta t / (2\mathrm{v}) \right]. \tag{3.41}$$

To allow for ease of implementation in the PIC algorithm, simple Padé approximations have been derived for the friction and diffusion coefficients using a fit with a least-squares determination relative to the error functions [46], i.e.

$$F_D \Delta t / \mathrm{v} = -\nu^* \Delta t / \left[1 + 1.08 (\vec{\mathrm{v}} / \sqrt{2} \vec{\mathrm{v}}_{\mathrm{th}})^{2.46} \right], \tag{3.42}$$

$$D_\parallel / \vec{\mathrm{v}}_{\mathrm{th}}^2 = -\sqrt{D_\parallel} / \vec{\mathrm{v}} \tag{3.43}$$

$$D_\perp / \vec{\mathrm{v}}_{\mathrm{th}}^2 = \nu^* \Delta t / \left[1 + 0.186 (\vec{\mathrm{v}} / \sqrt{2} \vec{\mathrm{v}}_{\mathrm{th}})^{1.85} \right] \tag{3.44}$$

where

$$\nu^* = \frac{2^{7/2} \pi^{1/2} n Z^4 e^4 \ln\lambda}{3m^2 (T/m)^{3/2}}. \tag{3.45}$$

A similar formalism can be derived for electron-ion collisions. However, by assuming the ions are infinitely massive and their velocities are approximately zero, given that they are small compared to the electron velocities, the Fokker Planck coefficients can be reduced to

$$H = \frac{Z_i^2}{\mathrm{v}} \tag{3.46}$$

and

$$G = Z_i^2 \mathrm{v} \,. \tag{3.47}$$

This then leads to the following friction and diffusion coefficients, respectively:

$$F_d = -\frac{4\pi n e^2 Z_i^2}{m^2 \mathrm{v}^2} \lambda \tag{3.48}$$

$$D_{\|}(\mathrm{v}) = 0 \tag{3.49}$$

$$D_{\perp 1}(\mathrm{v}) = D_{\perp 2}(\mathrm{v}) = \frac{4\pi n e^4 Z_i^2 \lambda}{m^2 \mathrm{v}} \,. \tag{3.50}$$

Theoretically, these coefficients are all that is needed for the Langevin equation to compute the changes in velocities. However, it is common procedure to force momentum and energy conservation by neglecting the friction coefficient and instead using the equation

$$(\mathrm{v} + \Delta \mathrm{v}_{\|})^2 + Q_{\perp 1}^2 + Q_{\perp 2}^2 = \mathrm{v}^2 \tag{3.51}$$

to solve for the parallel velocity increment, $\Delta \mathrm{v}_{\|}$ [46].

3.7 Benchmarking

Since a significant fraction of the work contained in this thesis is devoted to instability growth, it is desirable to compare the simulation results with theory for a range of test cases to ensure that it can be trusted for the more complex cases that will inevitably follow. These tests involve the comparison of instability growth rates. As was mentioned in the previous chapter, the two-stream, Weibel, and filamentary instabilities are all relevant to the hot electron transport issues for fast ignition. A convenient way to test a PIC code is to benchmark it with analytical theory. More specifically, one can simulate and extract the linear growth rate of a given instability and then derive the same growth rate analytically using linear perturbation theory for comparison.

To begin the growth rate extraction process for a simulation of a given instability, it is normally convenient to choose a simulation variable that is not only expected to grow, but is also expected to be relatively smooth, such as a field component. For example, it is conventional to choose the longitudinal electric field for the two-stream instability and the transverse magnetic fields for the Weibel and filamentary instabilities. Single normal mode perturbations in continuous linear plasma theory are generally expressed as

$$F(x,t) = \delta F e^{i(k_x x - \omega t)}, \tag{3.52}$$

where δF is the field perturbation amplitude, k_x is the wave number, x is the direction of the wave vector and variation of the field perturbation, and ω is the angular frequency, which is a function of k_x and system parameters. For an instability to be initiated in a simulation, an unstable normal mode must have some non-zero initial projection. This can arise from noise or statistical error in the simulation or it can be initiated with mode seeding. Mode seeding is a process by which a particular mode is chosen and initiated with specified particle velocity and density perturbations. Although mode seeding is the most reliable way to ensure that you grow the mode you want in a controlled way, it is usually only adequate for very simple problems that easily permit one to compute the particle velocity and density perturbations without enormous numerical difficulty. Because many of the problem scenarios relevant to fast ignition will involve beam distributions that are relatively complex, growing instabilities from simulation noise has proven to be more much more practical than mode seeding.

A typical benchmarking simulation is normally set up such that the spatial length corresponds to one wavelength or a multiple of wavelengths of the mode of interest. This allows one to then use the partial Fourier-Laplace transform, expressed as

$$\tilde{F}(k_x,t) = \frac{1}{2\pi}\int_{-\infty}^{\infty} dx F(x,t) e^{-ik_x x} \tag{3.53}$$

to extract the growth mode of interest. As time progresses, the seeded or maximum growth mode will dominate the perturbed field quantity such that we can express this quantity as

$$\widetilde{F}(k_x,t) \cong \widetilde{F}_m e^{\omega_{mi}t} e^{-i\omega_{mr}t} \tag{3.54}$$

where m refers to the maximum growth mode or seeded mode. After squaring, one then has

$$\left|\widetilde{F}\right|^2 \cong \left|\widetilde{F}_m\right|^2 e^{2\omega_{mi}t}, \tag{3.55}$$

which can be re-expressed as

$$\ln\left|\widetilde{F}\right|^2 \cong \ln\left|\widetilde{F}_m\right|^2 + 2\omega_{mi}t. \tag{3.56}$$

As one can see from this equation, by plotting the natural logarithm of the Fourier transform of the field quantity of interest versus time, the growth rate can then be extracted by taking one half of the slope of the curve.

Because the chapters that follow will present growth rates that have been benchmarked with analytical theory, it suffices to show a few simple examples of how this process works. The two simplest examples relevant to this thesis are the two-stream and filamentary instabilities that arise from two cold, relativistic counter-streaming beams. At present, the LSP code does not have the capabilities for mode seeding because the code neutralizes any charge perturbation that is imposed when the problem is initialized. Because of this, the two-stream instability must be grown from simulation noise. However, it is possible to initialize a problem with an applied magnetic field for the filamentary instability. So although one cannot seed this instability exactly with velocity and density perturbations, one can still partially seed the problem with a small applied magnetic field.

The geometry for the cold, relativistic two-stream instability simulation is shown in **Fig.3.4**. Velocity and density parameters were chosen that were both relevant to fast ignition and that would provide a high enough growth rate such that it could be extracted from simulation noise, i.e., $v_b = 0.94c$ and $\alpha = n_b / n_p = 0.1$. The analytical dispersion curve, which was derived from the cold fluid equations, is shown in **Fig.3.5**. The maximum growth mode, which corresponds to the peak of the dispersion curve, can be extracted from the simulation by initializing the length in the simulation to be the wavelength that corresponds to the peak value

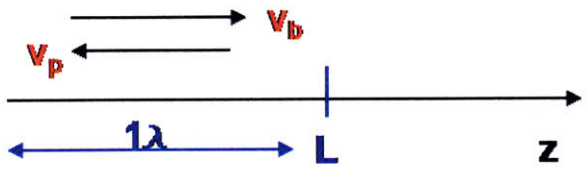

Fig.3. 4. Geometry for the cold, relativistic two-stream instability simulation.

of K. For this instability, the longitudinal electric field, E_z, is a convenient parameter choice for extracting the simulated growth rate. So by plotting the natural logarithm of the Fourier transform of E_z as a function of time, as shown in **Fig.3.6**, one will notice from equation (3.56) that the slope of this curve corresponds to twice the growth rate. As one can see from the figure, there is an initial period during which other modes are growing, but after a sufficiently long time (in this case ~ 200 plasma periods), the maximum growth mode begins to dominate and overtake the slower modes. The simulation growth rate appears to be in reasonably good agreement with analytical theory, yielding a percent difference of less than 3%.

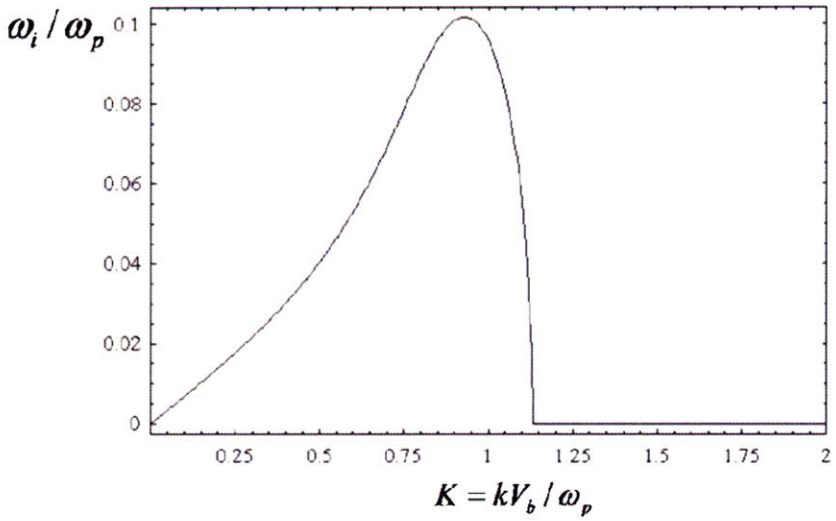

Fig.3. 5. Analytical dispersion relation for the cold, relativistic two-stream instability.

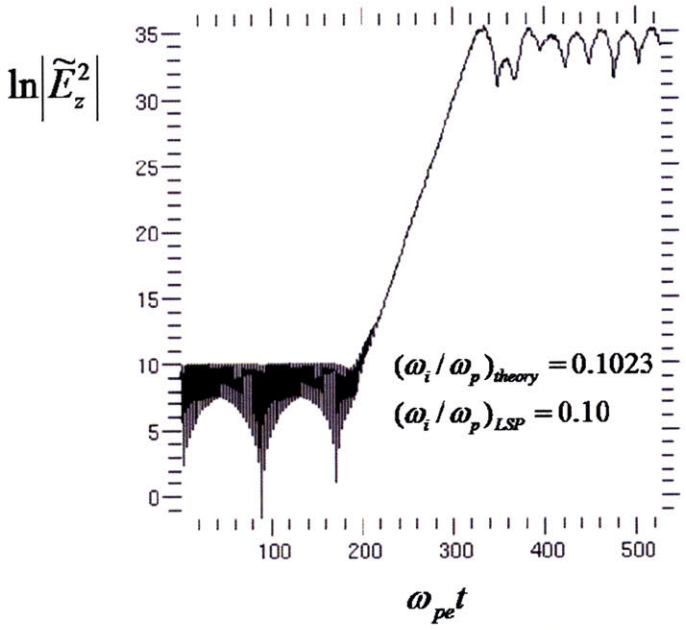

Fig.3.6. Simulated growth rate of the cold, relativistic two-stream instability.

Similarly, the cold, relativistic filamentary instability can be benchmarked in almost the same way with a slight change in the simulation's geometric orientation, shown in **Fig.3.7**. The analytical dispersion curve, which was also derived from the cold fluid equations, is shown in **Fig.3.8**. Because the maximum growth mode for this instability plateaus at K ~ 1, one can

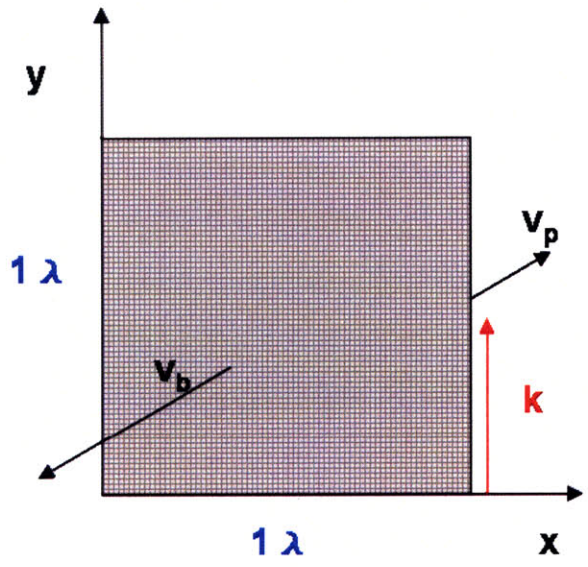

Fig.3.7. Geometry of the cold, relativistic filamentary instability.

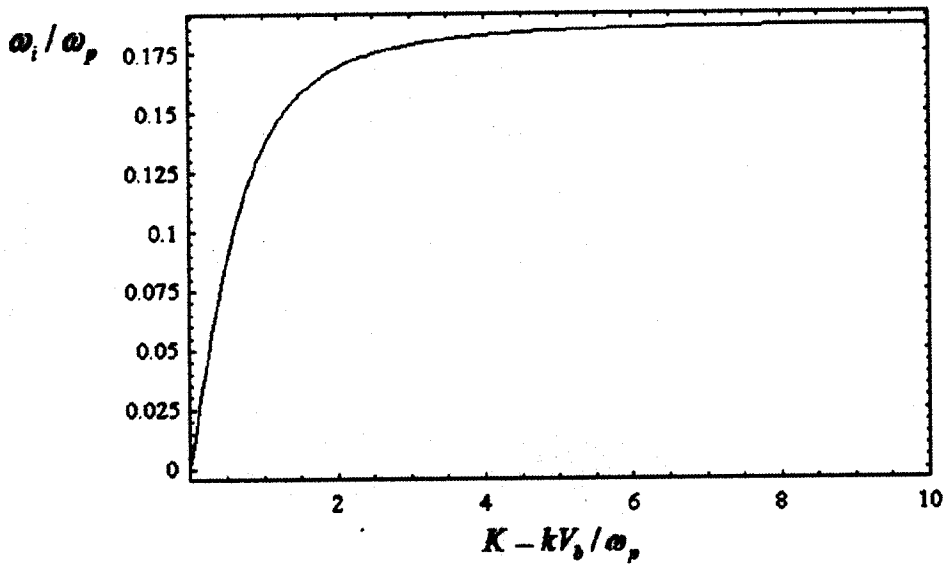

Fig.3.8. Analytical dispersion relation for the cold, relativistic filamentary instability.

choose roughly any high k mode and its corresponding wavelength to initialize the simulation. For this instability, the transverse magnetic field, B_x, is the convenient parameter choice for extracting the simulation growth rate. As previously mentioned, one can partially seed this mode in the LSP code by initializing the simulation with a small magnetic field perturbation, as shown in **Fig.3.9**. Like the two-stream, a similar log plot can be constructed and the growth rate extracted from the curve's slope, as shown in **Fig.3.10(a)**. An unseeded version (no initial magnetic field perturbation) of this simulation is also shown in **Fig.3.10(b)**. As one can see, mode seeding eliminates the initial "noisy" period that precedes the linear growth regime before it finds the maximum growth mode. In this case, the difference between the seeded and unseeded growth rates was virtually insignificant, with both in reasonably good agreement with analytical theory. However, the seeded growth rate will often prove to be in better agreement with analytic theory when one is interested in extracting modes other than the maximum growth mode. In these cases, the unseeded growth rate will tend to be higher than what is predicted by analytical theory since higher order modes tend to grow simultaneously.

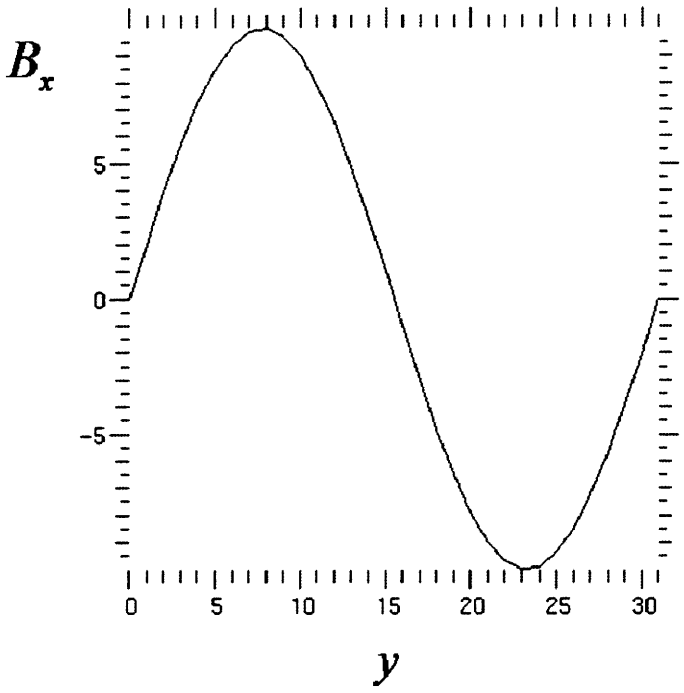

Fig.3.9. Magnetic field seed for the cold, relativistic filamentary instability.

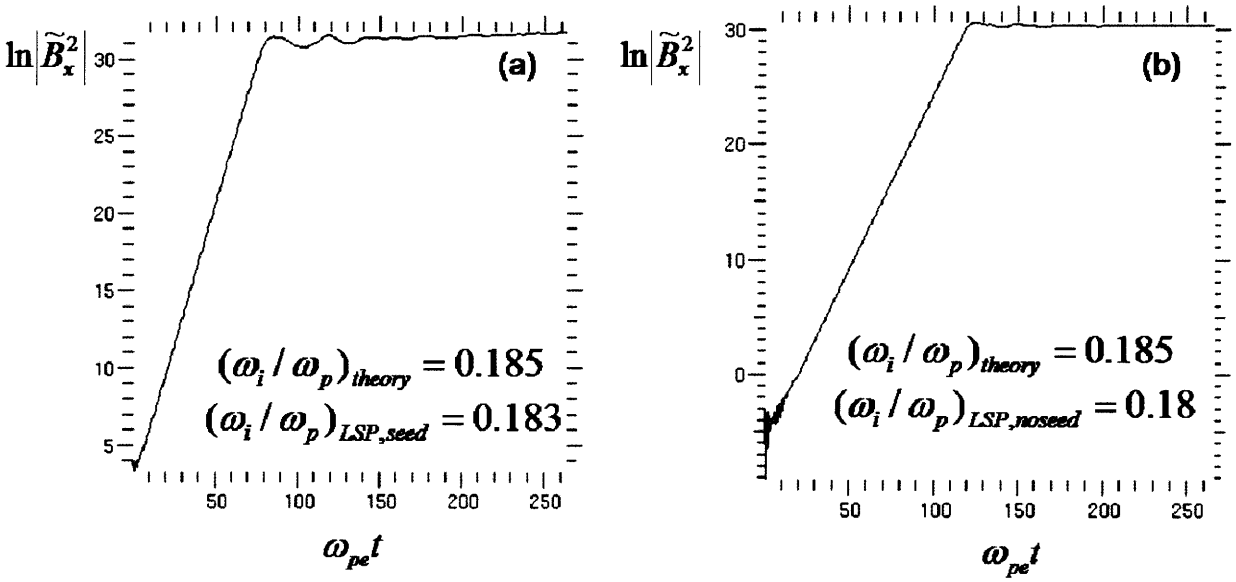

Fig.3. 10. Simulated growth rate of the cold, relativistic filamentary instability (a) with mode seeding (b) without mode seeding.

Chapter 4

Hot Electron Surface Confinement and the Escaping Electron Phenomenon

4.1 Introduction

The fast ignition concept relies on a relativistic electron beam generated via a short-pulse, high intensity laser-plasma interaction to ignite a pre-compressed deuterium-tritium target. More recent schemes have embedded a guiding cone into the initial target to keep a corridor open that is relatively free of coronal plasma during the fuel implosion and to also minimize the beam propagation distance to avoid subsequent transport issues. Furthermore, this embedded cone has also been shown in some cases to aid in the refocusing of the laser light, as well as confine and guide a beam of electrons along its inner wall. However, the degree of this electron confinement and guiding has been a subject of debate in recent years as a result of a number of inconsistencies that have arisen in experimental and analytical results. Namely, early

analytical work suggested that a minimum ("critical") cone angle existed below which nearly all of the absorbed laser energy would be carried along the surface by hot electrons confined by self-consistent electromagnetic fields [47]. Later experimental results confirmed the enhancement of hot electron confinement to the cone surface for smaller cone angles, but failed to reproduce this so-called critical angle below which complete confinement existed [48].

We have performed both integrated-explicit and hybrid-implicit PIC simulations with the XX [49] and LSP [36] codes, respectively, of cone and slab geometries with laser parameters similar to early published results. In addition to finding no evidence of a critical angle, we have also found that substantially fewer hot electrons (8-12%) are guided along the target wall than what has been previously reported (50-100%), suggesting that this surface confinement is only a minor effect. In doing so, we were also able to draw a parallel between this discrepancy and the idea of "escaping electrons," which refers to significant differences that arise in the measured (escaping) hot electron spectrum with respect to the original birth spectrum due to the generation of strong electrostatic self-fields [50]. This work will examine how the measured electron spectrum relates to the originally hot electron birth spectrum for variations in target geometry, initial energy, and angular orientation.

4.2 Hot Electron Surface Confinement

The physical mechanism by which hot electrons are confined to the cone target surface can be explained by the formation of electromagnetic fields during the laser plasma interaction. Initially, electrons are generated during the laser plasma interaction due to collective absorption mechanisms such as $J \times B$ heating, vacuum heating, etc. As the electrons are accelerated into the bulk target in the direction of the incident laser, the hot electron jet results in the build-up of large magnetic fields on the cone surface, acting to reflect the remaining electrons that enter the target toward the vacuum region. In addition, a quasistatic electric field is also generated near the surface from the space charge that builds up as a result of electrons being pulled from the target by the laser electric field, acting to reflect electrons back into the bulk target. So, in sum, the counteracting nature of both the electric and magnetic fields results in a finite electron current flow along the cone surface which self-consistently enhances the initial fields.

4.3 Critical Angle Debate

This idea of a surface electron current has been explored in recent years, both analytically and experimentally, and it suffices to briefly review some relevant published results. Initial analytical work by Nakamura et al. involving obliquely incident laser pulses claimed the existence of a minimum cone angle which would allow for maximum energy transport along the cone surface [47]. Using a simple slab model (shown in **Fig. 4.1**) of an obliquely incident, linearly polarized laser pulse, they calculated the current density profile of relativistic electrons accelerated along the surface that are acted upon by a nonuniform magnetic field. As shown in **Fig. 4.1**, the solid density target is defined from $z \geq L$, where L is the depth of the surface current (approximated as $L \sim l_s \equiv$ electron skin depth), and inside the target, current neutrality is induced by a return current flowing in the opposite direction of the surface current. They assumed the electrons are bent by the magnetic field according to conservation of angular momentum in the x-direction and energy conservation, yielding momentum components

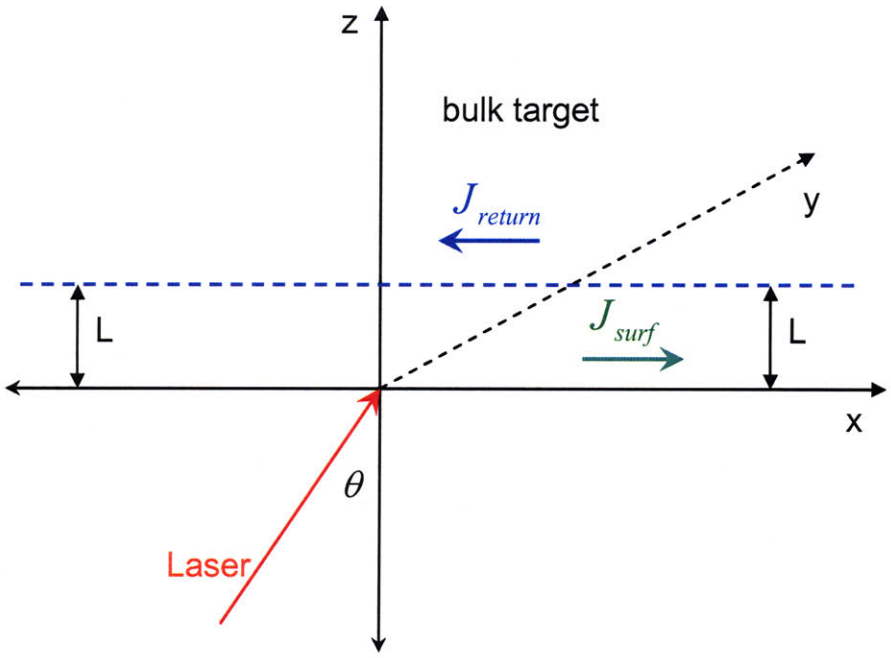

Fig. 4.1. Geometry for the Nakamura et al. analytical model of a linearly polarized laser incident on a solid slab [47].

$$p_x(z) = p_{in}\sin\theta + e[A(z) - A(0)] \tag{4.1}$$

$$p_z(z) = \pm\sqrt{p_{in}^2 - \{p_{in}\sin\theta + e[A(z) - A(0)]\}^2}\,, \tag{4.2}$$

where $B_y(z) = \partial A(z)/\partial z$, $p_{in} \le p_{max}$, and p_{max} is the maximum or cutoff value of a waterbag momentum distribution. Using this distribution model, they computed the surface current density as

$$\begin{aligned} J_s &= \frac{-en_s p_{max}}{m}\int_0^1 \frac{p_{in}\sin\theta + A)p_{in}^2\cos\theta}{\sqrt{1+p_{in}^2}\sqrt{p_{in}^2 - (p_{in}\sin\theta + A)^2}}\,dp_{in} \\ &\equiv -\frac{en_s p_{max}}{m\gamma_0}J_s'(z), \end{aligned} \tag{4.3}$$

where n_s is the number density of electrons of the surface current, $A = eA/p_{max}$, and $p_{in} = p_{in}/p_{max}$. By assuming conservation of canonical momentum, they also derived the return current density as

$$J_{ret}(z) = \frac{n_r e^2}{m}\left[A_m - A(z) + A_0\right], \tag{4.4}$$

where n_r is the number density of the background plasma and A_m is defined as $A(z = \infty)$. Finally, they used the self-consistency between the spatial profile of the surface magnetic field and the surface and return currents to derive the equation

$$\frac{\partial^2 A}{\partial z^2} = \begin{cases} J_s'(z) & 0 \le z < 1 \\ J_s'(z) - \dfrac{n_r}{n_s}\left(A_m - A + A_0\right) & L \le z \end{cases} \tag{4.5}$$

where $z = z/l_s$, $l_s = c/\omega_{ps}$, and $\omega_{ps}^2 = n_s e^2/m\gamma_0\varepsilon_0$. They solved this equation with the boundary conditions $A(0) = A'(0) = 0$, $A(\infty) = A_m$, and $A'(\infty) = 0$ using a shooting method to obtain the eigenvalue, A_m, after which they could obtain the surface and return current densities. However, the real quantity of interest was the transmittance, which they defined as

$$\xi = \frac{J_z(z = L)}{J_z(z = 0)}. \tag{4.6}$$

By calculating this ratio, they were able to locate a minimum, or "critical," angle at which the transmittance of electrons into the target drops to zero and all are reflected by the surface magnetic field. In sum, their self-consistent solution involving the magnetic vector potential and surface current allowed them to determine a "critical" angle below which no further electrons would penetrate into the bulk target and all would simply be confined to the target wall by the buildup of electromagnetic fields along the surface [47].

More recent experimental results by Li et al. involving oblique laser irradiation of planar foils using the Xtreme Light II laser system suggest that this surface confinement is less extreme [48]. Using a p-polarized pulse with an energy of up to 0.6 J in 30fs and a focal spot size of approximately 10μm, they measured angular distributions of fast electrons for different angles of laser incidence onto a 30μm aluminum target. Like Nakamura et al., their results show an increase in the number of electrons confined to the target surface as the laser incidence angle is reduced, with a maximum of around 50-65% for a 22.5° angle of incidence, but their results did not show a "critical" angle below which 100% of the hot electrons were completely confined.

4.4 Simulations of Hot Electron Confinement

In an effort to reproduce the experimental and analytical results of Li et al. and Nakamura et al., we utilized the hybrid-implicit PIC capabilities of the LSP code [36], as well as integrated explicit PIC simulations using a code developed by Andreas Kemp at LLNL [49]. By utilizing both codes we were able to take advantage of a number of features unique to each in order to better understand the hot electron transport and cone-target physics. More specifically, the fully integrated explicit PIC code developed by A. Kemp allowed for complete modeling of the laser-plasma interaction followed by subsequent hot electron transport down the cone. Although this technique is very robust, it is also computationally expensive, given that explicit schemes must resolve both the plasma frequency and Debye length. However, the LSP code nicely complements this technique with its direct-implicit particle push and hybrid fluid-kinetic algorithm that allows for modeling of colder, more dense plasmas for longer simulation times without having to resolve the plasma frequency and Debye length. Until recently, LSP did not have the correct boundary conditions to do fully integrated calculations that model the laser-plasma interaction and electron transport calculation, and as of late, this

new laser package has not been fully tested. Instead, users must simulate the generation of hot electrons by promoting from the background plasma with a specified conversion rate. However, the advantage to doing so is that the user has complete control over the initial hot electron distribution, which allows him/her to understand basic transport physics using simpler problems without having to deal with the complications of the laser pulse and laser plasma interaction.

4.4.1 Simulation Geometry

The simulation geometry, which is depicted in **Fig. 4.2**, was chosen to approximately mimic the analytical and experimental targets in the relevant publications claiming observance of surface electron currents mentioned previously. An aluminum slab 100μm long and 30μm thick was modeled in 2D Cartesian geometry to mimic the experimental geometry of Li et al [48]. Angles of 20 and 70 degrees were chosen to analyze the extent of increase in electron confinement as one moves to smaller target angles. In addition, the aluminum was initiated as pre-ionized Al3+ with an initial temperature of 5eV. As mentioned previously, LSP simulates laser conditions by promoting hot electrons from a cold fluid electron background. Electrons were excited with a Jöttner, or relativistic Maxwellian, momentum distribution, with temperature and drift parameters of 305 keV and 0.5c, respectively, which are approximately consistent with

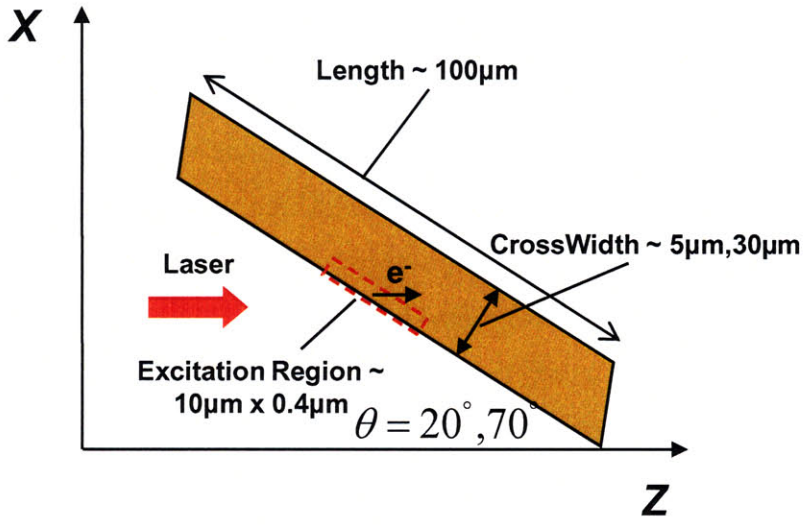

Fig. 4.2. LSP simulation geometry for modeling PIC and experimental laser-target problems of Li et al [48].

parameters fit from data obtained by Li et al [48]. In sum, a total of 0.30 Joules of energy were injected into the problem over a 30 fs Gaussian pulse in the form of hot electrons by promoting from a region along the upper cone, which was 10μm long and 0.4μm thick.

4.4.2 Electromagnetic Surface Fields

Before directly comparing confined electron fractions, it sufficed to first compare the magnitudes of the surface electric and magnetic fields with published PIC results by Li et al. The PIC code they used was similar in nature to that of A. Kemp's in that it used a fully-integrated explicit particle-push algorithm that included modeling of the laser-plasma interaction. From their simulations, they quote a peak surface magnetic field of approximately $2x10^7$ Gauss and a peak surface electric field of approximately $6x10^6$ kV/cm. Although these values are in reasonable agreement with A. Kemp's explicit code (B_{peak} = 1-$2x10^7$Gauss; E_{peak} = 3-$5x10^6$ kV/cm), they differ substantially from those of LSP. As one can see in **Fig. 4.3(a)**, the surface magnetic and electric fields peak at approximately $1.4x10^6$ Gauss and $1x10^6$ kV/cm, respectively, which are 6-15 times lower than the values quoted by Li et al.'s explicit PIC code [48]. In light of these discrepancies, one can conclude that the fields produced by the laser pulse make a significant contribution to the surface fields responsible for hot electron confinement. As

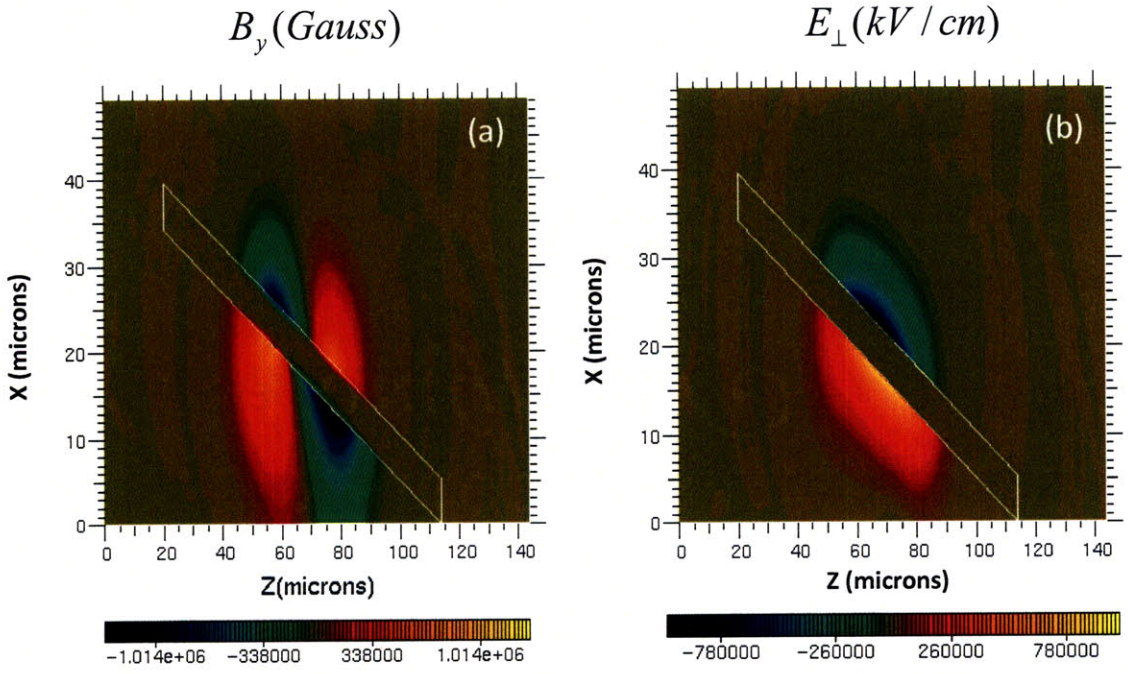

Fig. 4.3. Surface (a) magnetic and (b) electric fields produced from LSP simulation.

a result, codes such as LSP that do not contain a laser may be insufficient for accurately modeling this particular problem in its entirety.

4.4.3 Hot Electron Surface Fractions

Shown in **Table 4.1** is a compilation of surface and energy fractions computed for three different simulations that were run with variations in geometry and with collisions turned on/off. As one can see from the data, the 8-12% surface confinement for the aluminum slab case, which models the experimental conditions described by Li et al. [48], is substantially lower than the 50-65% confinement quoted in their PRL. Although the inclusion of collisions in the simulation did result in a slight enhancement in both electron confinement and energy carried along the surface, the increase was not enough to produce agreement with the fractions of Li et al. The reasoning for this enhancement is discussed in conjunction with the discussion of trajectories in the section that follows.

A similar simulation was performed by A. Kemp using a fully-integrated explicit PIC simulation modeling both the laser-plasma interaction and transport. Like the LSP simulation results, only a few percent of the hot electrons were found to be confined along the surface. Shown in **Fig. 4.4** are phase space plots of the hot electrons at two different times following the end of the pulse with a red line used to designate the direction along the slab surface. As one can see in **Fig. 4.4(a)**, there does not appear to be any preferred direction along the surface initially ($t \sim 144$fs). Later in time, the electromagnetic fields build up and act to redirect a small number

Simulation	Fraction of hot electrons traveling down the surface	Fraction of energy carried down the surface
Al slab (no collisions)	8.2%	5.5%
Al slab (collisions)	12.5%	9.1%
Al cone (no collisions)	6.9%	4.9%

Table 4.1. Fraction of hot electrons traveling along the surface and fraction of energy carried along the surface for three simulation cases using various geometries and with collisions turned on/off.

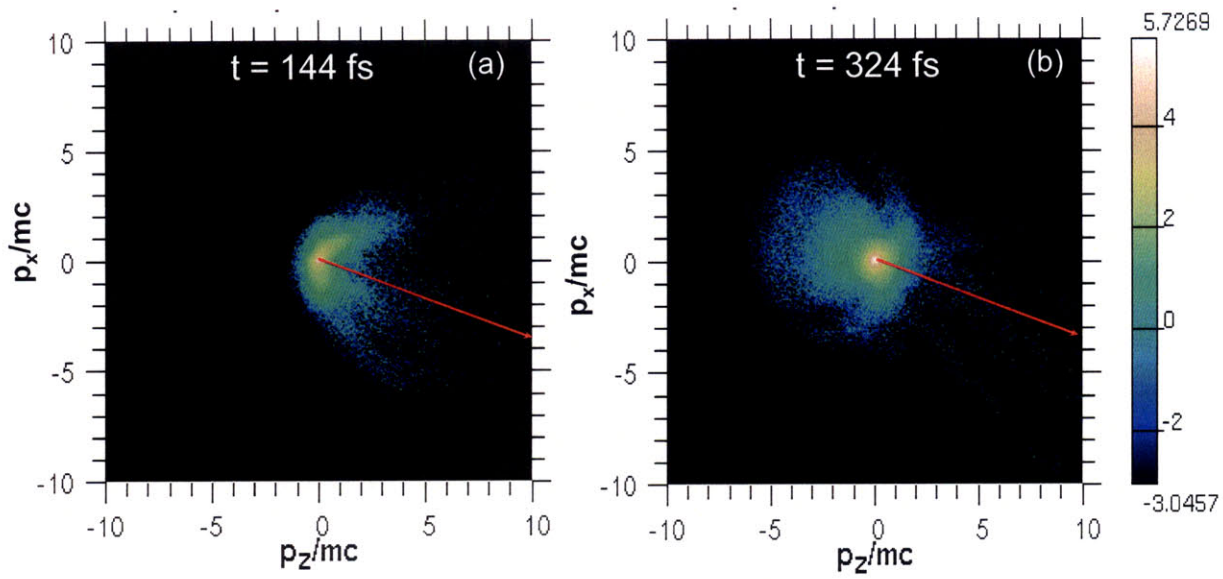

Fig. 4.4. Phase space plots of the hot electrons at t = 144fs (a) and t = 324fs (b) from a fully integrated PIC simulation by A. Kemp. Momenta are in units of $\gamma\beta$ and the red line refers to the direction of the surface.

along the surface, as shown in **Fig. 4.4(b)**, but the fraction is relatively insignificant, in agreement with the LSP results.

One final feature that was examined was the effect of geometry on surface confinement. More specifically, does a cone geometry, which is the target geometry currently being explored for fast ignition, result in more or less hot electrons being confined to the surface? As one can see in **Table 4.1**, both the surface confinement fraction and fraction of energy carried along the surface for the cone geometry are slightly reduced from that of the slab, but the two can be considered roughly comparable for the purposes of this study.

4.4.4 Trajectories of Confined Electrons

Although LSP does lack some of the relevant physics necessary for modeling the surface confinement problem in its entirety, one can still use its capabilities for understanding some of the basic physics surrounding the surface confinement process. Specifically, LSP allows the user to inject tracer particles into the simulation at user-specified spatial and temporal locations. These particles do not affect the simulation fields, but do "feel" the fields themselves. By

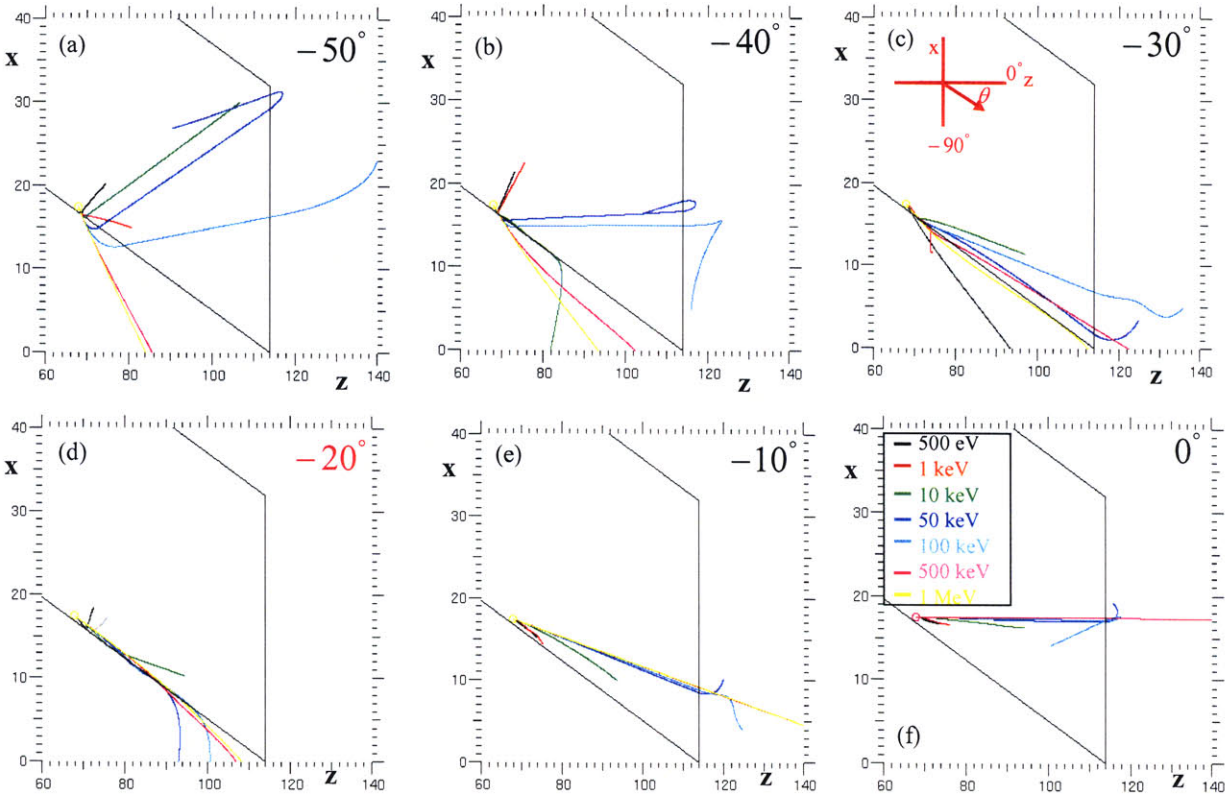

Fig. 4.5. Particle trajectories injected at various angles with a range of energies.

following the trajectories of these particles, one can gain a better understanding of what energy and angular orientation of the birth distribution will be subject to surface confinement. Shown in **Fig. 4.5** is a series of 6 frames consisting of 7 particle trajectories with various initial energies that have been injected at a given angular orientation relative to the z-direction. Highlighted in red is the -20° angle case, which refers to an injection angle directly along the target surface. The most significant result from these particle trajectory plots is that hot electrons born with an angular orientation directed down the target tend to stay confined to the target. Because the Jöttner birth distribution contains electrons emitted over 2π radians, a significant fraction of the hot electrons deemed "confined" will have originated from this direction to begin with. However, there does appear to be some electrons with a given range of energies and angular orientation that are pulled into the surface jet and subsequently confined. More specifically, there appears to be a "window of confinement" that exists such that hot electrons born with a moderate range of energies for a given angular orientation directed at or

below the angle of the cone will be confined by the surface fields. However, for hot electrons born with angular orientations directed inward towards the bulk plasma, there appears to be little chance for confinement. This phenomenon is also significant in understanding the enhancement in confinement that occurs when collisions are included, as mentioned in the previous section. Because scattering will have minimal effect on the higher energy electrons, these particles will continue to travel along an approximately linear path determined by the angle at which they are born. However, moderate to low energy particles that may have not been born with energies and angular orientations within this confinement window may be scattered into the window, resulting in an enhancement of confined electrons due to collisions.

4.5 The Escaping Electron Phenomenon

As a result of the discrepancies that arose between the measured hot electron surface fractions of Li et al. and those obtained by LSP and fully integrated PIC simulations, we were prompted to explore a recently publicized phenomenon known as "escaping electrons" to explain the differences in these results. The escaping electron phenomenon refers to analytical work published in recent years by E. Fill to compute fractions and energy spectra of electrons that escape into vacuum after being produced by ultra-short pulse laser-target interactions [50]. After the initial electrons from the beginning of the pulse escape into vacuum, the target charges up, resulting in very large electrostatic fields extending well into the vacuum region around the target. Consequently, the remaining electrons that are generated later in time either remain in the target as a result of insufficient energy to overcome these fields or escape from the target and are then slowed down by these fields. The primary implication of these effects is that the energy spectrum measured outside of the target after the pulse has ended is significantly altered from the birth spectrum, raising questions about earlier published results of hot electron temperatures, spectra, etc.

It should be noted that the results published by E. Fill are analytical and rely on a number of assumptions. More specifically, Fill assumes that the hot electrons are emitted instantaneously (i.e, the pulse is very short (of the order of 10fs or less)) and that magnetic effects can be neglected since electrostatic effects tend to dominate the self-field effects [50].

For the purposes of the simulations and experimental comparisons relevant to the work that follows, these are valid assumptions. However, it should be noted that a PIC simulation provides a more complete numerical analysis of this problem due to its complexity.

With these assumptions as a basis, E. Fill developed a simple Lagrangian technique using both planar and spherical geometry for computing the fraction and energy spectrum of escaping electrons using various initially assumed hot electron birth distributions [50]. Because the spherical geometry is more representative of the laser-target experiments that are typically performed, our comparisons will focus on these results. In sum, Fill concluded that the escaping spectrum is broader and slightly shifted to lower energies compared to the original birth spectrum. Furthermore, he found that for measurements taken at large enough distances from the target, the spectrum approaches an asymptotic form [50].

The results by E. Fill served as a foundation for explaining differences observed in the hot electron surface fractions quoted in experiments by Li et al. and our PIC simulations. Namely, the escaping hot electron spectrum measured at some distance from the target has been substantially altered by electrostatic self-fields emitting from the target and may only partially reflect the hot electron distribution within the target.

4.6 Hybrid Implicit PIC Simulations of Escaping Electrons

We began the initial investigation of escaping electrons with the LSP code using its built-in hybrid implicit algorithm mentioned previously. One of the primary issues to be addressed from these simulations was the effect of the angular orientation of the initial birth distribution on that of the measured escaping electron spectrum. In other words, does an added drift to the initial distribution in either direction of the target affect what is measured along the surface or elsewhere? Because LSP allows the user complete control over the initial birth distribution and removes the complicated and, for this case, unnecessary physics associated with the laser, it serves as an ideal numerical tool for investigating this phenomenon. Another important issue was the effect of target size on the escape spectrum. Because the hybrid implicit algorithm utilized by LSP does not require the stringent temporal and spatial resolution

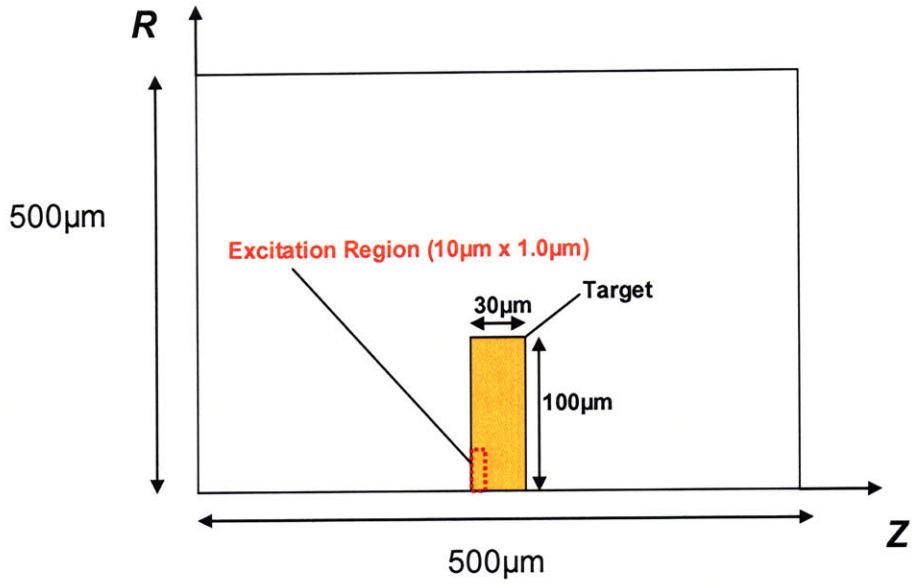

Fig. 4.6. LSP simulation geometry for modeling escaping electrons.

as in conventional explicit PIC codes, this also made the code advantageous for modeling larger targets.

The targets that were modeled in these simulations were representative of the experimental targets of Li et al. modeled previously and shown in **Fig. 4.2**. However, because the field structure is so critical to the escaping electron phenomenon and given that the Cartesian geometry used in the previous simulations doesn't quite capture the correct radial fall-off of the fields, cylindrical *R-Z* geometry was used instead for these runs. Shown in **Fig. 4.6** is the target geometry consisting of a 100μm x 30μm pre-ionized aluminum slab bounded by vacuum in a 500μm x 500μm volume. Hot electrons were promoted over a Gaussian temporal pulse of 30fs with a total energy of 0.30 J, which corresponds to approximately 50% of the total energy of the laser pulse quoted by Li et al [48]. The hot electrons were promoted from the background with an initial distribution characterized by a Jüttner or relativistic Maxwellian, which will be discussed in more detail in Chapter 5. Given the importance of the issue of angular orientation of the birth distribution, three cases were simulated: a distribution with a temperature of 305 keV and no drift (case A), a distribution with a temperature of 305 keV and a drift of 0.5c directed in the z-direction (case B), and a distribution with a temperature of 305 keV and a drift of 0.5c directed in the (radial) r-direction (case C).

4.6.1 Evolution of Hot Electrons

Shown in **Fig. 4.7** is the time evolution of hot electrons in terms of number density spanning from the end of the pulse at 30fs to approximately 500fs. As one can see from the figure, the hot electrons are initially emitted isotropically from the excitation region in a front or "shell-like" fashion. However, once the first wave of electrons leave the target, the target then acquires a positive charge, resulting in the buildup of large electrostatic fields and a subsequent sheath around the target edges. This redistribution of charge over time can be seen in the plots of electrostatic potential shown in **Fig.4.8(a)-(f),** revealing an increasingly large potential drop that develops across the target. The consequences of these electrostatic fields can begin to be seen in **Fig.4.7(c)** as electrons from the excitation region reach the back edge of the target. At this point, the higher energy electrons with sufficient energy to overcome the sheath will escape

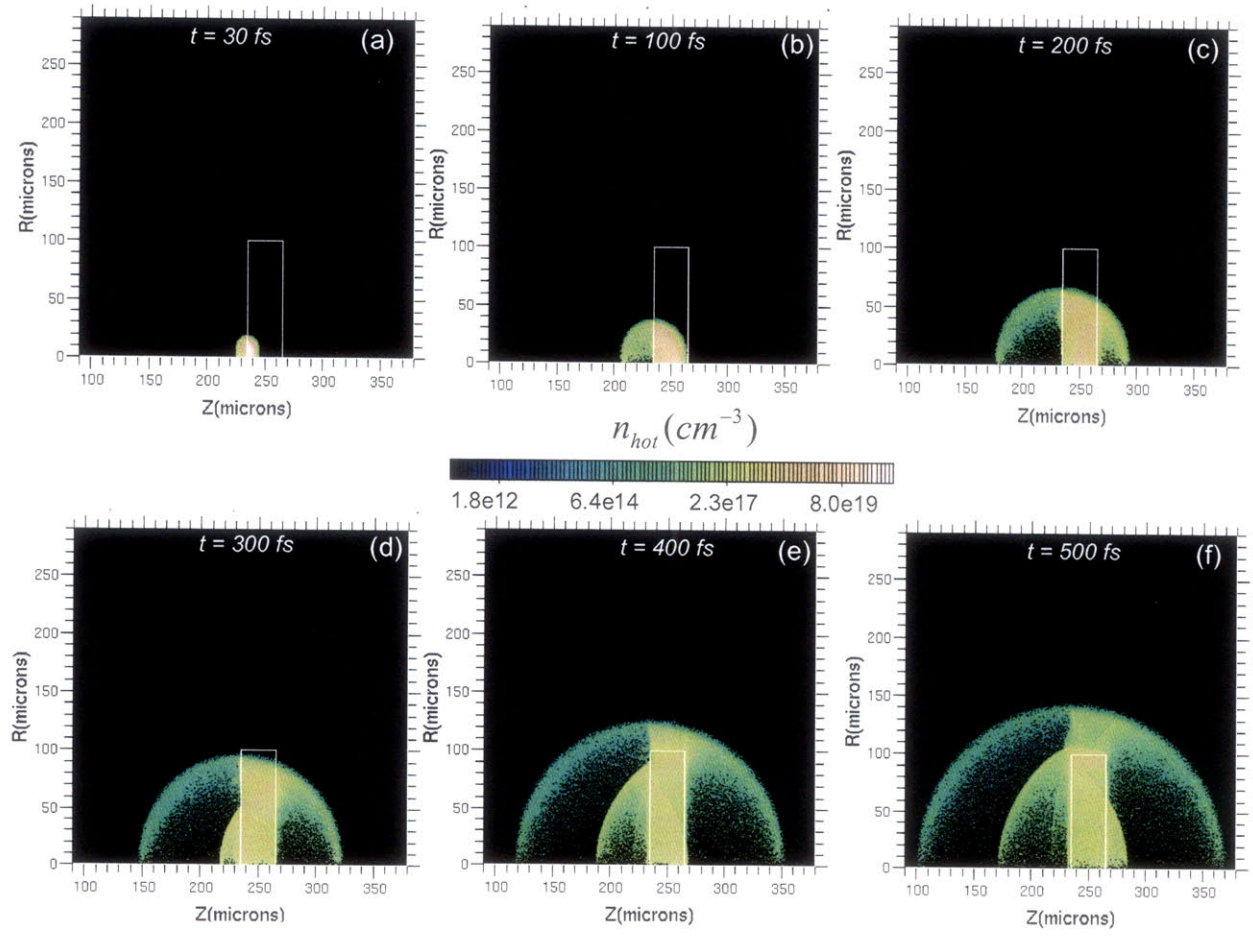

Fig. 4.7. Time evolution of hot electrons from the end of the pulse at 30fs (a) to 500 fs (f) plotted in term as number density (cm^{-3}).

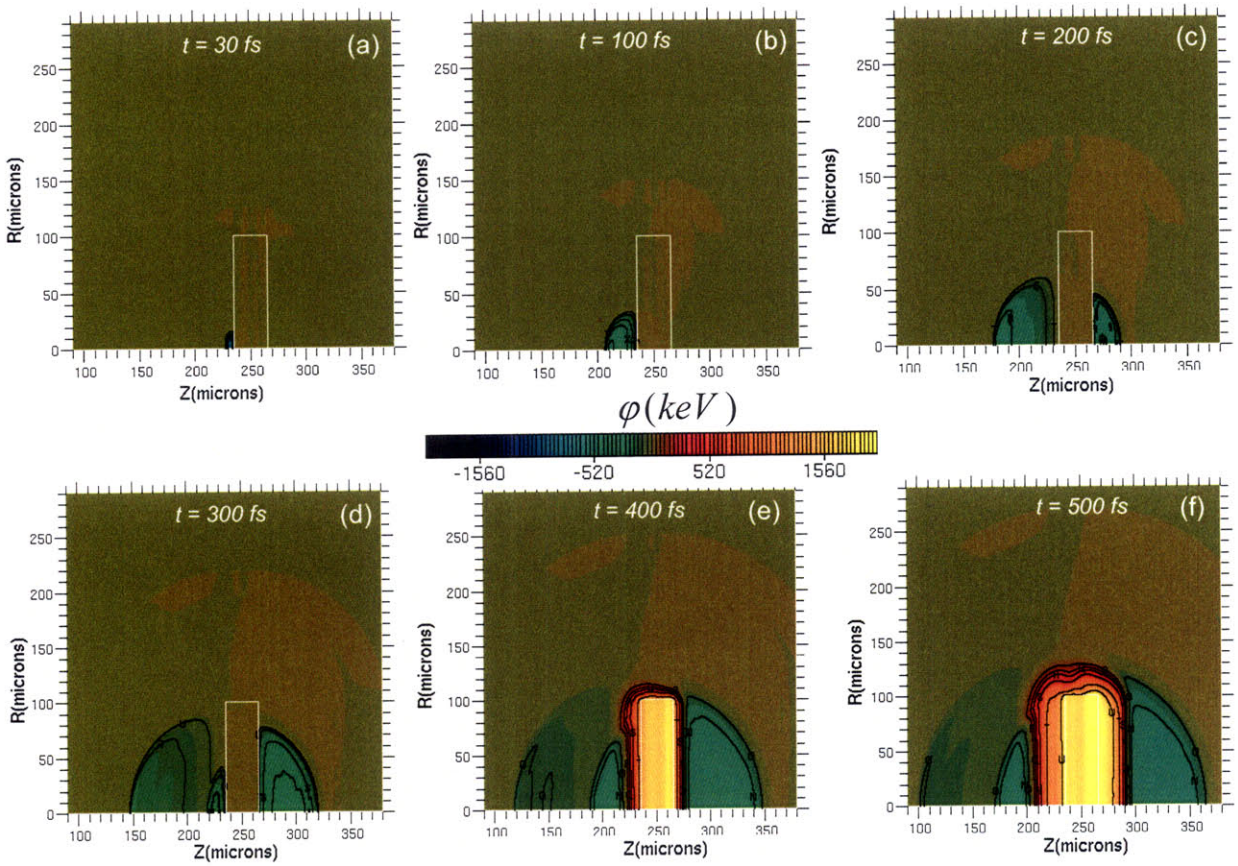

Fig. 4.8. Time evolution of the electrostatic potential in keV from the end of the pulse at 30fs (a) to 500fs (f).

from the target while the lower energy electrons will simply reflux, or bounce, back towards the front edge with a redirected transverse momentum. This process continues as the electron bunch(es) within the target bounce back and forth against the sheath along the target edges, with some fraction of electrons escaping with each bounce. Traces of the escaping electrons after each reflux event can be seen in **Fig.4.7(c)-(f)** in the form of "density shells" at the front and the back of the target that lie within the larger "initial escape" shell. Eventually, those electrons that continue to reflux within the target reach the top edge, at which point they then have a higher probability of escaping due to the lower potential drop at the top of the target compared to the potential drop across the sides, as shown in **Fig.4.8**. As one can see from the figure, the potential drop across the target gradually builds up as electrons continue to escape with each

reflux event. For later times, this potential drop becomes so large that no more electrons within the target have sufficient energy to escape, at which point there exists two hot electron populations: a confined population bound within the target by the electrostatic fields and an escaping population that has left the target but still feels the effect of the surrounding fields.

4.6.2 Characterization of Escaping Electrons

For many experimental measurements, the escaping electrons are those electrons whose features are quoted to characterize the initial hot electron birth population within the target. Because the electrostatic fields that develop around the target have such a dramatic effect on the electrons that escape, the two populations must be considered separate with their own distinct features. However, the ultimate goal of this work is to understand how the features of the initial birth population of hot electrons are altered compared to the escaping population. The hope is that a technique can be developed for experiments to predict initial birth population features by simply using escape measurements.

In order to begin the analysis of the escaping population features, a reliable method needed to be developed to distinguish escaping electrons from trapped electrons. The simplest technique one might consider is use of the directionality of the velocity vector of electrons, categorizing only those electrons directed away from the target as having escaped. However, this technique has the disadvantage that it does not account for those electrons who, at that point in time, are in the process of slowing down and will soon be trapped the next time the diagnostic is measured. In order to bypass this problem, we have developed a more sophisticated technique in which we take the dot product of a particle's velocity vector, $\vec{v}_p = (v_{rp}, v_{zp})$, with a unit vector directed radially from the target and intersecting the particle's position, i.e.,

$$\vec{U} = \frac{1}{\sqrt{(r_p - 0)^2 + (z_p - z_c)^2}} \left(r_p, z_p - z_c\right), \tag{4.7}$$

where $(0, z_c)$ is the target center and (r_p, z_p) is the particle position. This allows us to then compare the energy in the direction of the unit vector with the local electrostatic potential, after

Time (fs)	Escaping Electron Fraction
30	3.13%
100	2.36%
200	11.1%
300	18.3%
400	13.8%
500	6.63%

Table 4.2. Fractions of escaping electrons computed at various times from the end of the pulse at 30fs (a) to 500fs (f).

which we are then able to determine if the particle has sufficient energy to escape. Shown in **Table 4.2** is a summary of the fraction of electrons that have escaped at various times throughout the simulation described previously. As one can see from the table, the escape fraction initially increases as more and more electrons reach the top edge of the target. However, once the potential builds up to a relatively high level, no more electrons can escape from the target. At this point, one might expect the escape fraction to simply level off, but a new phenomenon arises that causes this fraction to decrease. More specifically, consider two particles, one fast and one slow, at some time t in which both particles have been deemed "escaped." Later in time, the fast particle may overtake the slow particle, resulting in an increase in the potential drop seen by the slow particle. As a result, when the next diagnostic is taken, the fast particle is still deemed "escaped" but the slow particle has lost sufficient energy such that it no longer escaping. This effect can actually be rather large, resulting in the sudden drop in the escape fraction at later times.

The initial motivation for this work arose from discrepancies between experimental measurements of surface electron fractions and those obtained from PIC simulations. As a result, a significant feature of interest that may help to link these two sets of results is the measurement of escaping electron intensity as a function of angle. Shown in **Fig. 4.9** is a schematic of the simulation geometry and an angular coordinate system with the origin defined at the bottom center of the target and an angular spread ranging from 0°-180°. An angular sector, θ_{tsurf}, ranging from 81.5°-98.5° corresponds to the spread in angle at which those electrons

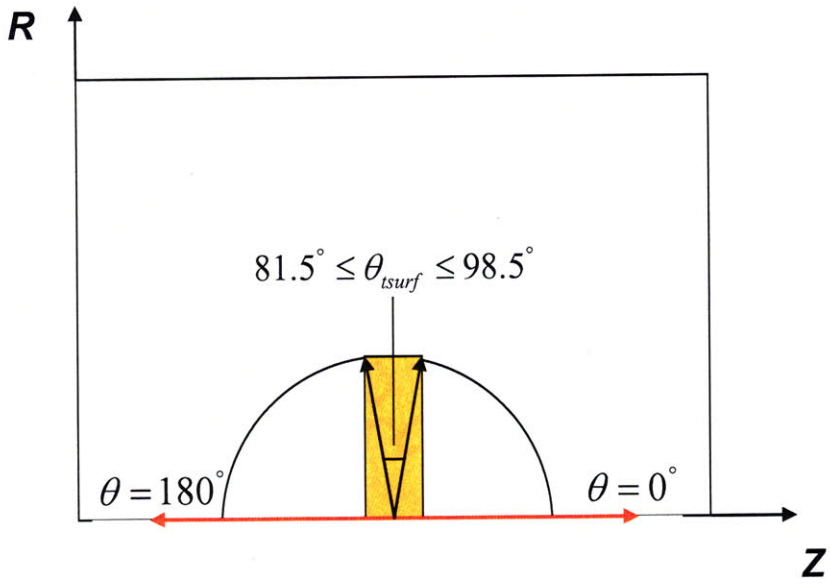

Fig. 4.9. Schematic of an angular coordinate system with the origin defined at the bottom center of the target ranging from 0°-180° and a surface escape angle, θ_{tsurf}.

escaping at the top of the target will exit through. By computing the fraction of electrons that escape through this angle, one can obtain a comparison with surface fractions quoted by Li et al [48].

Shown in **Fig.4.10** is a series of frames displaying histograms of the number of PIC particles that have been deemed "escaping" as a function of the angle of emission from the target. As one can see from the figure, there is a consistently dominant peak around θ = 90°, which corresponds to the top edge of the target. This is consistent with the previous plots of hot electron density and potential which revealed that the top edge possessed a lower potential drop relative to the other edges, creating a preferred direction of escape for electrons refluxing within the target. One can also see the development of two smaller, but still relatively large, surrounding peaks at t = 200-300 fs in **Fig.4.10(c,d)** at θ ~ 70°,145°. These two peaks correspond to the escape events described previously that take place as the electron bunches reflux within the target, resulting in the emission of electrons in shell-like structures. This subsequently creates an enhancement in escaping electron intensity around the angle at which a flux of electrons escape the target. Eventually these peaks diminish as the potential drop across the target increases and fewer electrons can escape. At this point, you start to see a clearly dominant peak near the edge of the target near θ = 90° where electrons have a higher probability

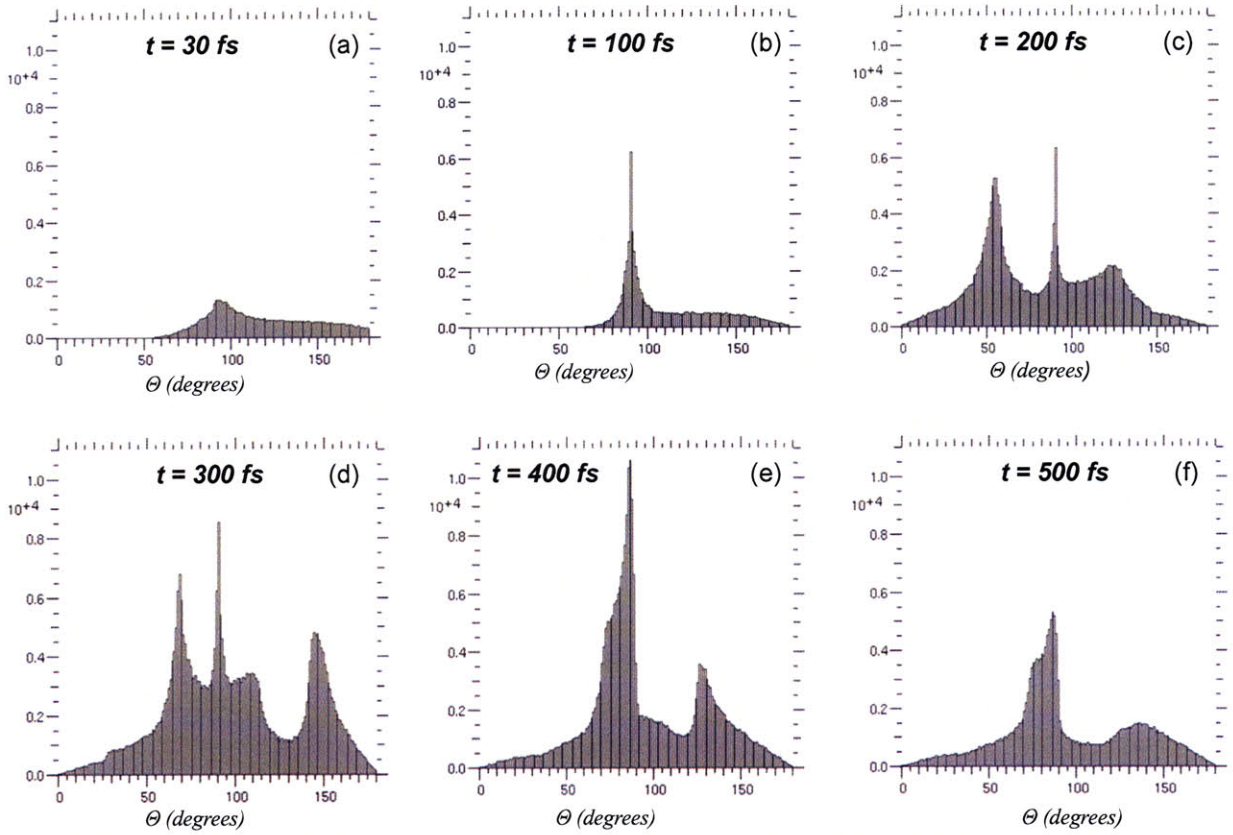

Fig. 4.10. Histograms of the escaping electron population as a function of angle from the end of the pulse at 30fs (a) to 500fs (f).

of escaping. After integrating between $81.5° \leq \theta_{tsurf} \leq 98.5°$, a maximum of approximately 31% of the electrons were observed to escape through the top edge of the target. This quantity can be used as useful comparison to the surface fractions quoted by Li et al [48]. At first glance, it is still rather low compared to the 50-65% fractions they quote. However, it should be noted that the birth distribution that was initiated in LSP was isotropic with no preferred direction, unlike what a laser would produce. In light of this, the low percentage is understandable. Li et al. quote surface fractions for a range of angles ranging from near glancing to near normal with surface. If one were to compare the 28% surface fraction from our isotropic simulation case with the 45°-near normal case measured by Li et al., which ranges from 6-28%, our results are in good agreement.

From the time history of the hot electron density and electrostatic potential shown in **Figs. 4.7-4.8**, it is evident that the escaping spectrum depends strongly on the shape of the target and the structure of the fields it produces, which will be discussed in more detail in a later

section. However, some similarities can still be found with the analytical work of E. Fill by comparing the energy spectrum of the initial birth population with that of the escaping population. Shown in **Fig. 4.11** are histograms of the energy spectrums of the initial birth population, shown in red, and the escaping population, shown in black. Over time, one can see that the escaping spectrum broadens and becomes down-shifted in energy, which is consistent with the analytical results of E. Fill [50]. Although it is difficult to see in this figure, the distribution also becomes harder with time. Furthermore, it is evident from **Figs.4.11(e)-(f)** that the escaping spectrum reaches an approximately asymptotic shape late in time, confirmed by the similarities in shape of the two escaping distributions at 500fs and 625fs.

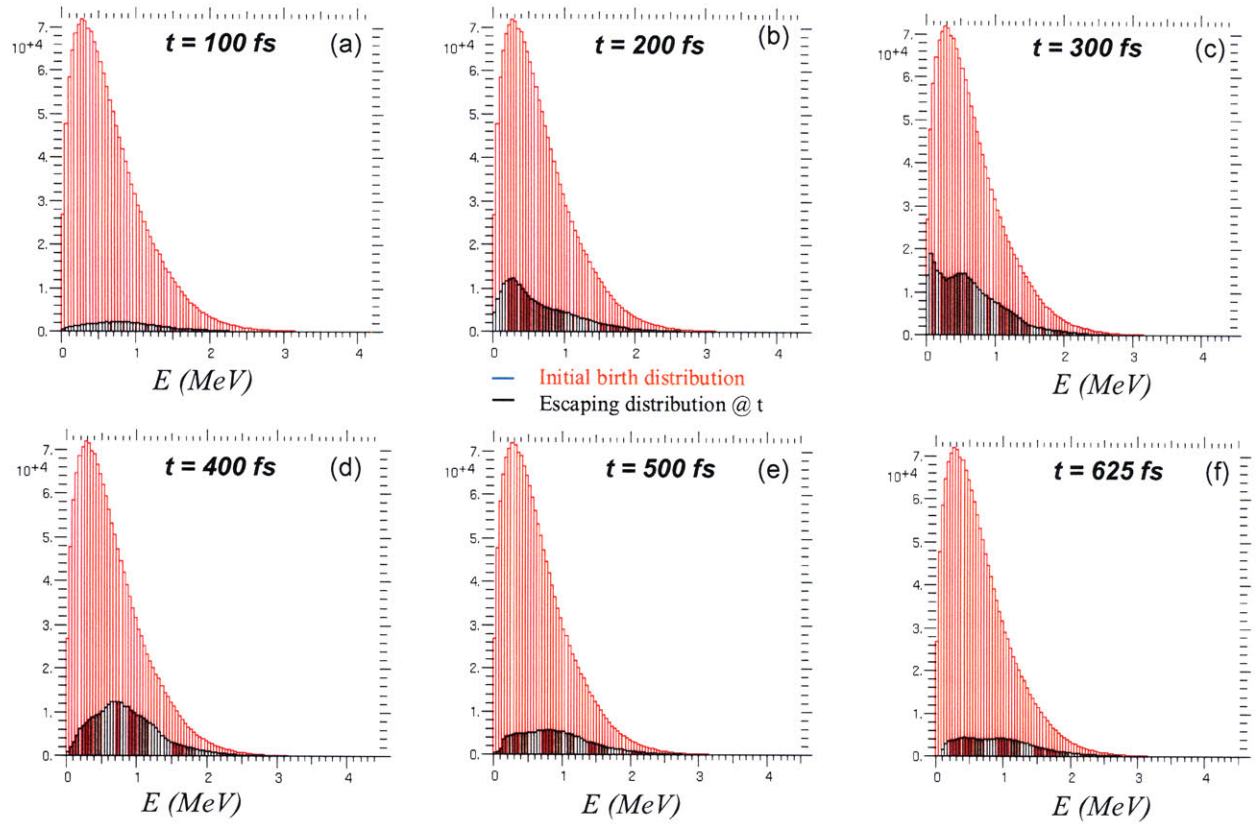

Fig. 4.11. Histograms of the energy spectrum of the initial birth population (red) and escaping electron population (black) from 100fs (a) to 625fs (f).

4.6.3 Effects of Angular Orientation of Initial Birth Distribution

Up to this point, the analysis has focused entirely on simulation case A, the isotropic hot electron birth distribution. However, in reality, the laser will be incident at some angle, which may influence the fraction of electrons leaving along the target surface, as quoted by Li et al. and other published works [47,48]. Because this laser angle of incidence naturally translates into a preferred drift direction of the hot electron birth distribution, we can implement this effect in LSP by simply adding a drift to the initially isotropic Juttner distribution.

As mentioned previously, LSP simulation cases B and C consisted of a Jöttner distribution with a 305keV temperature, but unlike case A, they have an added drift in the Z- and R-directions, respectively. More specifically, the distribution associated with case B is initiated with a drift of 0.5c directed normal to the target to approximate normal laser incidence and the distribution associated with case C is initiated with a drift of 0.5c directed parallel to the target to approximate glancing laser incidence. Shown in **Fig.4.12** are scatter phase space plots of the distributions for comparison of all three cases.

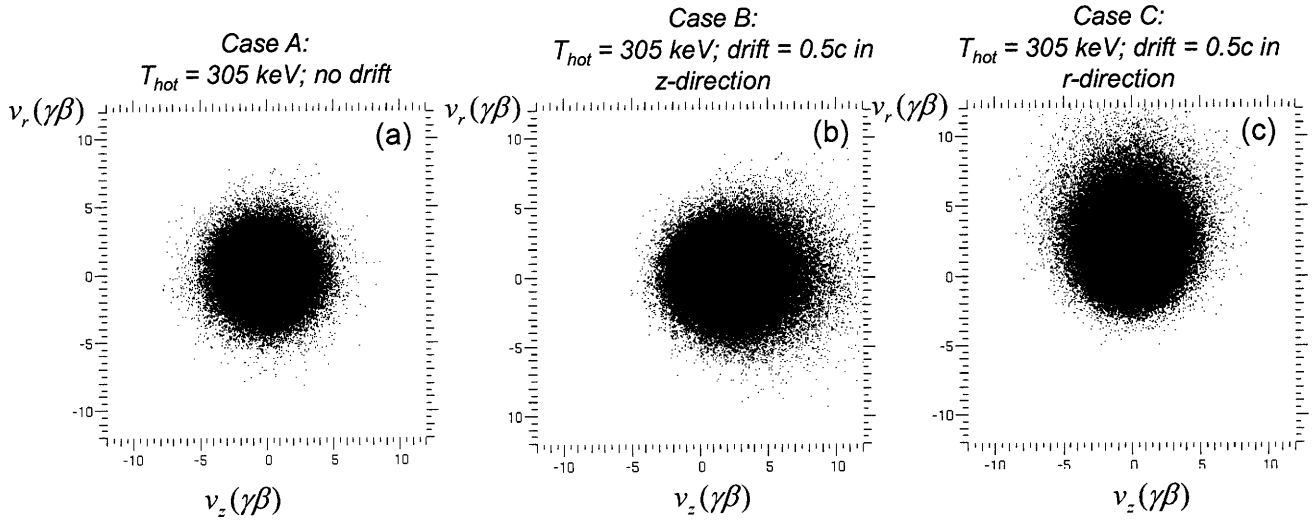

Fig. 4.12.Phase space scatter plots of the initial hot electron distributions for cases A, B, C.

The feature of greatest interest for comparison of the three cases is the escaping electron intensity as a function of angle with respect to the target center. Shown in **Figs. 4.13** and **4.14** are an equivalent series of histograms of the angular distribution of the escaping electron intensity, as was done for the isotropic distribution, case A, in **Fig.4.9**. As one can see from these figures, the structure is similar to that of the isotropic case, with a maximum of 3 and a

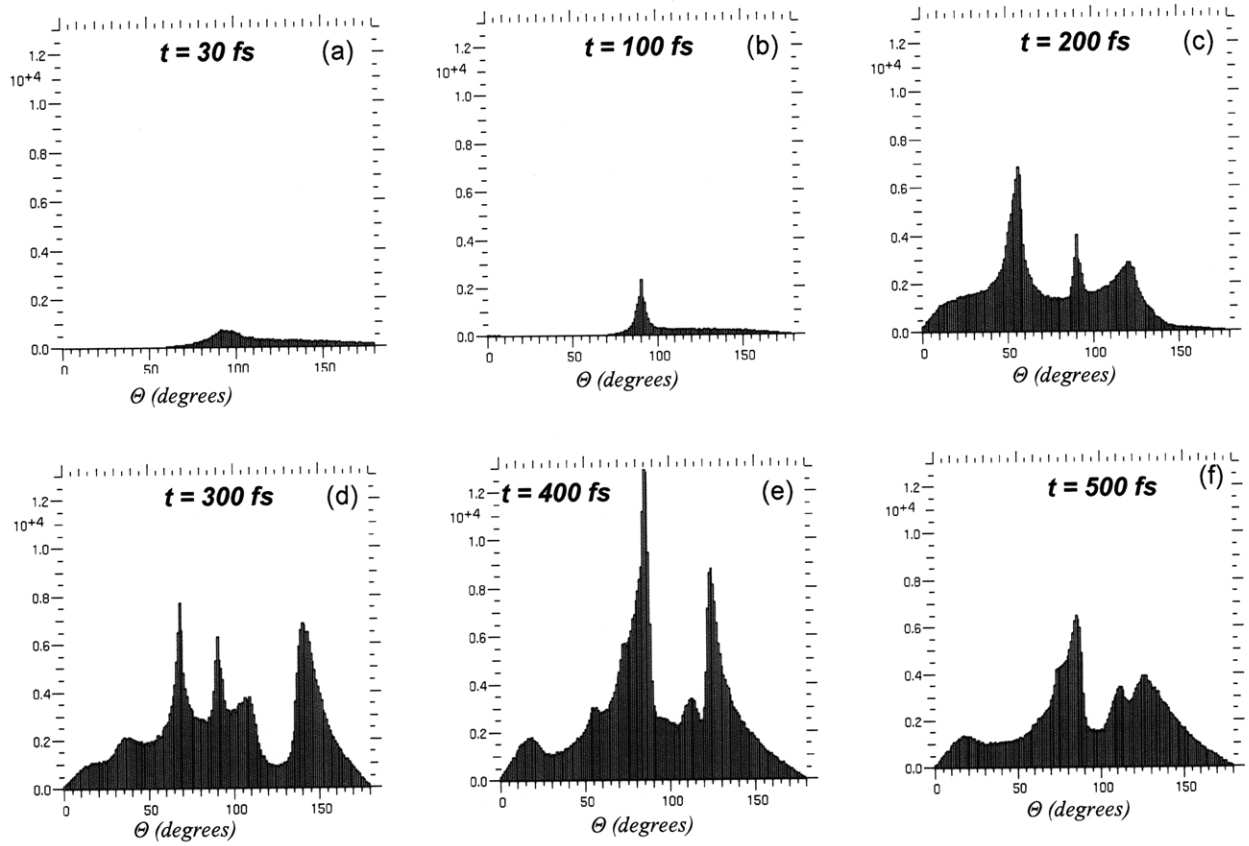

Fig. 4.13. Histograms of the escaping electron population as a function of angle for case B (v_{drift} = 0.5c in Z-direction; T = 305keV) from the end of the pulse at 30fs (a) to 500fs (f).

minimum of 1 peak at roughly the same angles of θ = 75°, 90°, 145°. For the normally incident drift case, B, the structure is a little more broad and full compared to the isotropic case, as one would expect, while the parallel drift case C, has a structure which is slightly sharper, especially around the peak at θ = 90°. Overall, though, the significant feature of interest is the clearly dominant peak at θ = 90° that exists for all three cases at later times. A more quantitative analysis of this feature can be gained from **Table 4.3** showing a comparison of the fraction of escape electrons being emitted within the surface escape angle, θ_{tsurf}, defined previously. The fraction has been computed at a later time of t = 625fs to more closely correspond to times when experimental measurements take place. As one can see from the table the fractions of electrons escaping through this angle are comparable (~25-30%), with differences being relatively minimal. What this suggests is that regardless of the initial angular orientation of the birth distribution, approximately the same fraction of electrons tend to escape along the top surface due to the lower potential drop.

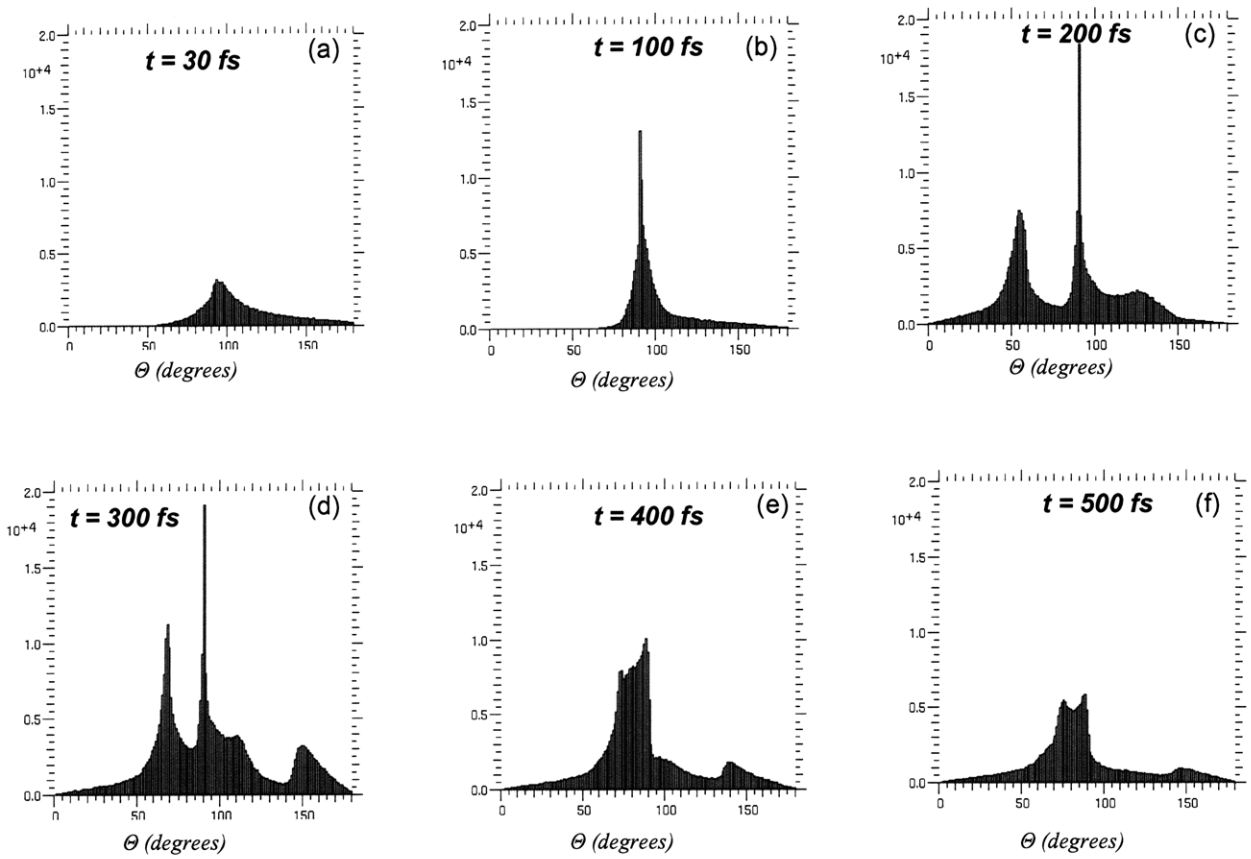

Fig. 4.14. Histograms of the escaping electron population as a function of angle for case C (v_{drift} = 0.5c in R-direction; T = 305keV) from the end of the pulse at 30fs (a) to 500fs (f).

Time (fs)	Escaping Electron Fraction within θ_{tsurf} Case A	Escaping Electron Fraction within θ_{tsurf} Case B	Escaping Electron Fraction within θ_{tsurf} Case C
625	31.0%	24.8%	29.3%

Table 4.3. Fractions of escaping electrons computed at 625fs for simulation cases A, B, and C.

4.6.4 Effects of Target Size on the Escaping Electron Population

Because the electrostatic fields surrounding the target have been shown to significantly alter the original electron birth distribution, one might expect that the target shape may also affect the distribution that experimentalists measure. A larger target will presumably result in a modified field structure as well as a different potential drop across the target, which will inevitably modify the ability of electrons to escape from the target. Because this effect will be significant to experimentalists due to the variety of target sizes they use for laser-target experiments that are conducted, we have investigated this issue by simulating several different targets of varying length.

Shown in **Fig. 4.15** is the original 30μm x 100μm pre-ionized aluminum target simulation geometry bounded by vacuum in a 500μm x 500μm volume, along with two additional longer targets of 200μm and 500μm, the latter being used to approximate an infinite conductor with a short at the boundary. An isotropic hot electron distribution was used for all three cases as discussed previously, consisting of hot electrons being promoted from the background over a 30fs Gaussian pulse with a total energy of 0.3J. The structure of the hot electron distribution involved use of an isotropic Jöttner with a 305 keV temperature.

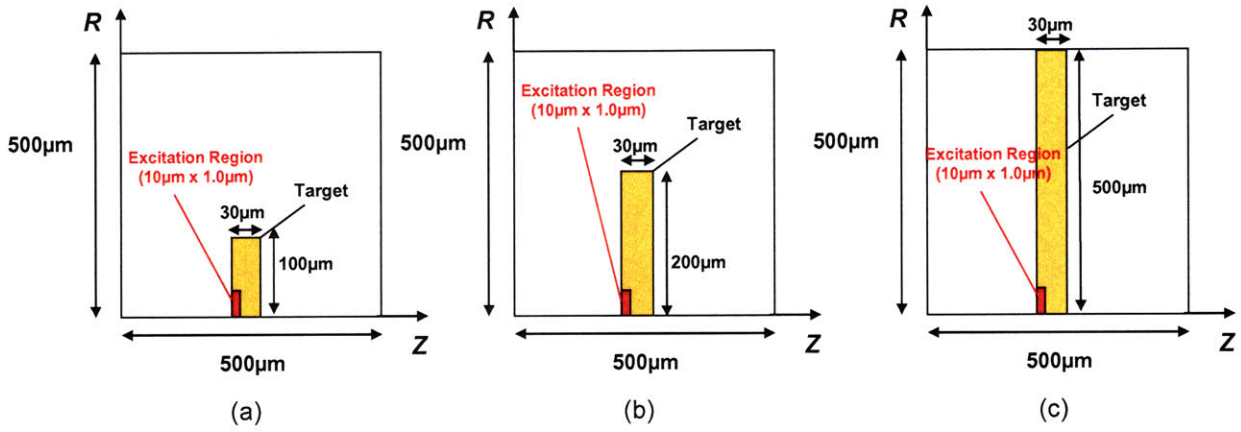

Fig. 4.15. Simulation geometry for 3 different target sizes consisting of 30μm X 100μm (a), 30μm x 200μm (b), and 30μm x 500μm.

Shown in **Fig. 4.16** is the hot electron density and electrostatic potential for each of the three target sizes at t = 800fs. What is immediately obvious from these plots is the increase in "escape shells" for larger and larger target sizes and the corresponding drop in potential. Basically, what happens is that for smaller target sizes, the hot electrons within the target reach the top edge and escape more quickly where the potential drop in this direction is lowest and creates a preferred path of least resistance. As a result, the target charges up and the potential plateaus not only more quickly but at a higher level to reach a quasi-static equilibrium in which no remaining electrons within the target have sufficient energy to escape. On the other hand, larger targets require more time for the hot electrons within the target to escape from the top edge, which allows for a lower potential drop that enables more electrons to escape from the target before the potential plateaus and prevents further escape.

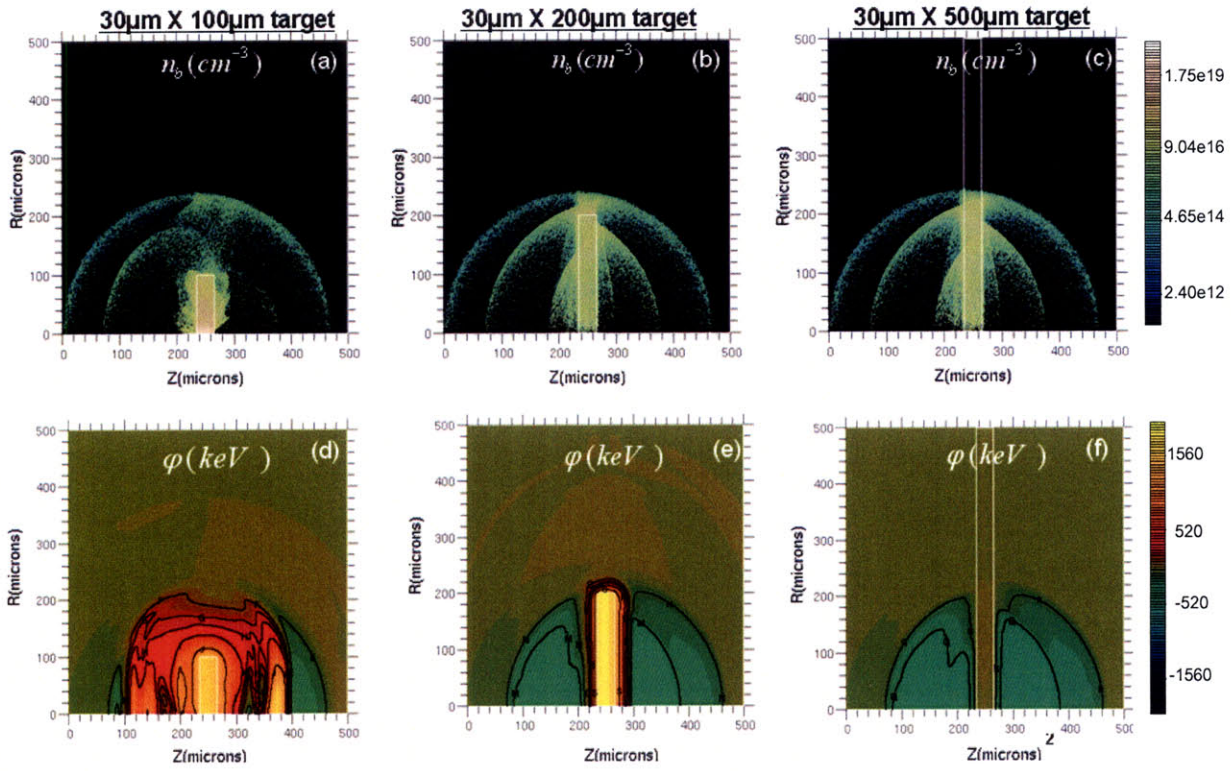

Fig. 4.16. Hot electron density for three different target sizes (a-c) and the corresponding electrostatic potential (d-f) at 800fs.

Target Size	Escape Fraction
30μm x 100μm	4.5%
30μm x 200μm	12.0%
30μm x 500μm	42.5%

Table 4.4. Escape fractions for the three target sizes computed at the approximate time at which the electrostatic potential plateaus.

One can gain a little more insight into the effects of target size by computing the escape fraction and the energy spectrum of the escaping particles for the three target sizes. Shown in **Table 4.4** are the escape fractions for the three target sizes at 700fs for the 30μm x 100 μm target, 900fs for the 30μm x 200 μm target, and 1 ps for the target approximating an infinite conductor (30μm x 500 μm). At these times, the potential is approximately constant and the escape fraction has leveled off. As one can see, the escape fraction increases with target size, reaching a limiting value of approximately 43% for the infinite conductor case. This is in agreement with the observations discussed previously since smaller targets allow electrons to escape from the top edge more quickly, resulting in a larger potential drop across the target and preventing further electron escape early on. The energy spectrums of the hot electrons also reveal significant target size effects. Shown in **Fig. 4.17(a-c)** are the energy spectrums of the initial birth distribution in red with the escape distribution overlaid in black for each of the three target sizes. A log plot of these distributions has been included in **Fig. 4.17(d-e)** for easier interpretation of these results. As one can see from the figure, the structures of the escape spectrums for the 30μm x 100 μm and 30μm x 200 μm targets are very similar, consisting of much broader and higher temperature escape distributions compared to the initial birth distribution around the peak. Furthermore, the escape distribution structure appears to be very similar to the initial birth distribution around the tail for both target sizes, suggesting that high energy particles escaping the target are not significantly altered by the fields surrounding the target. However, the energy spectrum of the escape distribution for the largest target (30μm x 500μm) appears to be relatively similar to the initial birth distribution. Based on the results in

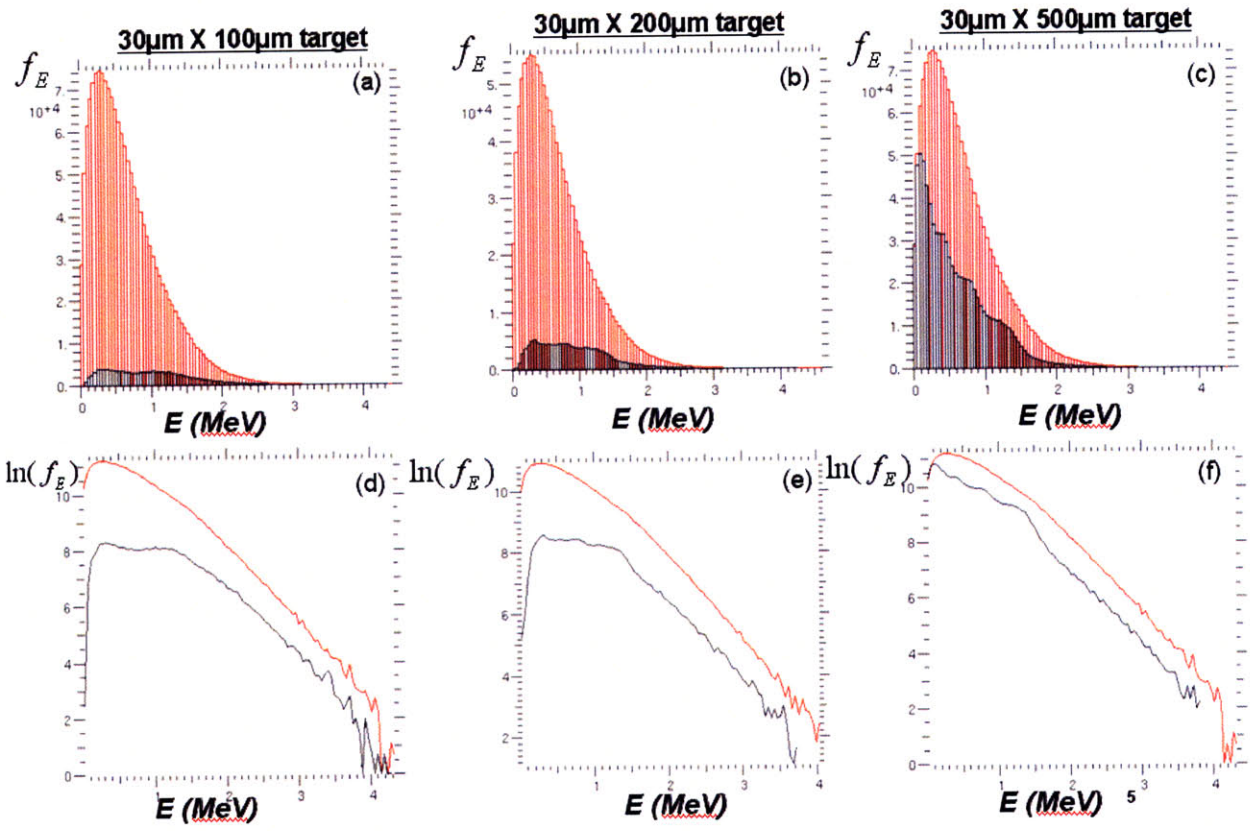

Fig.4.17. Energy spectrum of the initial birth distribution (red) and the escape distribution (black) for each of the three target sizes (a-c) and the corresponding log plot of each (d-f).

Fig. 4.16, one would expect this due the path of least resistance created by the short at the boundary and the absence of electron bursts escaping from the top edge in the previous cases. As a result, there are smaller fields and a lower potential drop across the larger target, resulting in less significant modifications of the initial birth distribution.

4.7 Conclusions

Our fully-integrated explicit and hybrid implicit PIC simulations have shown that hot electron surface confinement is only a minor effect. In addition to finding no critical angle, we have also found that even for small angles of incidence, the fraction of electrons confined to the surface is quite small (~8-12%), suggesting that the cone target angle can be considered a

minimal concern for design considerations. The discrepancy between these PIC results and the large surface fractions quoted from experimental measurements were clearly linked to the escaping electron phenomenon, which refers to significant differences in the measured (escaping) hot electron spectrum with respect to the original birth spectrum due to the generation of strong electrostatic self-fields. After re-computing the escape spectrum and the corresponding fraction that escaped from the target edge, our PIC results were found to be in approximate agreement with those quoted from experiment (30% vs. 28-50%). Furthermore, this fraction was found to be relatively independent of the angular orientation of the initial birth spectrum and subsequent angle of laser incidence. In sum, our results have shown that the electrostatic field structure produced by the target is strongly dependent on target geometry. As a result, the escaping distribution that is measured by experimentalists will be significantly altered from the initial birth distribution and will largely depend on the shape of the targets being used.

Chapter 5

Kinetic and Collisional Effects on the Linear Evolution of Fast Ignition Relevant Beam Instabilities

5.1 Overview of the Beam Instability Problem

The subject of beam-plasma instabilities has spanned many decades of research and has spawned a vast volume of literature due to its relevance to a wide range of fields of physics [51-57]. With the emergence of the fast ignition concept over a decade ago, this area of research has gained an increasing level of attention due to the relativistic electron beam associated with this scheme and the complex nature of the transport it must undergo [7]. More specifically, the fast ignition concept, an alternative to the conventional method of inertial confinement fusion, relies on a relativistic electron beam generated via a short-pulse, high intensity laser-plasma interaction to ignite a pre-compressed deuterium-tritium target. To

minimize the beam propagation distance and subsequent transport issues, more recent schemes have embedded a guiding cone into the initial target to keep a corridor open before the beam must traverse a density gradient of compressed plasma spanning several orders of magnitude [58,59]. Because this relativistic beam-plasma system is subject to a number of micro-instabilities that act to inhibit efficient energy transport and prevent the critical conditions for ignition to be met, an understanding of this transport system is crucial for evaluating the viability of the fast ignition scheme.

The relativistic beam-plasma system for fast ignition is a highly complex, transient, nonlinear problem with rapidly varying fields and currents that has proven difficult to model analytically in its entirety. Following the initial laser-plasma interaction and generation of relativistic electrons, a return current is drawn that establishes an approximately charge and current neutral equilibrium. During this equilibrium phase, the counter-streaming nature of this beam-plasma system makes it vulnerable to a number of micro-instabilities, namely, the two-stream[60], Weibel[51], and filamentary instabilities[56]. These instabilities will evolve through a linear growth phase, followed by a nonlinear saturated state. In sum, the combined effects of the shape of the initial equilibrium distribution, as well as collisions, on these phases has yet to be examined in great detail.

Knowledge of the detailed form of the initial relativistic electron beam distribution formed during the laser-plasma interaction is currently limited experimentally. Various experiments have characterized the beam distribution with temperature-like parameters which have been made use of by theorists and modelers by assuming a "Gaussian-like" shape [61]; however, as will be shown, the actual structure of the distribution can affect the instability growth rate. We will examine how the instability growth rates depend on various assumed initial equilibrium distributions, each with varying degrees of analytical difficulty: relativistic waterbag, the relativistic Maxwellian (Jüttner), and the low-temperature approximation to the relativistic Maxwellian (saddle-point approx.). However, a more physical depiction of the equilibrium beam distribution for analytical and computational models can be extracted from large-scale explicit particle-in-cell (PIC) simulations of the laser plasma interaction, as will also be presented in this paper.

The primary objective of this study will be to illustrate the effects of the initial beam distribution as well as collisions on the growth rate of critical beam instabilities relevant for fast

ignition using an analytical model supported by PIC simulations. Sec. 5.2 will outline the equilibrium formulation, collision model, and derivation of the dielectric tensor used to compute the various branches of instabilities of interest. Sec. 5.3 will follow with a brief overview of the theoretical distributions of interest and their respective features. For clarity, Sec. 5.4 will provide an overview of the LSP (Large-Scale-Plasma) code as well as simulation parameters used for comparison with analytical results. Sec. 5.5 will present numerical results of growth rates of the two-stream and filamentary instabilities for each of the theoretical distributions over a wide range of collision frequencies, which will be followed by similar calculations for a distribution extracted from a large scale explicit PIC simulation of the laser-plasma interaction in Sec. 5.6. Finally, a concluding discussion of the implications of these results will be presented in Sec. 5.7.

5.2 Equilibrium Formulation

5.2.1 Dielectric Tensor

The theoretical framework used to derive the dispersion equations consists of the familiar relativistic Vlasov-Maxwell formulation:

$$\frac{\partial f_s}{\partial t} + \vec{v} \cdot \frac{\partial f_s}{\partial \vec{r}} + q\left(\vec{E} + \frac{\vec{v}}{c} \times \vec{B} \right) \cdot \frac{\partial f_s}{\partial \vec{p}} = 0, \tag{5.1}$$

$$\nabla \times \vec{B} = \frac{4\pi \vec{J}}{c} + \frac{1}{c} \frac{\partial \vec{E}}{\partial t}, \tag{5.2}$$

$$\nabla \times \vec{E} = -\frac{1}{c} \frac{\partial \vec{B}}{\partial t}, \tag{5.3}$$

where s refers to the particle species. The equilibrium model assumes a spatially infinite and uniform beam-plasma system, no externally applied fields, immobile ions, and charge and current neutrality, i.e.,

$$n_b + n_p = n_i, \tag{5.4}$$

$$n_b v_b + n_p v_p = 0, \tag{5.5}$$

where b refers to the beam electrons and p refers to the background plasma electrons. For the purposes of linearization, scalar and vector quantities have been assumed to take the form

$$f_s(\vec{p},t) = f_s^0(\vec{p}) + \delta f_s(\vec{p},t) \tag{5.6}$$

$$S(\vec{r},t) = \delta S(\vec{r},t) \tag{5.7}$$

$$\vec{V}(\vec{r},t) = \delta \vec{V}(\vec{r},t) \tag{5.8}$$

where f_s, S, and $\vec{V}$ refer to species' distributions, scalar quantities, and vector quantities, respectively, f_s^0 is the equilibrium distribution, and the quantities preceded by δ's are the small amplitude perturbations and are assumed to have the form $e^{i(\vec{k}\cdot\vec{r}-\omega t)}$. After combining Maxwell's equations and applying a Fourier-Laplace transform, one obtains the following dispersion equation in terms of the electric field

$$\left[\frac{\omega^2}{c^2}\varepsilon(\vec{k},\omega) + k_j k_k - k^2 \delta_{jk}\right]\delta\tilde{E} = 0 \tag{5.9}$$

where δ_{jk} refers to the Kronecker Delta, $\delta\tilde{E}$ refers to the Fourier-Laplace transform of the electric field, and $\varepsilon(\omega,\vec{k})$ is the dielectric tensor

$$\varepsilon_{jk} = \delta_{jk} + \sum_s \frac{\omega_s^2}{\omega^2}\int d^3p \frac{p_j}{\gamma_s}\frac{\partial F_s}{\partial p_k} + \sum_s \frac{\omega_s^2}{\omega^2}\int d^3p \frac{p_j p_k}{\gamma_s}\frac{\vec{k}\cdot\frac{\partial F_s}{\partial \vec{p}}}{m_s\gamma_s\omega - \vec{k}\cdot\vec{p}}. \tag{5.10}$$

In this expression, F_s is defined as the normalized momentum distribution, f_s^0 / n_s and γ_s and $\vec{p}$ take the usual relativistic forms $\gamma = 1/\sqrt{1-\beta^2}$, $\vec{\beta} = \vec{v}/c$, and $\vec{p} = \gamma\vec{\beta}mc$. Finally, with the exclusion of all trivial solutions, one can obtain the following general expression for the dispersion relation

$$\det\left|\frac{\omega^2}{c^2}\varepsilon_{jk}+k_j k_k-k^2\delta_{jk}\right|=0\,. \tag{5.11}$$

5.2.2 Collision Operator

Although a sophisticated collisional study using a Boltzmann or Fokker-Planck operator is generally better, a much simpler model known as the BGK or Krook [62] operator can be used instead that will minimize algebraic complications. The Vlasov-Krook equation in its full form is then

$$\frac{\partial f_s}{\partial t}+\vec{v}\cdot\frac{\partial f_s}{\partial \vec{r}}+q\left(\vec{E}+\frac{\vec{v}}{c}\times\vec{B}\right)\cdot\frac{\partial f_s}{\partial \vec{p}}=-\nu\left(f_s-f_{s,\max}\right), \tag{5.12}$$

where ν refers to the collision frequency which acts to drive f_s toward a Maxwellian, $f_{s,\max}$. Although this operator is more tractable for mathematical analysis, it should be noted that it does not properly take into account the details of the collisions, nor does it retain the correlation of velocities before and after scatter [63].

Of the various types of collisions that may occur, background electron-ion collisions will be of greatest importance. The effect of these collisions will be to isotropize the motion of the electrons about the ions; therefore, for the Krook operator to produce physical results, the equilibrium electron distribution should be Maxwellian. We also expect the Maxwellian to have a finite drift. This drift arises as a result of the non-neutrality that exists where the hot electrons are produced, subsequently producing an electrostatic field that acts to restore charge and current neutrality by giving the background electrons a constant drift opposite that of the hot electrons. After these simplifications, the collision operator can be modified to $-\nu_{pi}\left(f_p-f_{p,\max}\right)$, where f_p is conventionally taken to be $f_p^0+\delta f_p$, the sum of the equilibrium and perturbed background electron distributions, respectively. This operator is also commonly expressed as $-\nu_{pi}\left(\delta f_p-\delta n_p f_p^0/n_p^0\right)$, where n_p is defined as $n_p^0+\delta n_p$, the sum of the equilibrium and perturbed background electron densities, respectively. Although it is common practice for some authors to neglect the second term involving n_p of this expression, allowing for only minimal corrections to the Vlasov-Maxwell formulation (i.e., ω can be replaced by

$\omega + i\nu_{pi}$), this approximation does not result in local particle conservation [63]. In fact, applying this technique to longitudinal plasma waves, such as in the two-stream instability, can result in spurious mode growth in the short wavelength limit.

The final collisional form of the dielectric tensor becomes

$$\varepsilon_{jk} = \delta_{jk} + \frac{\omega_p^2}{\omega^2}\int d^3p \frac{p_j(m_e\omega - \vec{k}\cdot\vec{p})}{(m\omega - \vec{k}\cdot\vec{p} + im\nu_{pi})}\frac{\partial F_p}{\partial p_k} + \frac{\omega_p^2}{\omega^2}\int d^3p \frac{p_j p_k \vec{k}\cdot\dfrac{\partial F_p}{\partial \vec{p}}}{m_e\omega - \vec{k}\cdot\vec{p} + im\nu_{pi}}$$

$$+ \frac{\dfrac{i\omega_p^2\nu_{pi}}{\omega^2}\left[\int d^3p \dfrac{(m\omega - \vec{k}\cdot\vec{p})\dfrac{\partial F_p}{\partial p_k}}{m\omega - \vec{k}\cdot\vec{p} + im\nu_{pi}} + \int d^3p \dfrac{p_k \vec{k}\cdot\dfrac{\partial F_p}{\partial \vec{p}}}{m\omega - \vec{k}\cdot\vec{p} + im\nu_{pi}}\right] * \left[\int d^3p \dfrac{mp_j F_p}{m\omega - \vec{k}\cdot\vec{p} + im\nu_{pi}}\right]}{1 - im\nu_{pi}\int d^3p \dfrac{F_p}{m\omega - \vec{k}\cdot\vec{p} + im\nu_{pi}}}$$

$$+ \frac{\omega_b^2}{\omega^2}\int d^3p \frac{p_j}{\gamma_b}\frac{\partial F_b}{\partial p_k} + \frac{\omega_b^2}{\omega^2}\int d^3p \frac{p_j p_k}{\gamma_b}\frac{\vec{k}\cdot\dfrac{\partial F_b}{\partial \vec{p}}}{m_e\gamma_b\omega - \vec{k}\cdot\vec{p}} \quad . \qquad (5.13)$$

It should be noted that this is not a completely general form of the collisional dielectric tensor, i.e., the background plasma electron distribution has been predetermined to be non-relativistic and collisions have been excluded from the beam terms.

5.2.3 Normalized Variable Convention

We define the following normalized variables that will be referred to in the calculations that follow:

$$\alpha = \frac{n_b}{n_p} \qquad T_{b,p}^* = \frac{T_{b,p}}{mc^2} \qquad \vec{u} = \frac{\vec{p}}{mc} \qquad (5.14)$$

$$\Omega = \frac{\omega}{\omega_p} \qquad K = \frac{kV_b}{\omega_p} \qquad \nu^* = \frac{\nu_{pi}}{\omega_p}$$

$$\vec{\beta}_{b,p} = \frac{\vec{v}_{b,p}}{c} \qquad \gamma_{b,p} = \frac{1}{\sqrt{1-\beta_{b,p}^2}}$$

The variables β_b and T_b^* refer to the relativistic drift and temperature of the beam species, which will be later defined in the numerical calculations as $\beta_b = 0.94\,(1\text{MeV})$ and $T_b^* = 0.01 \rightarrow 0.49\,(5 \rightarrow 250\text{ keV})$.

5.3 Theoretical Distributions

Although the specific form of the hot electron beam distribution is not well-known, various theoretical relativistic distributions are typically used with temperature parameters obtained from experimental scaling laws [61].

5.3.1 Jöttner Distribution

The fully covariant form of the relativistic Maxwellian distribution, also known as the Jöttner distribution, has the mathematical form

$$f_b^0 = \frac{n_b}{4\pi\gamma_b^2 T_b^* m^3 c^3 K_2(1/\gamma_b T_b^*)} e^{\frac{-1}{T_b^*}\left[\sqrt{1+u_\perp^2+u_z^2}-\beta_z u_z\right]} \tag{5.15}$$

where K_2 refers to the modified Bessel function of the second kind [64]. As one can see from the three-dimensional density contours plotted in **Fig. 5.1(c)**, this distribution is characterized by an ellipsoid with an asymmetric density localized at one end of its principal axis and exponentially decaying surface boundaries. In 1D, the reduced distribution obtained by integrating over the perpendicular and angular directions $(u_\perp, \varphi)$, similarly reveals the asymmetric, non-"Gaussian-like" peak and long tail, as shown in **Fig. 5.1(d)**.

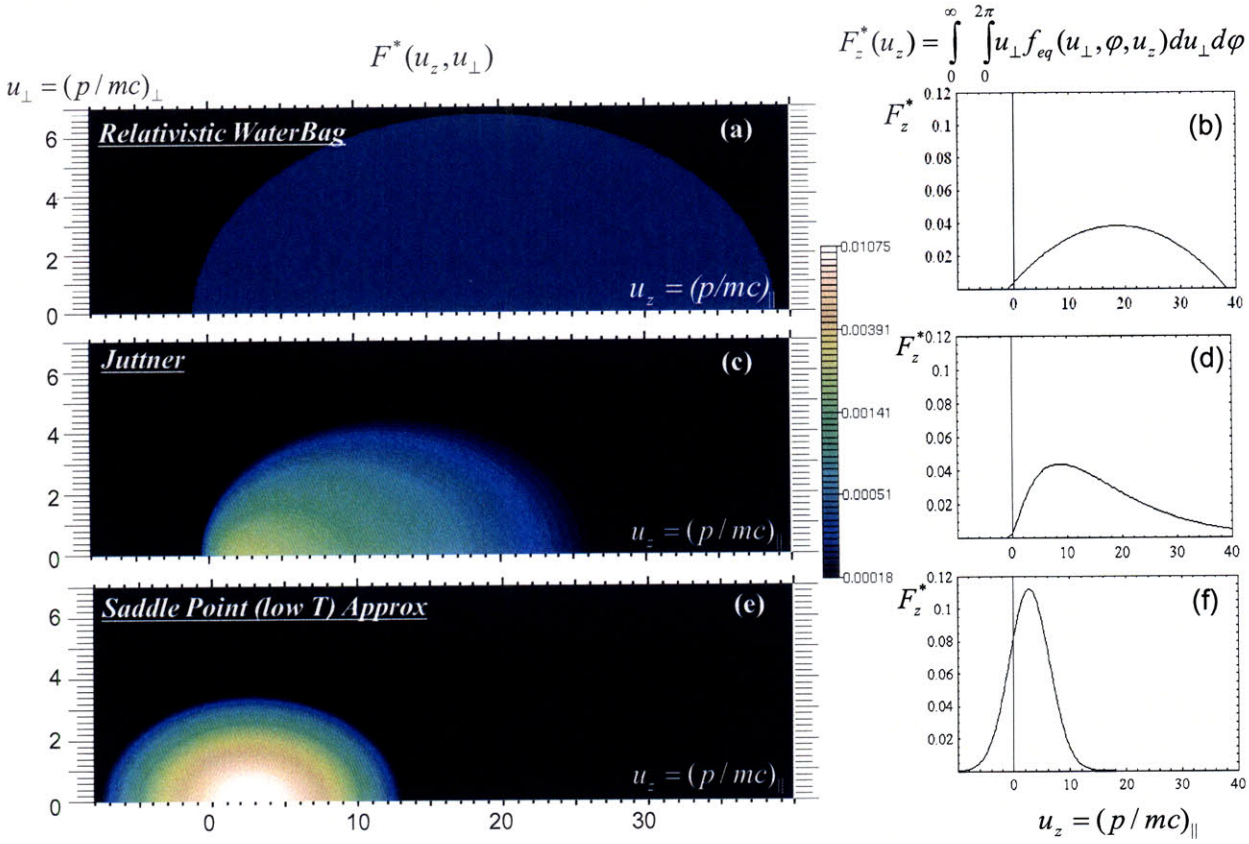

Fig. 5.1. Density contours , $F^*(u_z,u_\perp)$, and the reduced distribution, $F_z^*(u_z)$, integrated over $(u_\perp,\varphi)$ for the relativistic waterbag (a,b), the Jüttner (c,d), and the saddle point (low temperature) approximation to the Jüttner (e,f) for $\beta_b=0.94$ and $T_b=250keV$.

5.3.2 Saddle Point Approximation

Because the Jüttner tends to be rather complicated for computing the integrals involved in the dielectric tensor elements, a slightly simplified distribution can be obtained by doing a low temperature "saddle point" expansion of Eq.(5.15) assuming T << mc^2, or T* << 1, which yields the mathematical form

$$f_b^0=\frac{n_b}{\gamma_b m^3c^3\left(2\pi\gamma_b T_b^*\right)^{3/2}}e^{\frac{-1}{T_b^*}\left[\frac{u_\perp^2}{2\gamma_b}+\frac{(u_z-\gamma_b\beta_b)^2}{2\gamma_b^3}\right]}. \qquad (5.16)$$

This expansion is valid for all physical values of β_b so long as the temperature is sufficiently small. In contrast to the Jüttner distribution, the three-dimensional density contours, shown in **Fig. 5.1(e)**, reveal an ellipsoidal structure with symmetrically centered density and exponentially decaying surface boundaries. In 1D, the reduced distribution, shown in **Fig. 5.1(f)**, appears as a shifted Gaussian symmetric about its drift (with small leading order gamma corrections). Unlike the Jüttner distribution, Gaussian-like integrals are well-documented in the literature and prove to be significantly more tractable for computing dielectric tensor elements.

5.3.3 Relativistic WaterBag Distribution

An even simpler distribution than the saddle point approximation commonly used throughout the literature with variations in form is the relativistic waterbag, whose mathematical form has been defined as

$$f_b^0 = \frac{n_b}{(4/3)\pi\gamma_b m^3 c^3 (\gamma_b^2 \hat{\gamma}^2 - 1)^{3/2}} \Theta\left[\hat{\gamma} - \sqrt{1 + u_\perp^2 + u_z^2} + \beta_b u_z\right]. \qquad (5.17)$$

In this expression, $\hat{\gamma}$ is a "temperature-like" parameter that was derived by equating the second moment (temperature) of this distribution with the equivalent moment for the Jüttner, from which one can then solve for $\hat{\gamma}$ in terms of the beam temperature, yielding

$$\hat{\gamma} = \frac{1}{\gamma_b}\sqrt{5\gamma_b T_b^* \frac{K_3\left(1/\gamma_b T_b^*\right)}{K_2\left(1/\gamma_b T_b^*\right)} + 1}, \qquad (5.18)$$

where K_2 and K_3 are second order modified Bessel functions. In 3D, the density contours for the relativistic waterbag reveal a uniform density ellipsoid with well-defined surface boundaries, as shown in **Fig. 5.1(a)**. In 1D, the reduced distribution is characterized by an inverted parabola, as shown in **Fig. 5.1(b)**. One should note that the waterbag distribution is often more familiarly known as a square or "top-hat" distribution. However, the fully covariant form with the proper inclusion of relativistic effects gives it its ellipsoidal/parabolic structure. The "top-hat" features still do exist if one were to take a one-dimensional line-out of the 3D distribution, i.e., $f_b^0\left(u_\perp = 0, u_z\right)$.

5.4 Comparison with PIC Simulations

In order to validate the analytical dispersion relations that will be presented in the sections that follow, simulations were performed with the LSP code to extract linear growth rates for comparison with results. As explained in Chapter 3, LSP is a fully three-dimensional electromagnetic hybrid PIC code that was originally developed by Mission Research Corporation and in the last decade has been used extensively for modeling a wide range of relativistic electron transport problems relevant to fast ignition [36]. LSP contains many hybrid-implicit features that allow one to model larger, more dense plasmas for longer simulation times than conventional PIC codes. For the purposes of the beam-plasma problem in this study, we did not utilize many of the advanced features available, but instead ran the code as a conventional explicit PIC code. We did, however, make use of the code's ability to "turn on" and "turn off" its collision model.

For growth rate comparisons, LSP simulations were run in both 1D and 2D, depending on the instability of interest. Each simulation was set up to be one wavelength in the direction of the wave-vector and used simulation parameters of 100 particles per cell, 31 cells per wavelength, and 50 time-steps per plasma period. For the simulations in the collisional regime, 500 particles per cell were used for optimum energy conservation. In addition, each of the analytical distributions was loaded into the code using the method of univariate inversion, which has been outlined in detail in Appendix C. Although the original code does utilize Spitzer collision frequencies, constant frequencies were used for the purposes of exact comparison with analytical results. For simplicity, all instabilities were grown from noise (no initial velocity or density perturbations were applied). Growth rates were extracted from field quantities (i.e., the longitudinal electric field for the two-stream instability and the transverse magnetic fields for the Weibel and filamentary instabilities) by plotting $\ln\left|\widetilde{F}^2\right|$ vs. $\omega_p t$ and computing the slope, where $\widetilde{F}$ is the Fourier transform of the field quantity of interest (see Chapter 3 for details). Because these curves can sometimes be rather noisy, especially for 2D simulations, we extracted a maximum and minimum slope and used their average for simulation growth rate calculations. These maximum and minimum values are shown as error bar limits in the results that will follow.

5.5 Analytical Results

Because of the algebraic complexity of the theoretical distributions of interest, the analytical results that follow were computed numerically for a range of parameters. Parameters were chosen such that the effects of the initial beam distribution, collisionality, and beam temperature were clearly portrayed in regimes relevant to fast ignition. More specifically, dispersion curves of the maximum growth mode for each instability were computed for a low beam temperature ($T_b \sim 5$ keV) where the saddle-point approximation and Jüttner distributions are in agreement, and also for a relatively higher beam temperature ($T_b \sim 250$ keV) where the low temperature expansion for the saddle point approximation is no longer valid. Both temperature regimes also assume a relativistic drift of $\beta_b = 0.941$ (~ 1MeV) and a ratio of beam to plasma density, $\alpha = n_b/n_p = 0.1$.

Recent work by Bret et al. showed that the maximum growing mode is actually a coupled two-stream-filamentary mode that occurs for oblique orientations of the wave vector k, suggesting that a 2D instability calculation is necessary [56]. However, this work also concluded that as the beam reaches relativistic drifts, the filamentary mode begins to dominate the instability. Because the distribution of electrons for fast ignition relevant scenarios is expected to be largely relativistic in nature, the filamentary instability remains to be the primary concern. As a result, this study will focus independently on these instabilities using 1D calculations, the concentration being on the filamentary instability for fast ignition and the two-stream instability for academic purposes.

Although, in theory, one should be concerned with unstable modes from all three instabilities, the choice of parameters are not favorable for growth of the Weibel instability. Specifically, for all distributions, a single temperature is defined, T_b^*, that has not been decoupled into a perpendicular and parallel temperature. Because each of these distributions have moments such that $T_\perp / T_\parallel \leq 1$ for the parameter regime of interest (for example, the saddle point approximation yields $T_\perp / T_\parallel = 1/\gamma_b^2$), the Weibel instability growth rate is insignificant and will be omitted in the following sections. Finally, collision frequencies of $\nu_{pi}^* = \nu_{pi}/\omega_p \sim 0.01, 0.1$ were chosen to demonstrate the effect of collisions over a range that would be relevant to fast ignition.

5.5.1 Two-Stream Instability

Numerical calculations of the two-stream instability in the collisional and collisionless limits for the distributions of interest portray similar features. Mathematically, this branch of the dispersion equation for which $\vec{k} = (0,0,k_z)$ is

$$\omega^2 \varepsilon_{zz} = 0 . \tag{5.21}$$

As one can see in **Fig. 5.2,** numerical solutions of the dispersion relation for the low temperature regime (5 keV) reveal the classic "two-stream peak" around K~1. Scattering appears to have the usual damping effect in this long wavelength limit, with damping becoming more prominent with increasing collision frequency. In **Fig. 5.2(a)**, the saddle point result has been plotted simultaneously with the Jöttner result, while in **Fig. 5.2(b)** it has been plotted versus the relativistic waterbag result. As one can see, there is little difference in the dispersion curves of the three distributions in this low temperature regime. LSP simulations are also in reasonable agreement with analytical theory, yielding less than 25% error for each distribution, with larger errors attributed to the collisional cases where the code appears to generate growth slightly higher than the analytical results. As one would expect, an increase in beam temperature (250

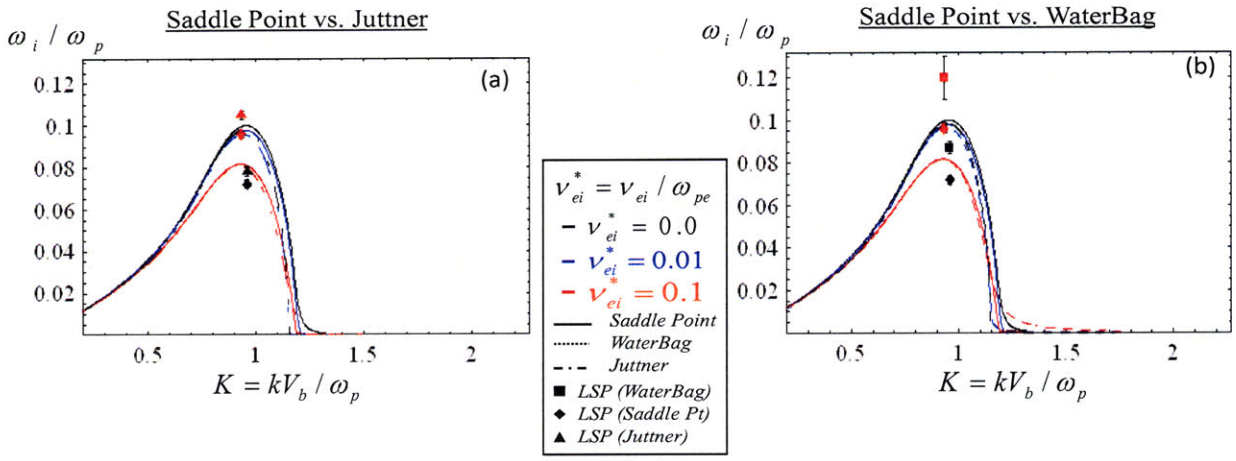

Fig. 5.2. Two-stream instability growth rate for the saddle point (solid), waterbag (dashed), and Jöttner (dot-dashed) for a range of collision frequencies in the low temperature regime (5keV).

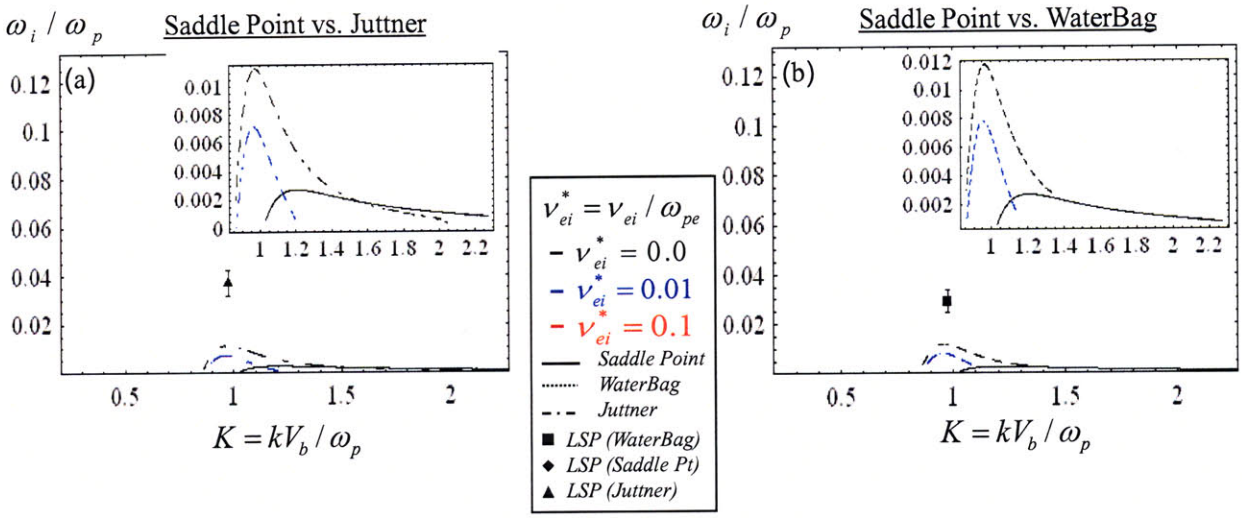

Fig. 5.3. Two-stream instability growth rate for the saddle point (solid), waterbag (dashed), and Jöttner (dot-dashed) for a range of collision frequencies in the high temperature regime (250keV).

keV) acts to suppress the instability for both distributions, as well. However, as shown in **Fig.5.3**, one begins to see the development of differences in the dispersion curves at higher temperatures. More specifically, in this regime, the saddle point expansion is no longer a valid approximation to the Jöttner distribution and underestimates the peak growth by approximately a factor of 4, as shown in **Fig. 5.3(a)**. Though the analytical form of the relativistic waterbag distribution that has been chosen does not rely on any low temperature approximations, it appears to show better agreement with the Jöttner distribution at high temperatures. LSP simulations in this high temperature regime show poorer agreement with the analytical results, though this is likely attributed to the low growth rates in this limit, which are difficult to extract from the high noise level in the simulation.

5.5.2 Filamentary Instability

Unlike the two-stream instability, the filamentary instability is dominant for more relativistic beams and so is more of a concern for fast ignition scenarios. Mathematically, this branch of the dispersion equation for which $\vec{k} = (k_x, 0, 0)$ is

$$\omega^2 \varepsilon_{xx}\left(\omega^2 \varepsilon_{zz} - k_x^2 c^2\right) - \omega^4 \varepsilon_{xz}^2 \tag{5.22}$$

Numerical calculations of the filamentary instability in the collisional and collisionless limits for the distributions of interest are shown in **Fig. 5.4** for the low temperature (5 keV) regime, where the imaginary part of the maximum growth mode is plotted in **Fig. 5.4(a)** and the corresponding real part is plotted in **Fig. 5.4(b)**. As one can see in **Fig. 5.4(a)**, collisions have little overall effect on the maximum growth rate for all K with the dispersion curves for each of the saddle point/Jüttner and the relativistic waterbag distributions being comparable in this regime. At lower K, there is a slight increase in growth due to collisions, followed by a point of overlap. However, after this point, the curves with finite collision frequency develop a clearly observable "kink." At this transitional point, the filamentary branch, which is characteristically a purely growing instability, develops a finite real frequency, which appears to grow with K, as shown in **Fig. 5.4(b)** where the transition to nonzero real frequency can be matched with the location of the "kink" in **Fig. 5.4(a)**. One can understand this kink more quantitatively by plotting the zero contours of the dispersion relation in $\omega_i - \omega_r$ space where the roots are found by locating the intersection point of the real and imaginary zero contour curves, shown in **Fig. 5.5**. As one can see in this figure, there are initially two purely growing roots before the kink and as K increases,

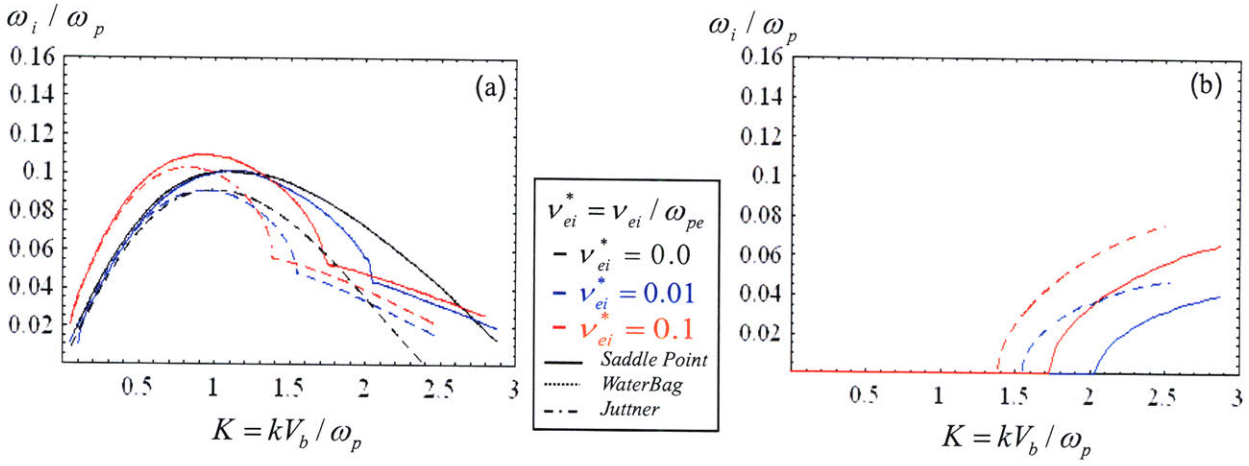

Fig. 5.4. Filamentary instability growth rate (a) and corresponding real frequency (b) for the saddle point (solid) and the waterbag (dashed), and for a range of collision frequencies in the low temperature (5keV) regime.

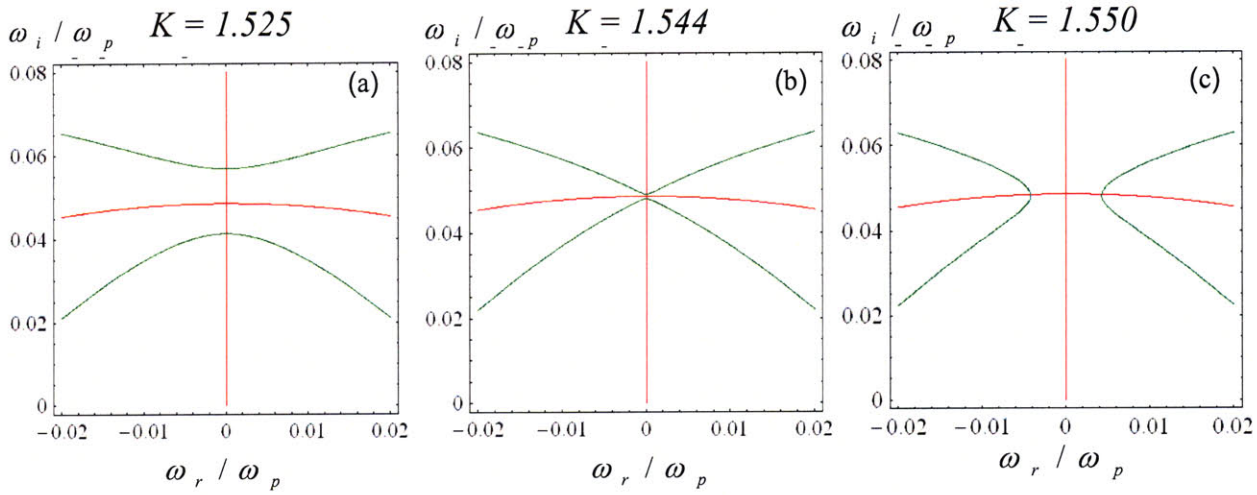

Fig. 5.5. Zero contours of the filamentary instability in $\omega_i - \omega_r$ for the relativistic waterbag distribution before the kink (a), at the kink (b), and after the "kink" (c). Red corresponds dispersion relation's imaginary part and green corresponds to the real part.

the two roots intersect precisely where the kink appears in **Fig. 5.5**. Beyond the kink at higher K, the two roots split horizontally along the ω_r axis where each root now obtains a finite real frequency. This effect in which collisions enhance growth at "low K" and suppress growth at "high K" was also noted by Deutsch et al. [65]. LSP simulations are similarly in reasonable agreement with analytical theory, yielding growth rate results within approximately 15-25% of those predicted by theory, and like the two-stream results, most of the difference lies with the collisional runs. However, given that growth rate extraction for this instability is from 2D simulations and is being grown from noise, the difference is expected. Like the two-stream instability, the filamentary instability can be reduced with beam temperature in both the collisional and collisionless limits, as can be seen by comparing **Figs. 5.6(a)** and **5.6(b)**.

It should be noted that recent work by Gremillet et al.[53] using a collisionless variation of the waterbag distribution claimed the existence of a threshold temperature above which the dominant oblique wave becomes purely longitudinal and all filamentary modes are completely suppressed. Although an exhaustive 2D calculation of this phenomenon is beyond the scope of this paper, we performed a temperature study with our fully covariant relativistic waterbag distribution within and much higher than the published temperature range. No threshold

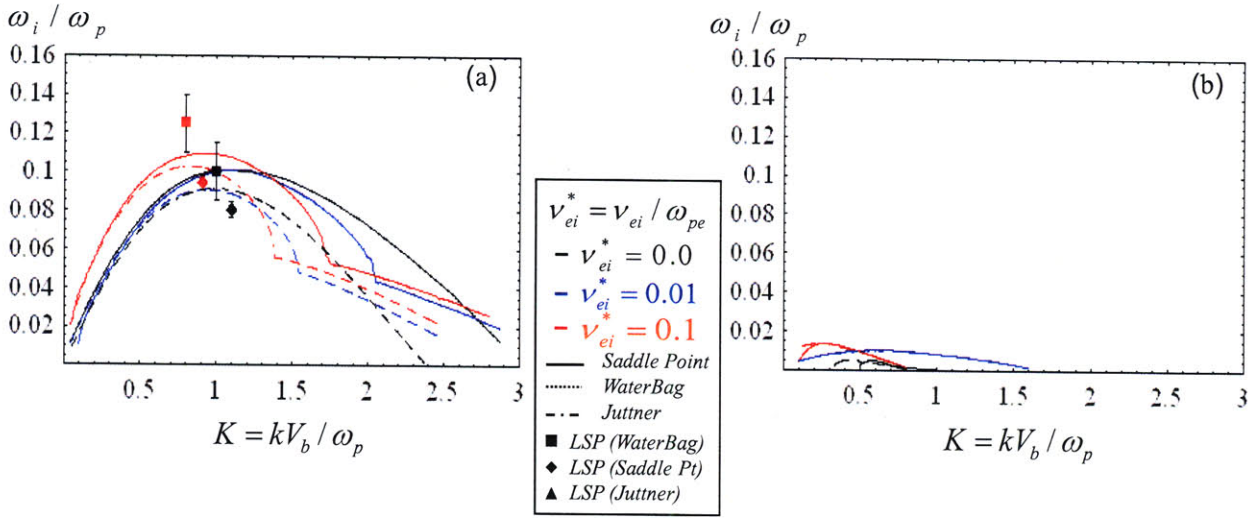

Fig. 5.6. Filamentary instability growth rate for the saddle point (solid), waterbag (dashed), and the Jöttner (dot-dashed) for a range of collision frequencies in the low temperature (5keV)regime (a) and high temperature (250 keV) regime(b).

temperature was found in the collisionless limit that was capable of completely suppressing filamentary modes (i.e., a finite, but very small growth rate could always be found for a wide range of temperatures). These conflicting results could be attributed to differences in the initial distribution structure but should be duly noted. Furthermore, earlier work by Molvig showed that when a finite collision frequency does exist, the filamentary instability cannot be stabilized with temperature, requiring an applied magnetic field to completely suppress these modes [49]. Our results also confirm this inability to suppress the filamentary instability with temperature for finite collision frequencies within the wide temperature range mentioned above.

5.5.3 Plasma Density Effects

For the previous analytical calculations, a beam-to-plasma density ratio of $\alpha = n_b/n_p = 0.1$ was conveniently chosen due to the higher growth rates that are expected, which make them more easily extractable from simulations. However, because the guiding cone that is to be inserted into fast ignition targets will allow the beam electrons to begin transport closer to the core and at higher densities along the plasma corona, it is necessary to examine instability growth rates with smaller beam-to-plasma density ratios ($\alpha << 0.1$). The previous instability

calculations showed that the relativistic waterbag can produce instability growth curves similar to more complex distributions. Therefore, due to its simplicity, it will be used for the analysis that follows.

In **Fig. 5.7**, filamentary instability growth curves are shown for both the high and low temperature regimes for beam-to-plasma densities of $\alpha = 0.1, 0.01, 0.001$. As one can see, the instability growth decreases with decreasing values of α in both the high and low temperature regimes. Physically, this means that the closer the beam is generated to the compressed fuel core (for a fixed beam density), the lower the growth rate will be. In the collisionless limit, the peak growth rate has an approximately linear dependence on α However, as **Fig. 5.7** shows,

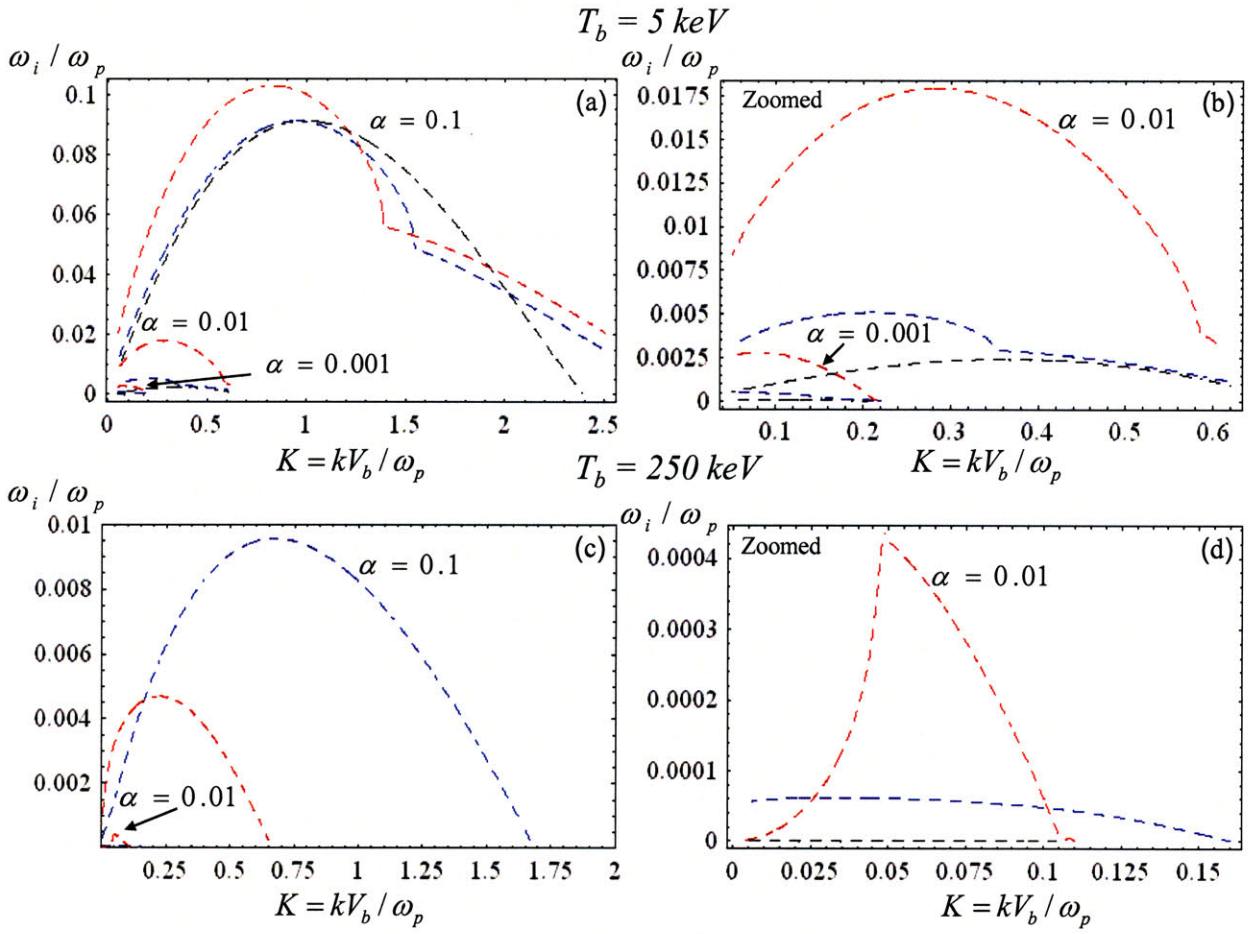

Fig. 5.7. Filamentary instability growth rate for the relativistic waterbag distribution for various values of the beam-to-plasma density ratio, α, in the low temperature regime (a,b(zoomed)) and the high temperature regime (c,d(zoomed)).

this dependence becomes more complicated in the collisional regime, as the instability growth rate appears to be dominated by the dispersion relations with finite collision frequency over a significant range of K . In fact, in the high temperature regime, collisional growth rates can be up to several orders of magnitude larger than those without collisions.

5.6 Beam Distribution from an Explicit PIC Simulation

Up to this point, dispersion curves have been generated for theoretical distributions whose temperature and drift parameters were loosely tied to those measured from experiments. However, a more physically based model for the distribution can be obtained from explicit PIC simulations of the laser plasma interaction. Z3, a fully relativistic, 3D collisionless PIC code, has been used to model a range of short-pulse, high intensity laser-plasma interactions [66].

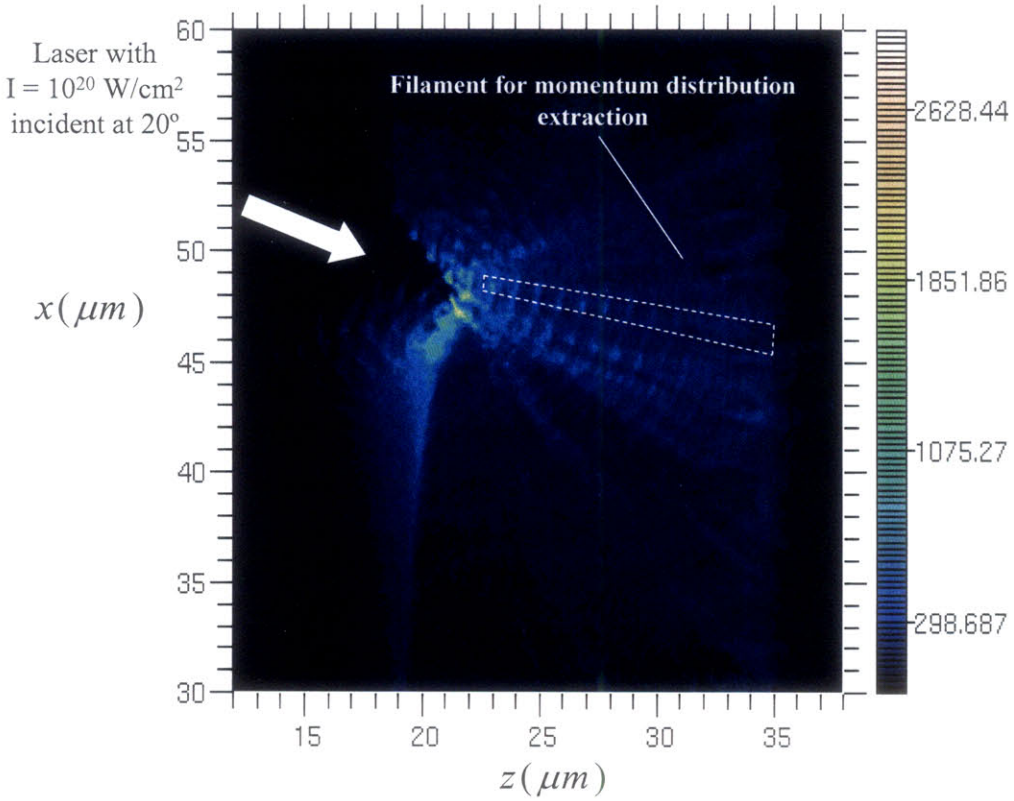

Fig. 5.8. 2D explicit simulation of a laser plasma interaction at 0.51 picoseconds showing the density of all particles with $\gamma > 2$. The filament used for extraction of the momentum distribution is outlined with white dashes.

The 2D simulation that will be analyzed in the paragraphs that follow consisted of modeling a laser with an intensity of $1x10^{20}$ W/cm^2 incident at a glancing angle of 20 degrees onto a plasma slab. As shown in **Fig. 5.8**, density contours of the individual particles portray the familiar current filaments that fan outward from the point of interaction. It should be noted that in order to distinguish between the background and beam electron species, only electrons with $\gamma > 2$ were selected from the simulation.

The momentum distribution of a single filament in the direction of the laser was used for analysis, rather than that of the entire simulation space. In **Fig. 5.8**, the chosen filament has been outlined in white. Histograms of the longitudinal (F_z) and transverse (F_x) momentum distributions within the filament have been plotted in **Fig. 5.9**. Of the three theoretical distributions of interest, only the Jüttner was able to capture both the asymmetric peak and long tail portrayed by the particle data in the longitudinal direction with fit parameters of $\beta_b = 0.76$ and $T_b = 531\ keV$. It should be noted that these fit parameters were evaluated with the chi-squared test as a "goodness-of-fit" assessment and yielded a χ^2 value of 104 for 78 degrees of freedom, which is approximately within the desired 95% confidence interval. Also shown in

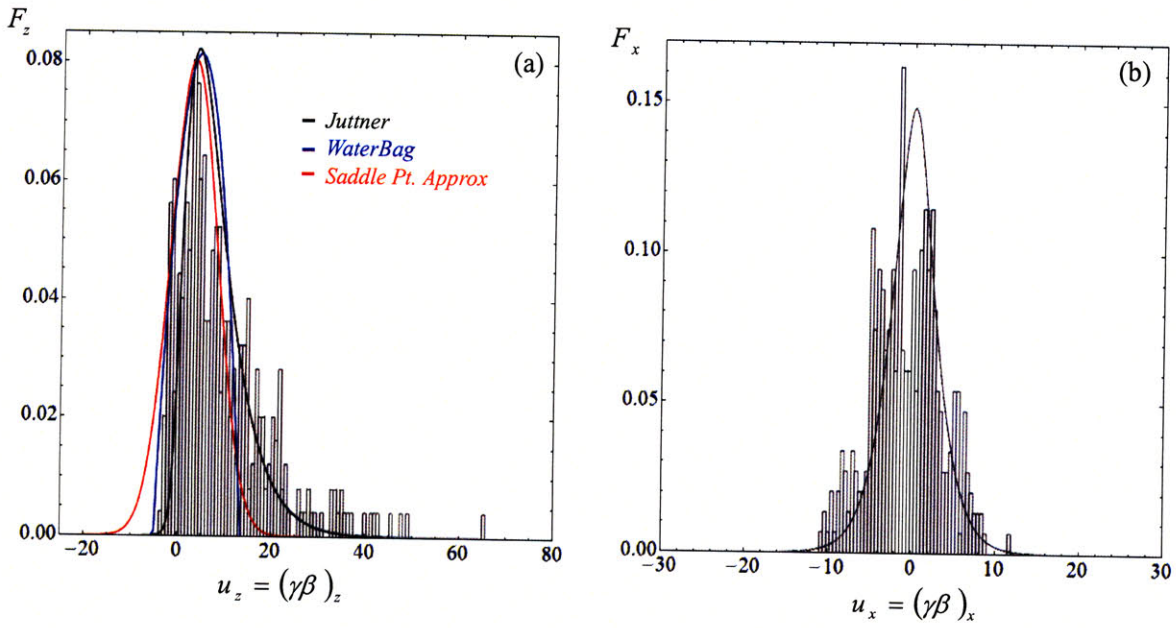

Fig. 5.9. Histograms of the longitudinal (a) and transverse (b) momentum distributions extracted from a 2D explicit PIC simulation, along with best fits to the Jüttner, waterbag, and saddle point approximation.

Fig. 5.9 are overlays of fits for the relativistic waterbag and saddle point distributions, showing poor agreement with the data due to their symmetric nature. Ultimately, the instability growth rate of this particle distribution is of primary concern so numerical calculations of both the filamentary and two-stream instability were computed with the fit parameters mentioned previously. As one can see in **Fig. 5.10**, the two-stream instability appears to be the clearly dominant instability in the collisionless limit, with the peak occurring at high K (K > 1) with a growth rate over two orders of magnitude greater than the filamentary at low K (K < 1). However, in the collisional regime, the two-stream instability appears to be almost completely suppressed, while the filamentary instability growth actually increases with collisions at low K.

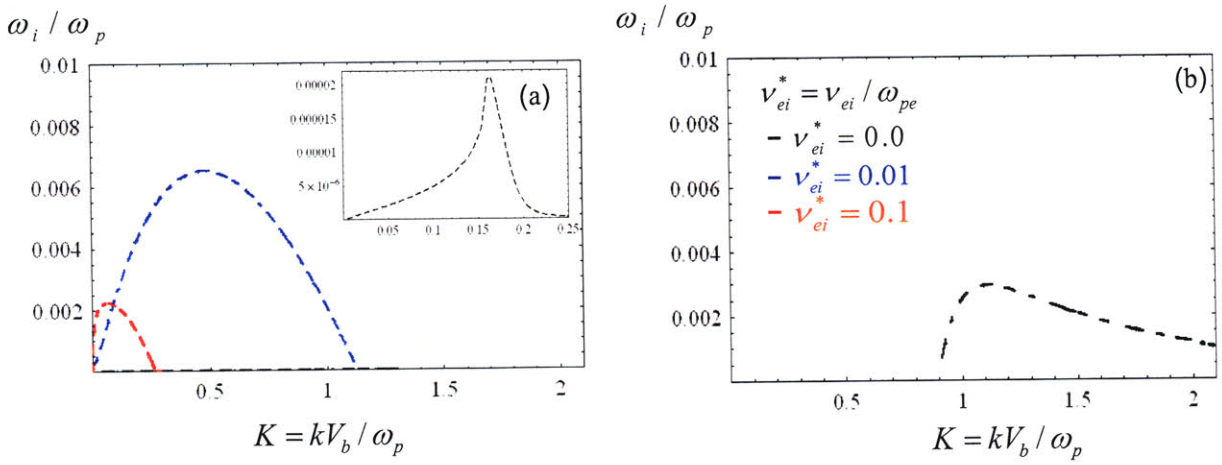

Fig. 5.10. Growth rates of the filamentary (a) and two-stream instabilities (b) for the best fit Jöttner parameters ($\beta_b = 0.76$ and $T_b = 531$ keV) to the 2D Z3 explicit PIC simulation data.

5.7 Conclusions

Relativistic beam transport is a critical element of the electron-driven fast ignition scenario and so it is important to understand how the various micro-instabilities to which it is vulnerable may inhibit transport. Because the specific form of the beam distribution has, for the

most part, eluded researchers up to this time, theoretical distributions whose temperature and drift parameters were loosely tied to those measured from experiments have been used for instability growth calculations, as well as computational modeling. However, this study has demonstrated that the structure of the distribution, as well as collisions, can strongly affect instability growth.

In general, kinetic and collisional effects have been shown to have disparate effects on each of the instabilities of interest. Specifically, at relatively low temperature, the saddle point, Jüttner, and the relativistic waterbag distributions appear to have comparable maximum linear mode growth rates for the two-stream instability in both the collisionless and collisional limits, with collisions acting to damp growth. At higher temperatures, the two-stream can be suppressed; however, in this regime, where the saddle point approximation to the Jüttner distribution is no longer valid, the saddle point approximation greatly underestimates the growth rate. Unlike the two-stream instability, collisions have only a minimal effect on the growth rate of the filamentary instability in the low temperature regime, yielding comparable maximum linear mode growth rates for each of the theoretical distributions. However, collisions do create an unusual "kink" in the growth rate that forces the normally purely growing filamentary instability to transition to a growing/oscillating state, with the oscillation frequency increasing with K. For wave numbers less than the location of the kink, collisions appear to enhance growth, while for wave numbers greater than the location of the kink, collisions damp growth. Although collisions alone do not appear to be capable of damping the filamentary instability, an increase in beam temperature can achieve damping. In sum, these results suggest that one could use the relativistic waterbag distribution to model the relativistic beam in both the high and low temperature limits with minimal error since it is the mathematically simplest distribution of the three and retains the essential instability features. That being said, the relativistic waterbag was used to show that filamentary instability growth decreases with decreasing values of α, the beam-to-plasma density ratio, in both the high and low temperature regimes, suggesting that instability growth becomes less significant the closer the beam begins transport (at higher densities) to the compressed fuel core.

A more physically-based distribution was also obtained from 2D explicit PIC simulations whose results have shown that the relativistic electron beam filament can be best modeled with a Jüttner distribution. In this parameter regime, the maximum growth appears to

be dominated by the filamentary instability with finite collision frequency at low K ($K < 1$) and by the two-stream instability in the collisionless limit at high K ($K > 1$). Although the exact Jüttner distribution was used to compute these dispersion curves, future calculations could use the mathematically simpler relativistic waterbag distribution for reasonable approximations to instability growth.

Chapter 6

Nonlinear Evolution of Fast Ignition Relevant Beam Instabilities and Electron Transport Implications

6.1 Introduction

Thus far, this work has focused primarily on the linear growth regime of fast ignition relevant beam instabilities with little mention of the effects these instabilities will have on hot electron transport once this regime ends and saturation ensues. However, it is the nonlinear saturated state of these instabilities that will dictate how efficiently the hot electrons will transport the laser energy to the dense fuel core for ignition. An initial study of the linear growth regime has proven to be essential for understanding the nonlinear saturated regime due to the intimate coupling of the two stages. When the hot electrons are produced during the laser plasma interaction and a return current develops, the electromagnetic fields are relatively weak and have minimal effect on the overall electron transport during this period. However, because these fields are growing at a rate of the order of the plasma frequency, they eventually saturate

at a significantly higher level, enabling them to strongly influence the remaining beam transport. In principle, both the two-stream and filamentary instability modes will be growing simultaneously for the counter-streaming beam-plasma problem of interest. However, as was shown in Chapter 5, the filamentary instability will be of greater concern for the parameters of interest.

Given the importance of the saturated magnetic field level, it suffices to acquire an understanding of the mechanism which saturates the instability. Early work by Manheimer and Davidson on the nonlinear development of electromagnetic beam instabilities attributed saturation to the process of "magnetic trapping" [67,68]. According to their results, the initial instability grows as the beam particles continue to feed energy into the magnetic field perturbation. However, as the field perturbation reaches a sufficient level, the gyro-radius of the particles within the wave becomes sufficiently small such that they become trapped in the wave's magnetic potential well. With time, more and more particles become trapped by the increasingly large magnetic field such that less and less energy gets fed into the wave and growth ceases. Manheimer identified this point of stabilization as the time at which the magnetic bounce frequency of the particles,

$$\omega_B = \sqrt{\left|\frac{ekV\overline{B}}{mc}\right|}, \tag{6.1}$$

is of approximately the same order as the growth rate of the most unstable mode, i.e.,

$$\omega_B \sim \gamma . \tag{6.2}$$

At this point, a saturated state of the instability has been reached which can be characterized by the saturated magnetic field amplitude, $\overline{B}_{sat}$ [67].

With this in mind, the goal of this work is to understand the effects of the parameters of the initial beam-plasma state (i.e., temperature, drift, background density) and collisions on magnetic trapping and the ensuing saturated magnetic field amplitude. In Section 6.2, I will review a subset of published results on the nonlinear evolution of fast ignition relevant beam instabilities and significant features of interest. In Section 6.3, it will be demonstrated that the

LSP code has been used to successfully reproduce these features in both 1D and 2D, providing confidence for extrapolation into the collisional regime. Section 6.4 will follow with a series of simulations highlighting the effects of the initial beam parameters, background density, and collisions on filamentary features in the nonlinear regime. This work will be complemented in Section 6.5 with an analysis of how the instability generated magnetic field affects particle orbits for a range of parameters and conditions and the effect on apparent stopping power and range. Finally, in the concluding discussion of Section 6.6, we will be able to address the ultimate question as to what conditions we should care about instabilities at all.

6.2 Overview of Nonlinear Beam Saturation Literature to Date

The most extensive published work on the saturation of beam-plasma instabilities and most relevant to the fast ignition scheme consists of a series of six papers published by F. Califano et al. He began his analysis in the first paper with a simple collisionless fluid formulation for the beam and plasma electron species in which he showed the development of a spatial "resonant"-type singularity in the electron beam densities and magnetic field as the instability transitioned to smaller and smaller spatial scales [55]. This small scale generation was shown to continue indefinitely to the order of characteristic kinetic scales (such as the electron gyro-radius) and lower, at which point the fluid model was deemed insufficient at this point [55].

To improve upon the fluid analysis, Califano extended his results in a later paper with the inclusion of kinetic effects by integrating numerically the Vlasov equation coupled to Maxwell equations [69]. Like the fluid formulation results, he saw the generation of larger and larger wave numbers (smaller and smaller spatial scales); however, the inclusion of kinetic effects showed no sign of divergence or singularities since the cascade to small spatial scales was interrupted at the collisionless skin depth. From phase space plots of the electron beams, Califano also saw the rotation of the electron velocities around the peaks of the magnetic field. This effect can be attributed to the mechanism of magnetic trapping which was identified in earlier publications by W. Manheimer, R. Davidson, etc. as a source of mode stabilization [67,68]. During the transition from the linear to nonlinear regime, the electron gyro-radius

decreases until it and the spatial scale of the perturbation, $\lambda = 2\pi/k$, become of the same order as the electron skin depth, at which point the small scale generation process stops and the instability saturates [69]. An equivalent saturation condition is also found in the literature that requires that the magnetic bounce frequency, ω_b, be comparable to the growth rate, γ [67].

Califano continued his kinetic analysis of the spatial structures of the current and magnetic fields generated by the filamentary instability in the third paper of the series with the goal of identifying features that can be used as signatures in experimental results [70]. In his analysis of the nonlinear evolution of this instability in 1D, he found that for relativistic beams, the resulting structure of the current and magnetic fields in the nonlinear phase are independent of the initial conditions, i.e., the phase and wave number of the initial perturbation. In addition, he found a similar result in 2D, but the main effect observed in these simulations was the pinching of several physical quantities (i.e., magnetic field, density, transverse electric field) in the transverse direction. In the non-relativistic regime, he observed a somewhat modulated, arrow-like structure along the direction of the beam; however, as the beam became more relativistic, the beam/filaments became more homogeneous along the longitudinal direction. One final effect he observed was the generation of a relatively large electrostatic field transverse to the beam direction. In the linear regime, this electrostatic field was negligible, but as the instability transitioned into the nonlinear phase, it actually dominated the magnetic term in the Lorentz force [70].

In a pair of PRLs that followed, Califano used his analysis of the nonlinear evolution of the electromagnetic beam-plasma instability to explain the formation of magnetic vortices observed in 2D PIC simulations in the wake of an ultra-intense laser pulse [71,72]. Califano showed that a fast kinetic mechanism, based on the resonant wave-particle-interaction, is capable of generating magnetic vortices on the electron time scale. Using a 2D-2V Vlasov-Maxwell code, he was able to reproduce a series of magnetic vortex pairs with typical dimensions of the electron skin depth along the beam direction, consistent with the global structure seen in the magnetic wake of 2D PIC simulations of the laser pulse interaction with under-dense plasma. In these Vlasov simulations, the vortices are stable for a finite time and appear to propagate in the beam direction at a phase velocity comparable with the velocity of the beam. According to Califano, the generation of vortices can be attributed to the resonant interaction between the 2D electromagnetic beam-plasma instability mode and the particles in

the fast beam. This is verified by the classic signature of the resonant wave-particle interaction seen in phase space plots of the longitudinal beam velocity showing electron trapping along the beam direction, which accounts for the bunching of density parallel to the beam [72].

The final paper published by Califano in 2002 explored the fully nonlinear kinetic regime of the beam plasma instability with the inclusion of ion dynamics [73]. In his previous formulations, Califano limited his analysis to electron dynamics, considering the ions as a fixed neutralizing background. Although this approximation is valid in the linear regime, Califano showed that during the very early nonlinear phase of the instability and for longer times, ion dynamics cannot be neglected. More specifically, ponderomotive effects in the nonlinear regime create electron cavities and because of the electrostatic field resulting from the charge separation, ion cavities are then formed. From Vlasov simulations, Califano showed that in the long-time nonlinear regime, the system eventually manages to impose quasineutrality on the initial inhomogeneous configuration [73].

A recent paper by Gremillet also explored the linear and nonlinear features of the electromagnetic beam-plasma instability in a fully relativistic framework, but unlike Califano, he focused more on the oblique nature of the modes [57]. Using the model developed by Bret et al., he successfully benchmarked the oblique mode theory with PIC simulation. Gremillet then extended his simulations into the nonlinear regime where he showed that beam trapping is clearly visible [56]. In phase space plots of the particles from 2D PIC simulations, he observed the familiar vortex structures which suggest complete trapping in the potential troughs of the dominant wave. However, a less obvious result from this work was the partial trapping of plasma electrons, which he attributed to the strong wave-particle interaction between the relatively slower oblique waves and the bulk plasma electrons [57].

One final publication worth mentioning is work done by Okada et al. in the last year in which in which he compares theoretical results involving linear growth rates and the amplitude of the saturated magnetic field with that of 3D PIC simulations of ultra-intense laser plasma interactions [74]. According to the literature, the purely transverse filamentary instability growth rate for a relativistic bi-Maxwellian takes on a maximum value of

$$\Gamma^{T} = \sqrt{\frac{8}{27\pi}}\sqrt{\frac{T_{\perp}}{mc^{2}}}\frac{A^{3/2}}{A+1}\omega_{ph}, \tag{6.3}$$

where the transverse wave number, k_z is defined as

$$k_z = \sqrt{\frac{A}{3}}\frac{\omega_{ph}}{c}, \tag{6.4}$$

ω_{ph} is the beam frequency, $A = T_{\|} / T_{\perp} - 1$, and $T_{\|}$ and $T_{\perp}$ are the temperatures parallel and perpendicular to the beam direction, respectively. According to Okada, the high energy electron trapping that causes instability saturation happens due to both magnetic and electrostatic fields, but magnetic trapping is the dominant mechanism. Since the literature has found that this occurs when the magnetic bounce frequency, ω_b, increases to a value comparable to the linear growth rate, Γ_T [67,68], one can derive an analytical expression for the saturated magnetic field,

$$\Gamma^T \cong \omega_b \equiv \sqrt{\frac{ek_{\perp}u_{\|}B^T}{\gamma^2 mc}} \tag{6.5}$$

$$\rightarrow B^T = \frac{8\sqrt{3}}{27\pi}\sqrt{\frac{T_{\|}}{mc^2}}\frac{A^{5/2}}{(A+1)^3}\frac{\gamma^2 m\omega_{ph}c}{e}, \tag{6.6}$$

where B_T is the saturated magnetic field amplitude and $u_{\|} = \sqrt{T_{\|}/m}$. By relating the temperature to the ponderomotive potential and taking the maximum value of the expression involving A, the saturated magnetic field can be simplified as

$$B^T \cong 3.48\times10^{-2} I_{18}\sqrt{\frac{n_e}{n_c}}B_0, \tag{6.7}$$

where n_e is the hot electron density, B_0 is the laser magnetic field, and I_{18} is the peak laser intensity in units of 10^{18} W/cm^2. From this expression, Okada concluded that the saturated magnetic fields are determined by the laser intensity and plasma density. Furthermore, 3D PIC simulations of a laser plasma interaction were shown to be in good agreement with both the maximum growth rate and the saturated magnetic field [74].

6.3 Magnetic Trapping and Saturation Effects

The previous section highlighted a number of significant features associated with magnetic trapping and the saturated regime such as magnetic vortex formation, intertwined filament production, ion cavitation, etc. from earlier published results [67-74]. Because the ultimate goal is to extend this work into regimes that include collisions and a range of initial parameters using the LSP code, it suffices to first verify that LSP reproduces these features correctly.

6.3.1 1D Saturation Effects

As was noted by Califano, a significant understanding of magnetic trapping can be gained from a simple 1D simulation of the filamentary instability. Shown in **Fig. 6.1** is a schematic of the simulation geometry used in LSP to model the filamentary instability for the counter-streaming beam-plasma problem. The simulation box was chosen to be one wavelength of the maximum growing mode in the transverse z-direction with periodic boundary conditions on each edge. The usual resolution parameters were chosen as 31 cells per wavelength, 20 time-steps per plasma period, and 100 particles-per-cell. The hot electron and return current distributions were defined as cold beam distributions ($T_b = T_p = 0$) with drift velocities initiated in the x-direction of $\beta_b = 0.94$ and $\beta_p = -0.094$, respectively, and the beam-to-plasma density ratio was chosen as $\alpha = n_b/n_p = 0.1$. Ions were included and were assumed cold and motionless. Although these parameters are not representative of the fast ignition relevant beam and plasma conditions that

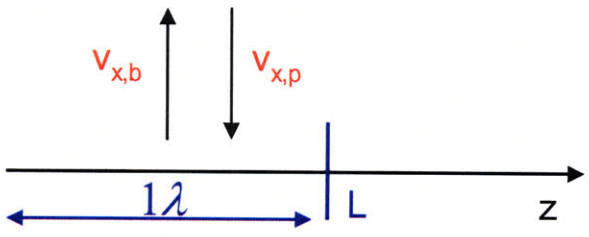

Fig.6.1. Schematic of the 1D simulation geometry used to model filamentary instability growth in LSP.

are to be expected, they allow for a number of advantages such as easier instability growth analyses due to higher growth rates, ideal conditions for collisional analyses due to higher collision rates, and significantly less noise for observing saturation features.

For the filamentary instability in this particular geometry, the parameter of interest is B_y. Shown in **Fig. 6.2(a)** is the profile of $B_y(z)$ during the linear regime until saturation, as well as the Fourier analysis of the maximum growth mode used for growth rate extraction in **Fig. 6.2(b)** (see Chapter 3 for additional details on growth rate extraction). As one can see, the magnetic field profile maintains an approximately sinusoidal form until saturation occurs at approximately $\omega_p t = 47$. At this point, if one computes the bounce frequency, ω_B, using equation 6.1 discussed previously, it is approximately $0.17\omega_p$, which is of the order of the growth rate, $\gamma \sim 0.18\omega_p$. This confirms the magnetic trapping criteria quoted by Manheimer and Davidson [67,68]. Furthermore, the dipolar magnetic field profile develops a very sharp, near-singular structure around the symmetry axis. These results are in agreement with Califano et al., which demonstrates the transition to smaller and smaller spatial scales as a significant number of particles begin to be trapped [69]. The mechanism of magnetic trapping can be seen more clearly from the evolution of the density profiles of the two electron species shown in **Fig.**

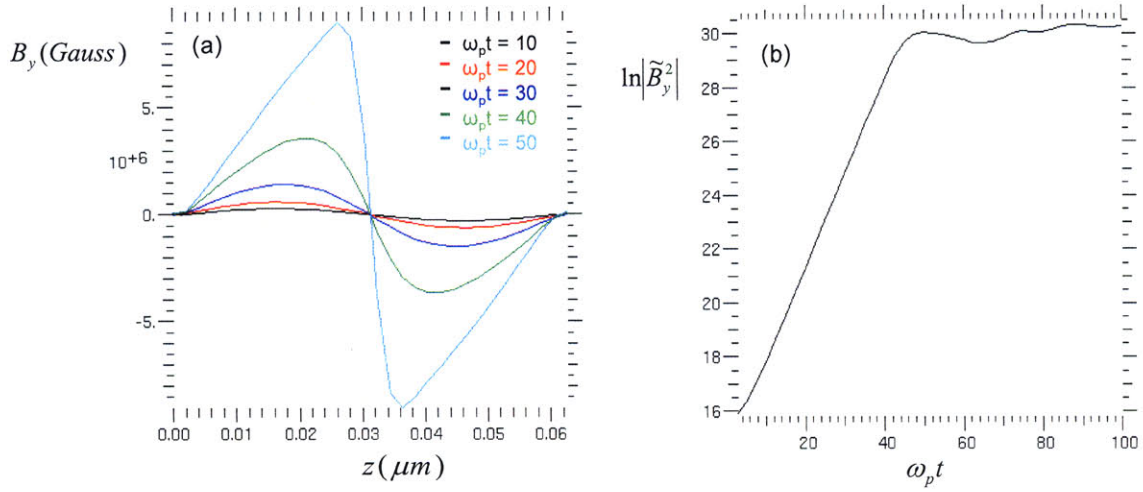

Fig.6.2. Evolution of the magnetic field profile during the linear growth regime and initial transition to the nonlinear saturated state (a) and the Fourier growth analysis of the maximum growth mode (b).

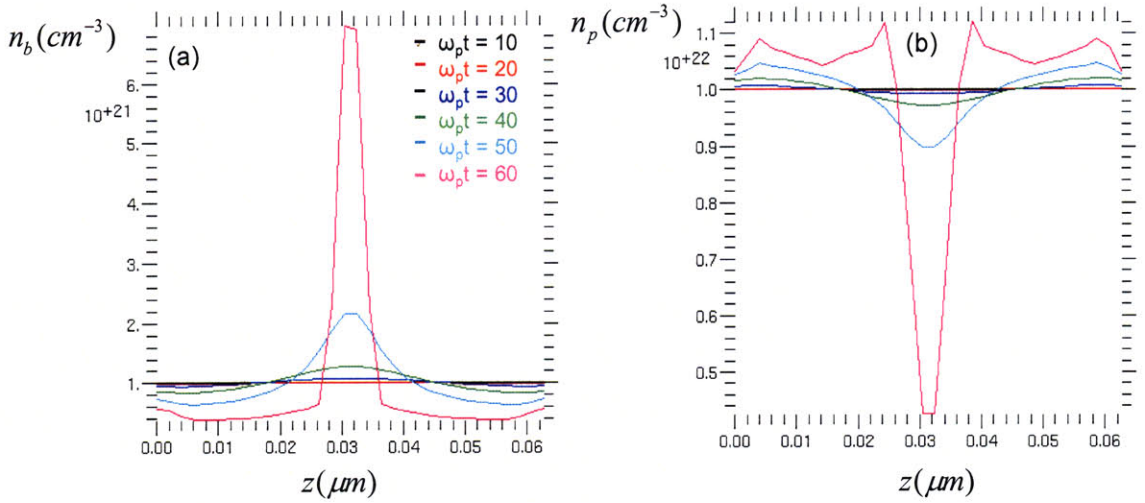

Fig.6.3. Evolution of the beam (a) and background plasma (b) density during the linear growth regime and into the initial nonlinear saturated regime.

6.3. From the figure, one can see that as time progresses, the initially sinusoidal perturbation develops into peaks and cavities concentrated around the magnetic field "singularity." At this point, the two electron populations become trapped in a structure that resembles a central fast current surrounded by two external return currents carried by the slower species. Additionally, the transverse phase space plots for each species reveal the gradual transition of the sinusoidal perturbation to vortices, as shown in **Fig. 6.4**, which is the classic signature of particle trapping.

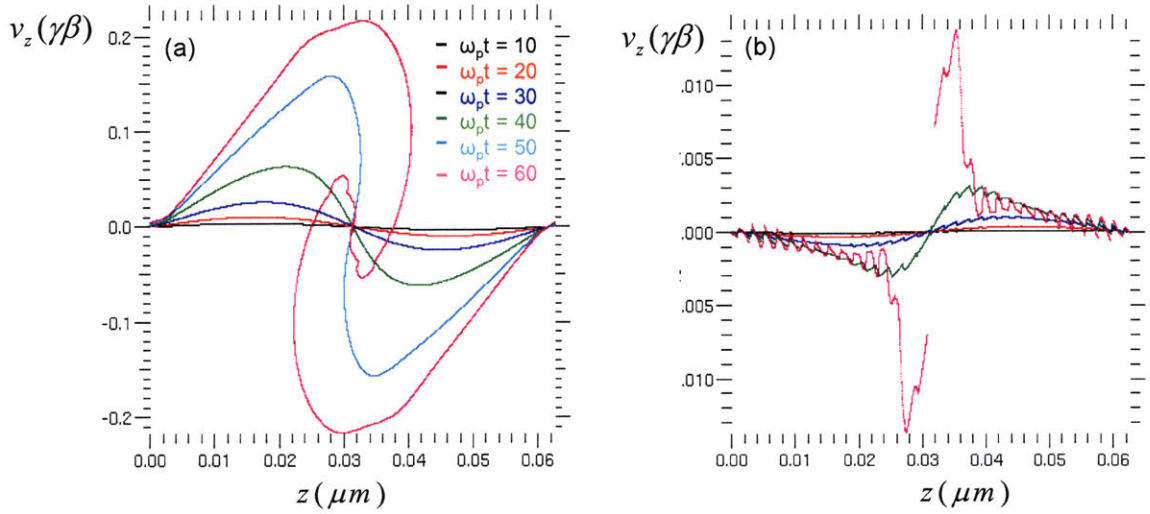

Fig.6.4. Transverse phase space plots of the evolution of the beam (a) and background plasma (b) from the linear to initial nonlinear regimes.

One final feature worth mentioning is the importance of ion dynamics for times longer than the extent of the linear regime. Shown in **Fig. 6.5** is the profile of the ion density at the end of the linear regime through the transition to the nonlinear regime. As one can see, density cavities begin to develop due to the electrostatic field resulting from the charge separation created by the electron peaks/cavities. As time progresses, the ions align themselves with electron peaks/cavities to try to restore quasi-neutrality, in agreement with the results of Califano et al [73].

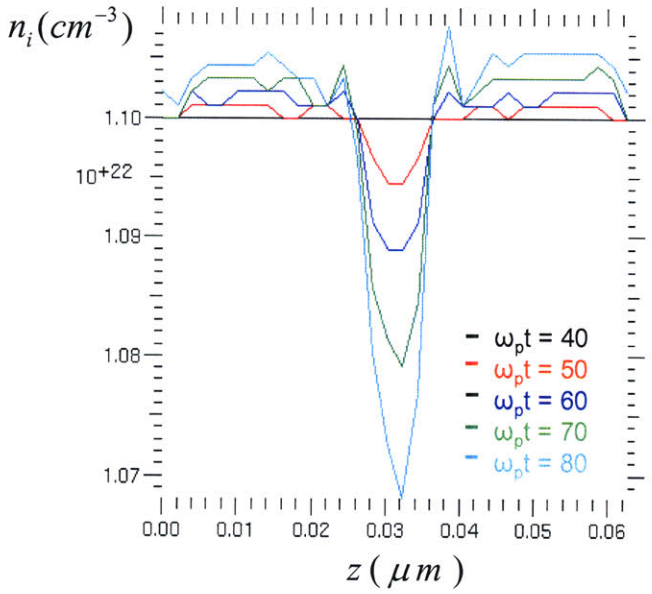

Fig.6.5. Development of ion cavitation for late times in the nonlinear regime.

6.3.2 2D Saturation Effects

A number of other significant saturation features arise in 2D that have been noted in earlier work and are deserving of attention. In order to reproduce these features in LSP, we devised a simulation in 2D Cartesian geometry shown in **Fig. 6.6**. This problem models the longitudinal (x-direction) and one dimension of the tranverse direction (z-direction). The transverse direction was chosen to be two wavelengths of the maximum growing mode and 1.0 micron in length along the beam direction with periodic boundary conditions on the top edges and symmetry (reflecting) boundary conditions on the left-right edges. Parameters identical to

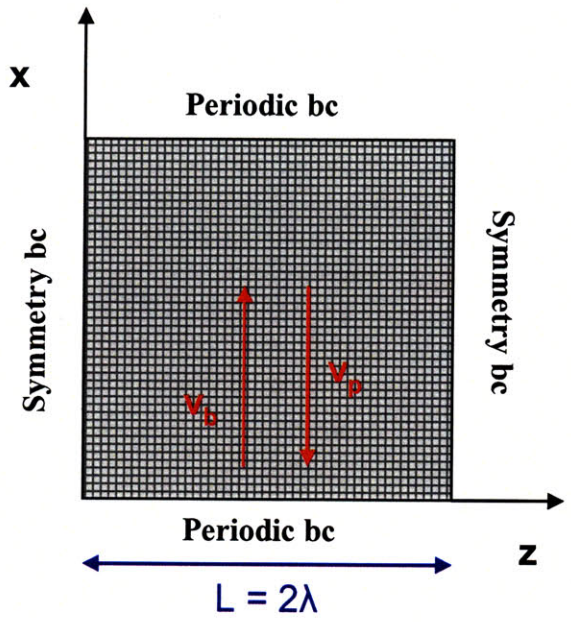

Fig.6.6. Schematic of the 2D simulation geometry used to model filamentary instability growth in LSP.

that of the 1D case were chosen, which consisted of cold beam and background plasma distributions ($T_b = T_p = 0$) with drift velocities initiated in the x-direction of $\beta_b = 0.94$ and $\beta_p = -0.094$, respectively, and the beam-to-plasma density ratio of $\alpha = n_b/n_p = 0.1$. The usual resolution parameters were chosen as 31 cells per wavelength, 20 time-steps per plasma period, and 100 particles-per-cell, as well.

One of the more interesting features that arises in 2D is the formation of magnetic vortices along the direction of the beam. Shown in **Fig.6.7(a)** is a plot of the magnetic field well into the nonlinear regime around $\omega_p t = 75$. As one can see, the usual dipolar magnetic field structure exists, as in the 1D case, but you also see a series of magnetic vortex pairs that develop along the direction of the beam that propagate in time. Shown in **Fig.6.7(b)** is a line-out of the magnetic field contour at $z = 0.075$ microns for $\omega_p t = 150$, 160, and 170. The profile appears to propagate at a velocity of approximately $v = 0.82c$, which is close to that of the beam drift velocity. As Califano et al. pointed out, these magnetic vortices are well correlated with the electron beam flow, shown in **Fig.6.8** [72]. As one can see from the phase space plot of the fast beam species in **Fig.6.8(a)**, vortices also develop along the direction of the beam, which is a clear signature of trapping due to wave-particle interactions. As a result of this trapping, one also sees density bunches along the beam direction, shown in **Fig. 6.8(b)**, which also propagate

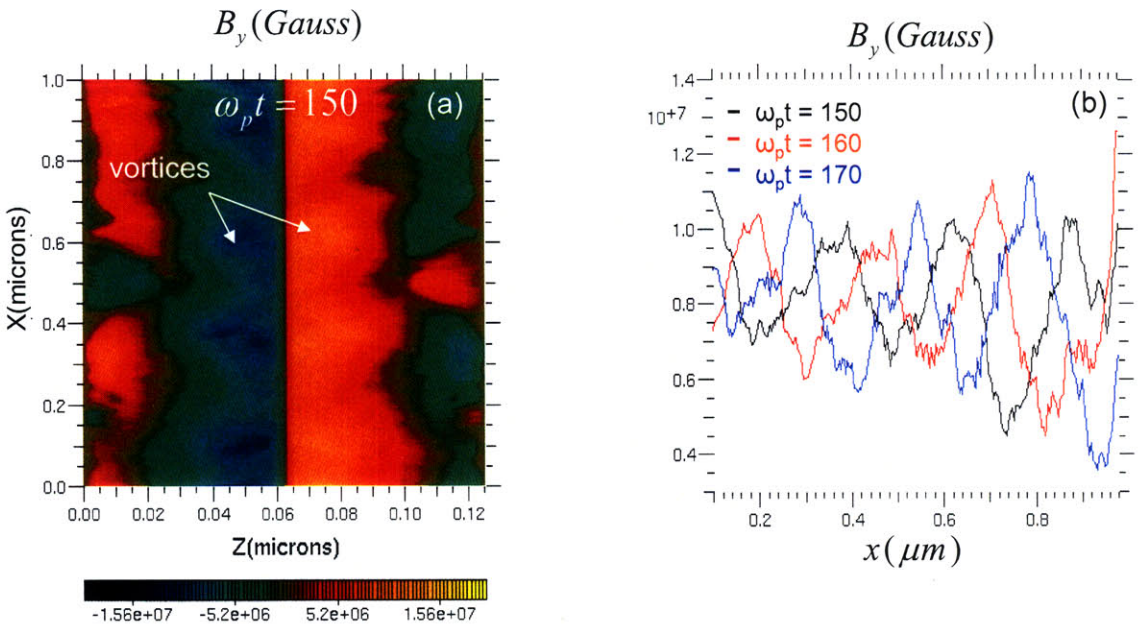

Fig.6.7. Contour of the 2D magnetic field and development of vortices in the nonlinear regime at $\omega_p t = 150$ (a) and line-outs of the magnetic field profile at $\omega_p t = 150$, 160, and 170 (b).

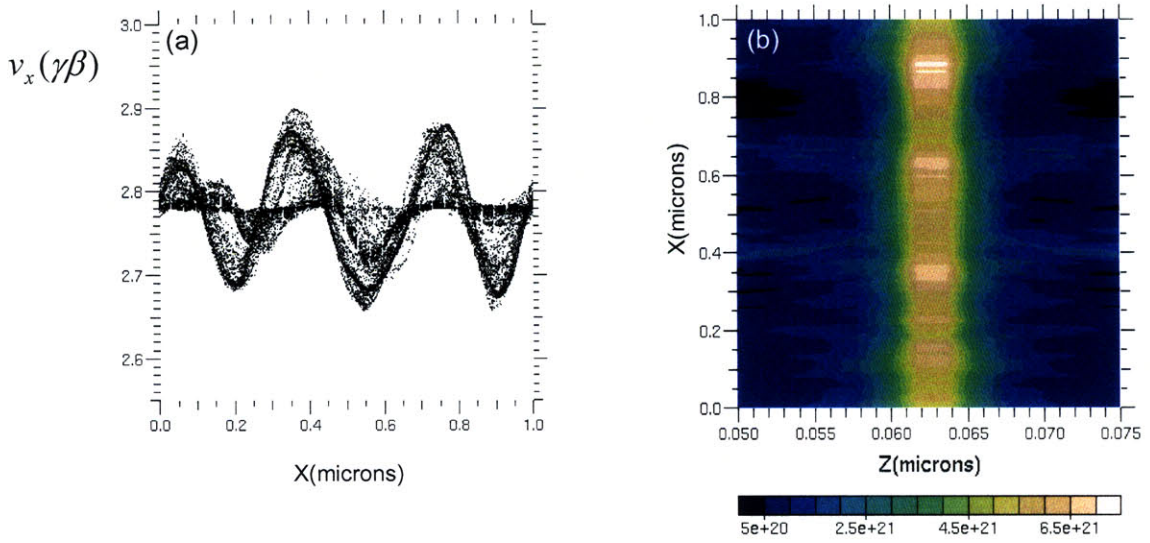

Fig.6.8. Phase space plots of the beam species along the beam direction (a) and a 2D contour of the particle density bunches along the beam direction (b).

in time at a velocity approximately equivalent to that of the beam velocity. In sum, these results confirm agreement between the LSP code and published results.

6.3.3 Effects of Collisions on Magnetic Trapping and Saturation

Before addressing the issue of collisions, it suffices to briefly discuss the saturation mechanism of non-symmetric ($n_b \neq n_p$, $v_b \neq v_p$) beams. As noted by Manheimer and Davidson, the point of saturation can be defined as the time at which the bounce frequency of particles within the beam becomes approximately equal to the growth rate of the instability [67,68]. An equivalent criteria was also derived by Califano et al. in which he identified the saturation point as the time at which the gyro-radius of particles within the beam becomes of the order of the electron skin depth. In the context of saturated magnetic field levels, this second criteria becomes significant when one tries to understand the saturation mechanism of non-symmetric beams. In this case, the point of saturation is determined by the slower, more dense return current because it is this species that becomes trapped first as a result of its slower drift velocity. When this happens, the gyro-radii of the fast beam particles are still quite a bit larger than the electron skin depth and still possess kinetic energy that has not had a chance to be converted to magnetic field energy [55]. This issue is significant in the context of collisions for relativistic beams because it is the slower background electron-ion collisions that are of greatest importance. Because the slower return current will be most affected, this will also impact the saturated magnetic field level, as will be shown.

To gain an initial understanding of collisional effects on magnetic trapping and saturation, we started with a simple 1D analysis in LSP identical to the collisionless 1D case discussed in section 6.3.1 consisting of cold counter-streaming beams with drifts of $\beta_b = 0.94$ and $\beta_p = -0.094$, respectively, and a beam-to-plasma density ratio of $\alpha = n_b/n_p = 0.1$. For the collisional case, we simply turned on the newly integrated relativistic Manheimer collision model described in Chapter 3. Shown in **Fig.6.9** is a Fourier analysis of the maximum growth mode. As one can see, the saturation level of the collisional case is slightly higher than the case with no collisions. This effect can be attributed to the impact of collisions between the slower, more dense return current and the ions. As mentioned previously, the trapping of particles within the slow return current determine the saturation level. When collisions are present, the slower particles that would have otherwise been trapped have the ability to scatter out of the

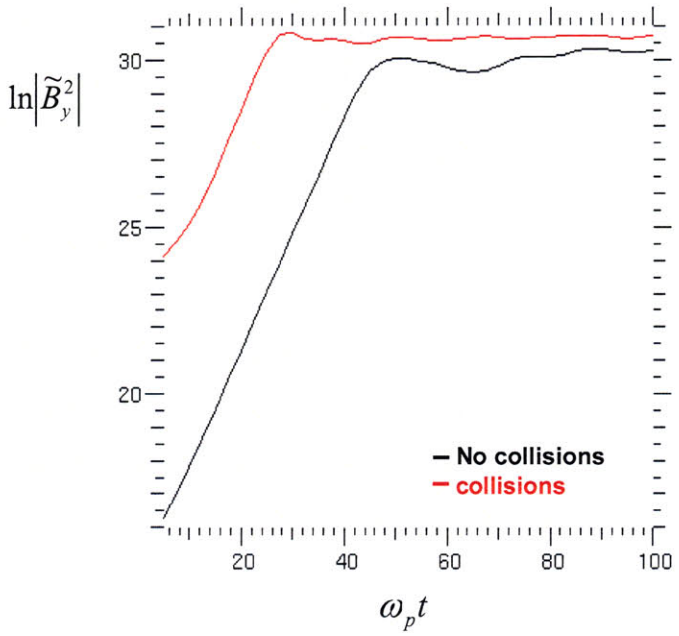

Fig.6.9. Fourier growth analysis of the maximum growth mode of the cold relativistic filamentary instability for the collisional (red) and collisionless (black) cases.

magnetic potential well. As a result, the perturbation velocities are able to reach places where they would otherwise be prohibited by the magnetic trapping. One can see this effect more clearly in phase space plots shown in **Fig. 6.10** of the slower background electron species over the course of the linear growth regime. Because these particles can reach higher velocities, this then leads to larger currents and subsequently larger magnetic fields. Also shown in **Fig. 6.11** are the current and magnetic field profiles for the collisionless and collisional runs which clearly reach larger amplitudes in the collisional runs, as predicted.

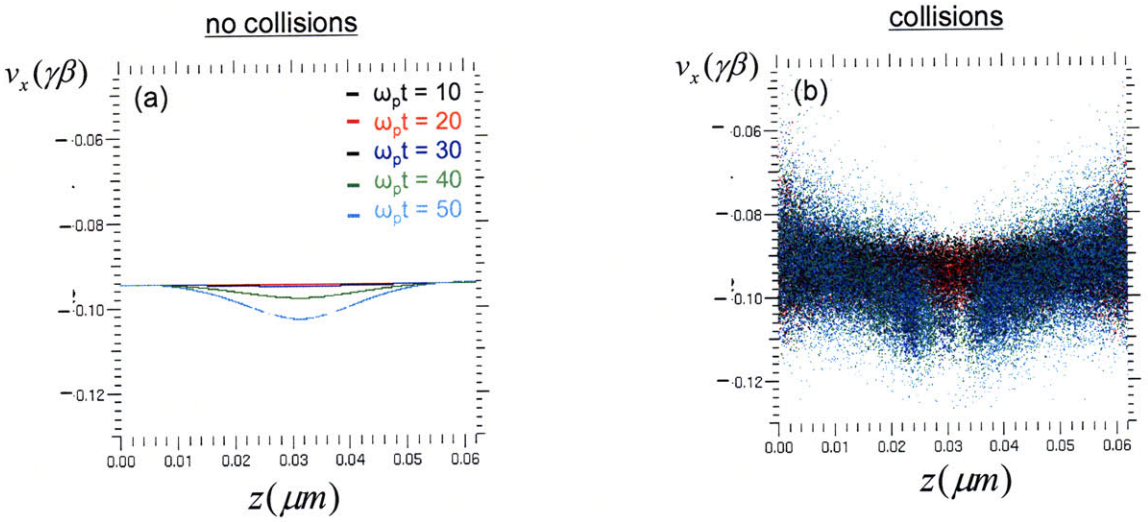

Fig.6.10. Phase space plots of the slower background species during the linear regime for the collisionless run (a) and the collisional run (b).

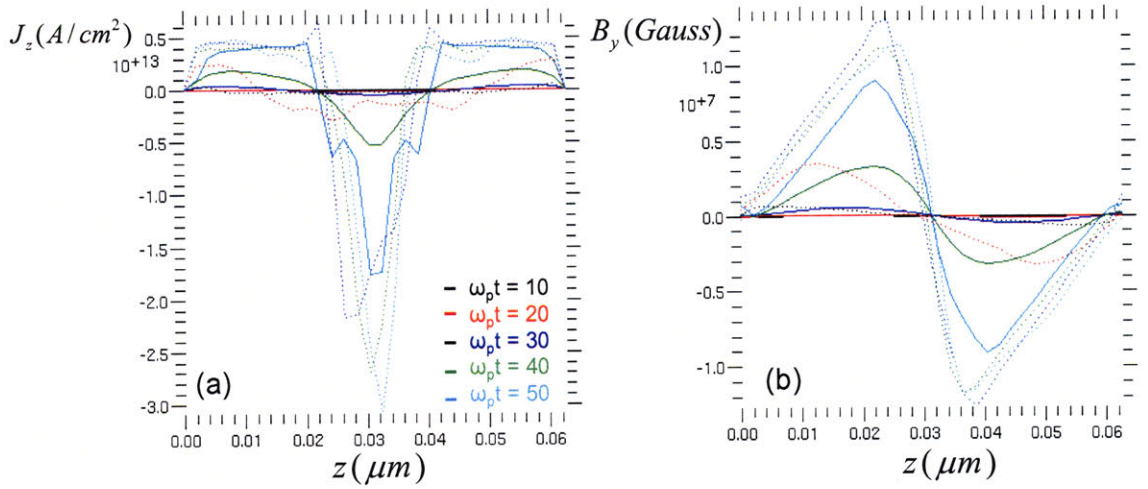

Fig.6.11. Current (a) and magnetic field (b) profiles with collisions (dotted) and without collisions (solid) over the course of the linear growth regime.

One additional source of magnetic field growth also comes from the production of electric fields by collisions that act to drag the return current. Because these fields are growing in time, their curl makes a contribution to the magnetic field. In order to see this effect, we simulated the same instability in 2D with parameters identical to those described previously. Shown in **Fig. 6.12** are contours of the transverse electric field for both the collisional and collisionless cases. As one can see, there is clearly a gradient along the direction of the beam (x-direction) for the collisional case, while there is no gradient in this direction for the collisionless case. This subsequently creates a magnetic field contribution in the y-direction.

It should be noted that the enhancement of the saturated magnetic field levels is only slight and is observed only under optimum conditions (cold beams) where the collision frequency is high. When we re-ran these cases with more realistic beam/background density parameters, virtually no difference was seen in the saturation levels.

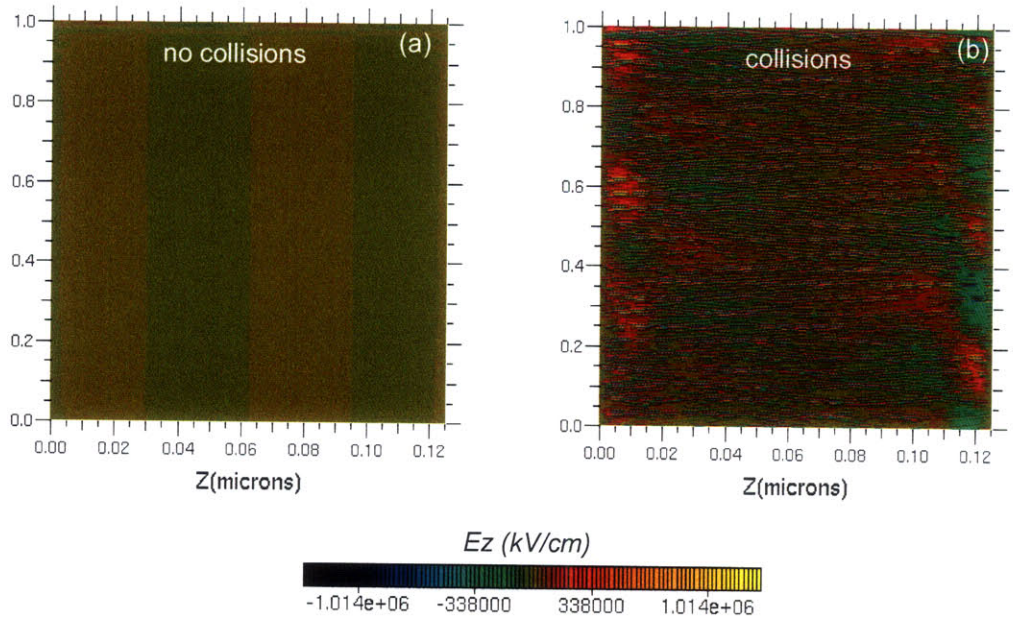

Fig.6.12. 2D contours of the transverse electric field for the collisionless (a) and collisional (b) runs during the linear regime at $\omega_p t = 50$.

6.4 Effects of Initial Conditions on the Nonlinear Saturated Regime for Extended Times

Thus far, the discussion of saturation has, for the most part, been purely academic, focusing on the effects of various initial conditions and collisions for only extreme cases. Parameters were chosen such that the growth and saturation features could be easily observed and extracted from numerical PIC simulations, which tend to be quite noisy, and collisional effects could be easily seen in regimes where the collision rate was rather high. In reality, though, fast ignition will involve larger beam temperatures and much smaller beam-to-background plasma density ratios, unlike those parameters used in the simulations discussed previously. Ultimately, we would like to be able to characterize saturation features in this regime, such as filamentation, saturated magnetic field levels, net current, etc., for fast ignition relevant parameters. This will enable us to determine under what conditions we should care about instabilities at all.

Shown in Fig. **6.13** is the 2D geometry used to model the first of a series of four cases in LSP. The geometry consisted of a 40x40 c/ω_p grid, which is relatively larger than the simple cases modeled previously, and the usual resolution parameters of 31 cells per wavelength, 20

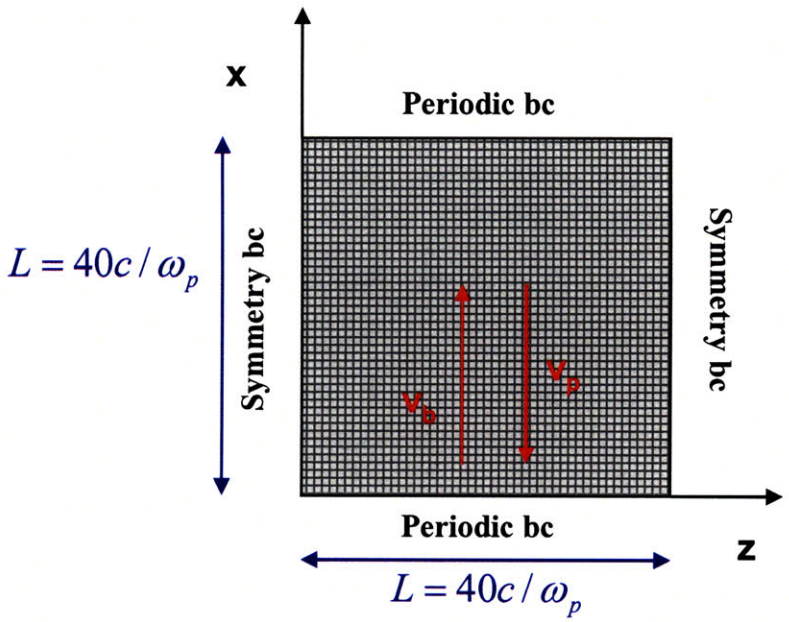

Fig.6.13. Schematic of the 2D simulation geometry used to model instability growth in LSP for fast ignition relevant parameters.

Case	Series 1 $\alpha = n_b/n_p = 0.1$	Series 2 $\alpha = n_b/n_p = 0.01$
A	T_b = 5keV; β_b = 0.94 (no collisions)	T_b = 5keV; β_b = 0.94 (no collisions)
B	T_b = 5keV; β_b = 0.94 (collisions)	T_b = 5keV; β_b = 0.94 (collisions)
C	T_b = 531keV; β_b = 0.76 (no collisions)	T_b = 531keV; β_b = 0.76 (no collisions)
D	T_b = 531keV; β_b = 0.76 (collisions)	T_b = 531keV; β_b = 0.76 (collisions)

Table 6.1. Overview of two series of four simulation cases to explore various saturation effects.

time-steps per plasma period, and 100 particles-per-cell were utilized. Because we are interested in a number of effects such as beam-to-plasma density ratio, beam temperature and drift, and collisions, we chose two series of simulation cases outlined in **Table 6.1**. The relatively cold, highly relativistic parameters of T_b = 5keV and β_b = 0.94 were chosen to be consistent with the equilibrium case studied in Chapter 5, while the Jüttner distribution with T_b = 531keV and β_b = 0.76 was chosen to be consistent with the parameters taken from the fit to the hot electron distribution in an explicit simulation of a laser-plasma interaction using the code Z3, which was discussed in detail in Chapter 5.

Shown in **Fig. 6.14** is a summary of the simulation results for each of the 4 cases of the first series ($\alpha = n_b/n_p = 0.1$) for comparison. On the left, the beam density has been plotted near the end of the linear growth regime at $\omega_p t = 50$ on a log scale for each of the 4 cases, while on the right, the same density has been plotted at various times of $\omega_p t = 200$, 500, and 1025 throughout the nonlinear saturated state on a linear scale. During the the linear regime, one can see the development of interwoven filaments in the colder cases A and B which are very similar in size and density with and without the inclusion of collisions. The slanted, woven nature of the filaments is characteristic of the 2D filamentary-two-stream mode; however, the filamentary instability can be seen to dominate simply from observing that the filaments are still mostly

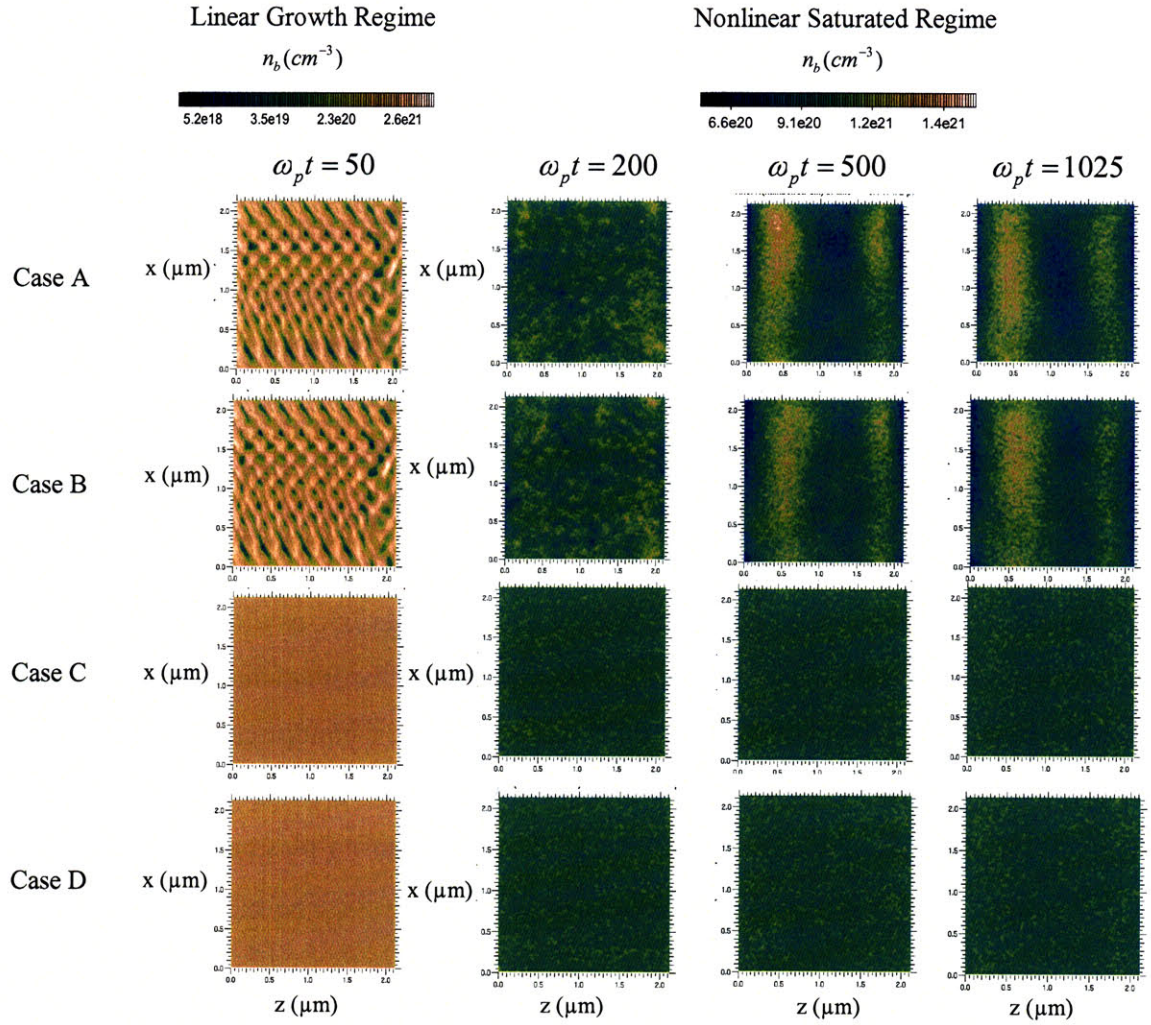

Fig.6.14. Summary of simulation results in the form of beam density during the linear (log scale) and nonlinear (linear scale) growth regimes for the first series of cases with $\alpha = 0.1$.

Case	B_{sat} (Gauss)	γ/ω_p
A	3.05×10^7	0.101
B	2.92×10^7	0.101
C	1.04×10^7	0.00002
D	1.05×10^7	0.0065

Table 6.2. Summary of saturated magnetic field and levels and filamentary growth rates for the first series of cases with $\alpha = 0.1$.

directed in the beam direction. In cases C and D, which consisted of much hotter beam parameters from the fit discussed in Chapter 5, this interwoven filamentary structure has virtually disappeared, with filamentation being only slightly observable. This is consistent with the relatively lower growth rates calculated in Chapter 5, as well as the saturated magnetic field amplitudes listed in **Table 6.2**. As one can see from the table, there is minimal difference between the saturated magnetic field amplitudes in the collisional and the collisionless cases, which was predicted in the previous section. The higher temperature cases C and D also have a reduced saturation level as a result of their lower growth rates.

As one looks later in time to the nonlinear saturated regime, one can see how the individual filaments eventually merge into larger filaments in case A and B. Early in time, the background plasma return current acts to surround each of the filaments in an effort to screen the local magnetic field. However, because this screening is not perfect, as time progresses, the attraction between the filaments becomes strong enough such that the filaments coalesce. This effect is obviously not as visible in cases C and D because the initial conditions were not sufficient to induce instability growth to any significant degree in the linear growth regime.

Thus far, we have examined simulations with an initial beam-to-plasma density ratio of $\alpha = n_b/n_p = 0.1$ due to higher expected growth rates well above the noise level in simulations that make growth rate extraction easier and instability features more easily observable. However, because the guiding cone that is to be inserted into fast ignition targets will allow the beam electrons to begin transport closer to the core at higher densities along the plasma corona, it is necessary to examine these same cases with smaller beam-to-plasma density ratios of $\alpha << 0.1$. A beam-to-plasma density ratio of $\alpha = 0.01$ was used for the second series of cases by simply increasing the background plasma density by an order of magnitude. Because explicit PIC algorithms require the plasma frequency and Debye length to be resolved and this restriction becomes expensive at high densities, the problem size was simply reduced such that the resolution was the same, but the grid dimensions of 40x40 c/ω_p were retained. Shown in **Fig. 6.15** is a summary of the results for the $\alpha = 0.01$ series similar to that of the $\alpha = 0.1$ series shown in **Fig. 6.14**. From a comparison of the two figures, one can see that the filamentation features are dramatically reduced in the $\alpha = 0.01$ series. One can still see the onset of growth of the 2D coupled filamentary-two-stream mode in the linear growth regime in the cold

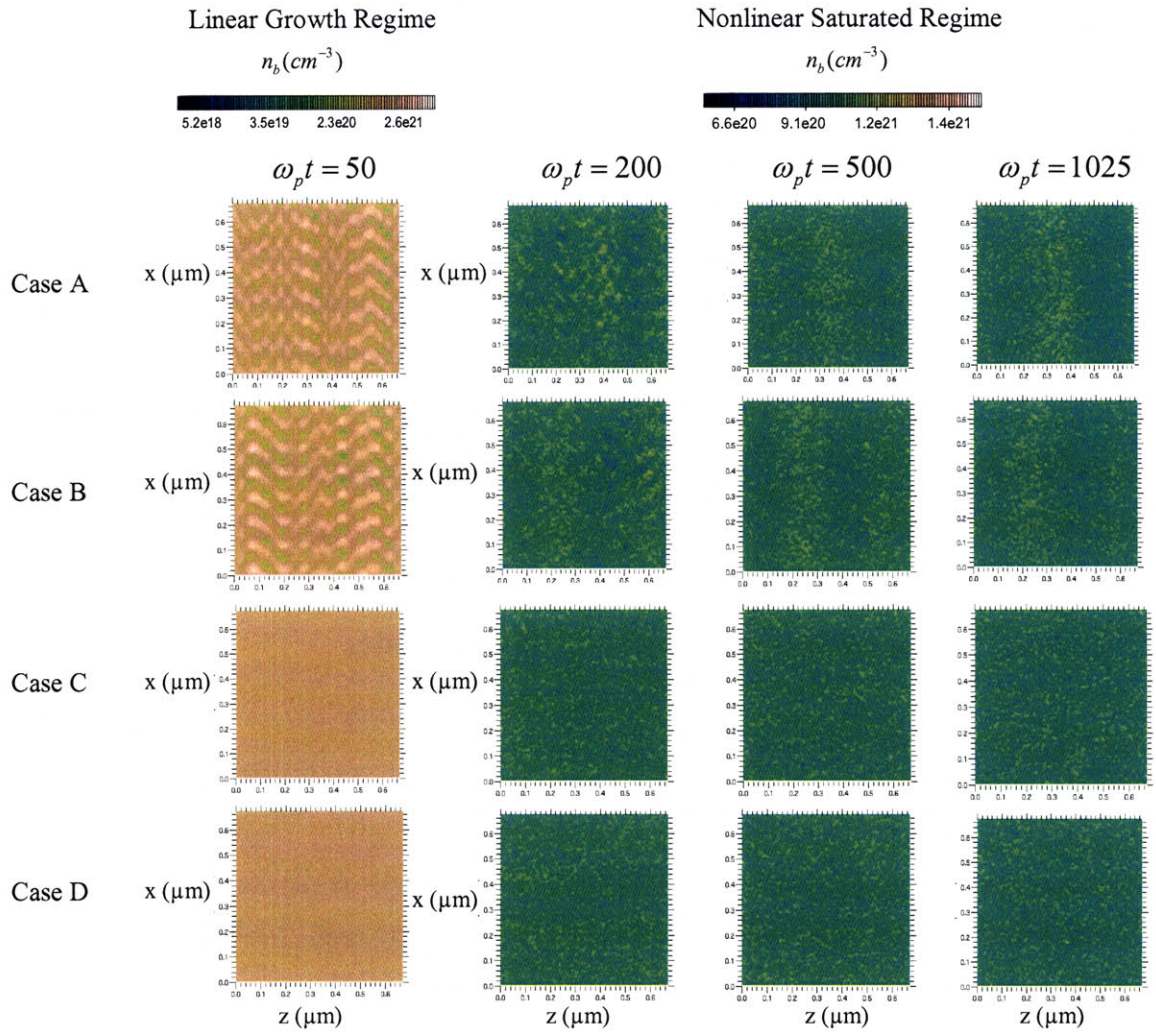

Fig.6.15. Summary of simulation results in the form of beam density during the linear (log scale) and nonlinear (linear scale) growth regimes for the series of cases with $\alpha = 0.01$.

Case	B_{sat} (Gauss)	γ/ω_p
A	1.02×10^7	0.0024
B	9.92×10^6	0.0051
C	3.30×10^6	0.00000064
D	3.13×10^6	0.000024

Table 6.3. Summary of saturated magnetic field levels for the series of cases with $\alpha = 0.01$.

temperature cases, A and B, though the filaments are noticeably less dense. This is to be expected due to the much lower growth rates for these parameters. In addition, the saturated magnetic field levels are approximately a factor of 3 lower than the $\alpha = 0.1$ case. As a result, filament features such as residual attraction and coalescence in the nonlinear regime are much less observable. The warmer cases, C and D, using the fit parameters reveal virtually no filamentation at all in the linear growth regime and subsequent nonlinear regime. This is also to be expected, as the growth rate is dramatically reduced for high temperatures and for $\alpha << 0.1$, as was confirmed by results in Chapter 5. Finally, it is worth mentioning that collisions appear to make little difference in either the filamentation or saturated magnetic field levels for either set of cases, which is in agreement with previous predictions.

6.5 Effects of Saturated Fields on Particle Orbits

One of the more obvious, yet uninvestigated features of interest for fast ignition is the orbits of hot electrons within the beam as instabilities evolve through the linear and well into the nonlinear regime. Although there have been many decades of research devoted to the investigation of beam instabilities, the effects on individual particle orbits has been more or less neglected. However, by examining the individual particle orbits, one can determine how the orbits are modified due to instability generated magnetic fields and how this will subsequently affect the particle stopping power. Ultimately, the question we would like to answer is how the effective particle range of the hot electrons changes due to instabilities.

The availability of large PIC codes capable of running on multiple processors has greatly facilitated the investigation of individual particle orbits. For the work relevant to this thesis, we made use of a convenient user option in the LSP code mentioned briefly in Chapter 4 that allows one to inject "tracer particles" within a given simulation at a specified momentum, position, and time. These tracer particles do not contribute or affect the electromagnetic fields in the simulation itself, but behave like test particles in that they only "feel" the effects of the fields. The tracer particles were injected into the simulation cases discussed in the previous section at the midpoint of the lower edge of the simulation box ($z = 1.105\mu m$, $x = 0$) and were tracked throughout the entire simulation. Because the hot electrons will be generated in a distribution containing a wide range of energies, we chose to inject particles at a relatively high

energy of $E_k = 1$ MeV and relatively low energy of $E_k = 1$ keV. I will only discuss results for the $\alpha = 0.1$ series, as these are sufficient for drawing the necessary conclusions of interest for this investigation.

It should be noted that the boundary conditions that have been specified will induce some bias into the particle orbits. As was mentioned previously, reflecting boundary conditions have been used longitudinally due to current problems within the parallel version of the code that prevent the use of periodic boundary conditions on both edges in parallel. Because these boundary conditions result in reflections along the longitudinal edges, the bias will be evident from some of the trajectories that follow. However, we can, in some ways, justify these boundaries and also learn a great deal from these results even though the conditions are not ideal. As will be shown, the magnetic fields reach such large values within and around the filaments that one can assume the particles will eventually get reflected at some point, even without the imposed reflection conditions at the boundary.

Shown in **Fig. 6.16** are the particle orbits for case A, the relatively cold ($T_b = 5$keV) collisionless case for the two energies mentioned above and have been plotted using two different aspect ratios in **Fig 6.16(a)** and **(b)**. While the large aspect ratio case (1:26) may be deceiving, it allows one to better observe the modification of the particle orbits by the instability generated magnetic fields. The second aspect ratio case (1:1) has been added for a better view of the actual particle range. The beam density and magnetic field have also been included in **Fig 6.16 (c)** and **(d)**, respectively, for reference. Because the linear growth regime is rather short, the magnetic field grows relatively fast and the combination of the saturated field and subsequent filament coalescence into larger filaments that produce larger magnetic fields has an almost immediate effect on the particle trajectories. As one can see from **Fig.6.16**, the tracer particles are initially dragged into the larger filaments formed in the nonlinear regime from filament coalescence. The higher energy particles ($E_k = 1$ MeV) do what one might refer to as "filament hopping." In other words, while they propagate in the beam direction, they also become temporarily trapped within the filaments by their magnetic field and rattle around inside the potential well with a clearly observable transverse motion. Eventually, the particles reach an opening (absence of a magnetic vortex) where the magnetic field is lower and they can escape the filament. However, they then become vulnerable to the magnetic field produced by a

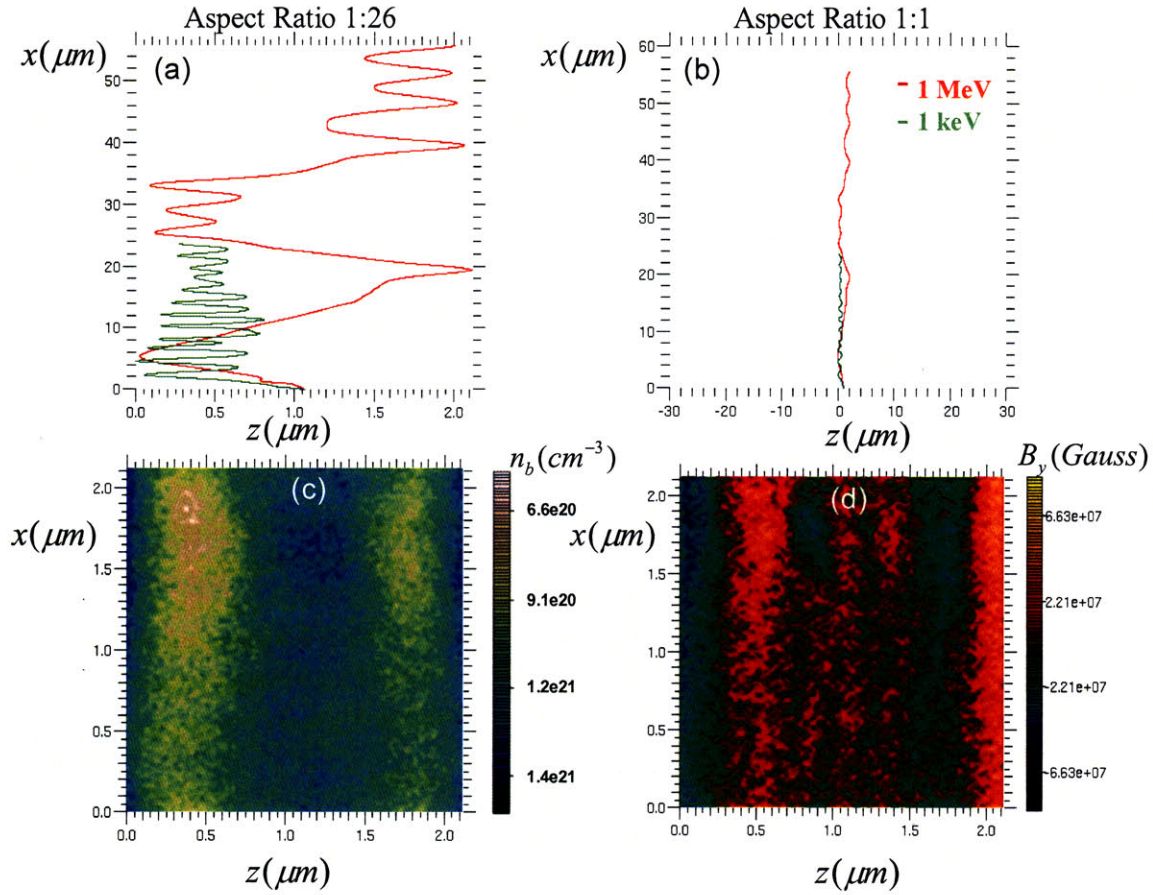

Fig.6.16. Particle orbits of tracer particles injected with energies of E_k = 1 MeV and 1keV for the collisionless case A (β_b = 0.94; T_b 5keV) plotted with an aspect ratio of 1:26 (a) and 1:1 (b) and the beam density (c) and magnetic field (d) at $\omega_p t$ = 500.

nearby filament and are then subsequently dragged into its potential well (hence, the description "filament hopping"). Unlike the higher energy electrons, the lower energy electrons (E_k = 1keV) appear to spend more time rattling around within the filaments due to insufficient energy to escape the magnetic field that confines them. In other words, lower energy particles tend to do less "filament hopping" than the higher energy particles based on this particular set of trajectories.

For the purposes of comparison, we also injected identical tracer particles into the same simulation which included collisions. Shown in **Fig. 6.17** is an equivalent plot of the orbits of the collisional case plotted with different aspect ratios. As one can see from the figure, the

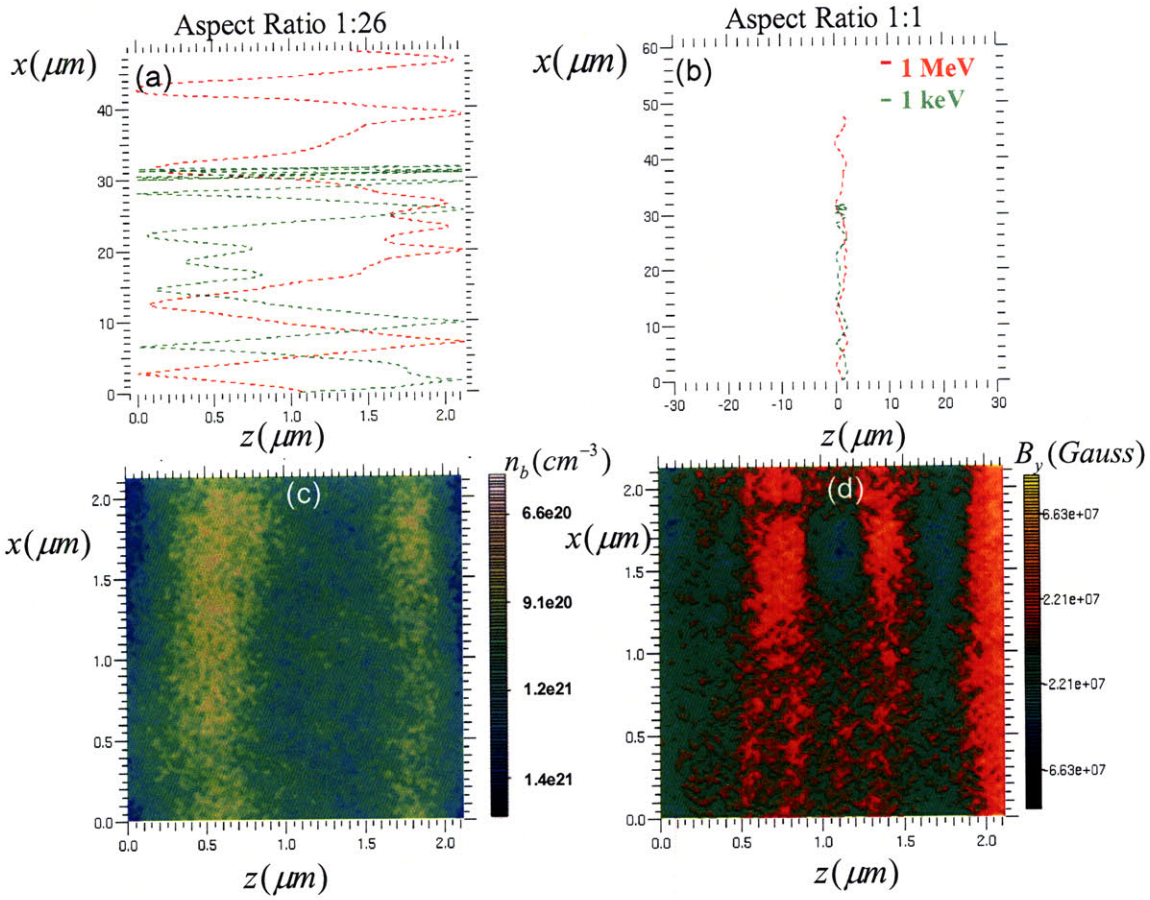

Fig.6.17. Particle orbits of tracer particles injected with energies of E_k = 1 MeV and 1keV for the collisional case B (β_b = 0.94; T_b 5keV) plotted with an aspect ratio of 1:26 (a) and 1:1 (b) and the beam density (c) and magnetic field (d) at $\omega_p t$ = 500.

orbits for the high energy particles (E_k = 1 MeV) are very similar to the high energy particles in the collisionless case, showing evidence of the same "filament hopping" phenomenon. This is to be expected, as collisions have little, if any, effect on electrons at this high of an energy. However, one does see differences in the low energy particle orbits for the collisional case. As one can see from **Fig. 6.17**, collisions create more transverse motion for particles of this energy, enabling them to scatter in and out of the potential well. For cases of quite low energy, such as E_k = 1keV, this actually appears to enhance filament hopping since particles of this energy are more likely to be effected by collisions and can scatter in and out of the filament, as opposed to simply being trapped inside it.

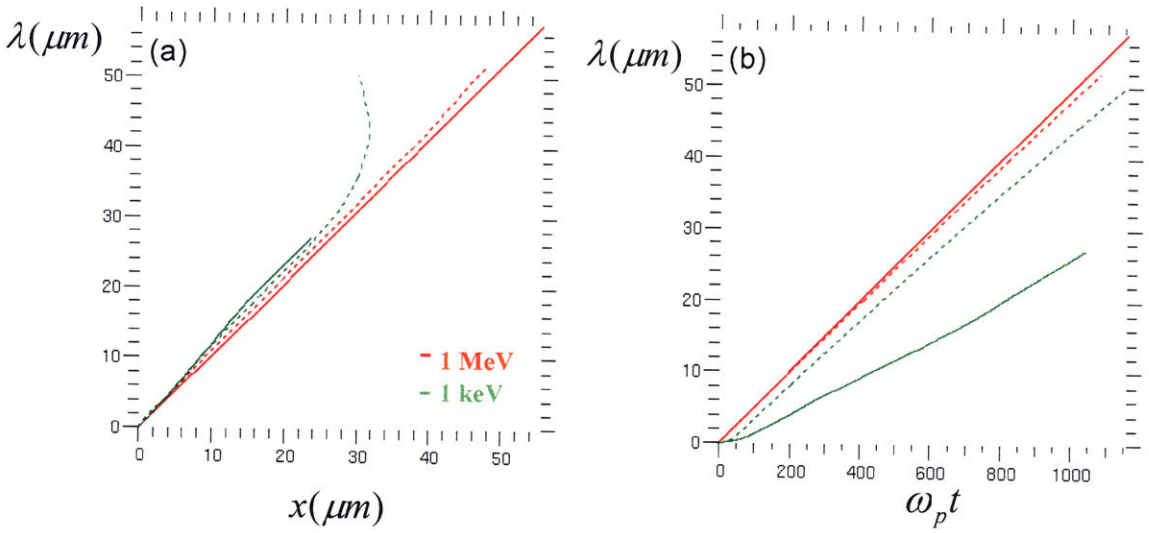

Fig.6.18. Path-length of particles for a range of energy injected into the collisionless case (solid line) and the collisional case (dotted line) plotted versus the vertical distance x (a) and versus time for cases A and B.

One can gain a little more perspective on these trajectories by computing the path-length as a function of both the vertical distance (x) and time. Shown in **Fig. 6.18** are plots of the path-lengths, λ, for both the collisional and collisionless simulations, cases A and B, for the same relatively cold cases discussed in the previous paragraphs. In **Fig. 6.18(a)**, the plot has been put on a scale such that the aspect ratio is 1:1 and a slope of 1.0 can be used as a reference. As one can see from the plot, high energy particles, both in the collisional and collisionless cases, have a slope that is very near 1.0, which is in agreement with the trajectory plots shown previously with a 1:1 aspect ratio that suggest that the particles have a relatively straight path. In other words, what we can deduce from this plot is that the instability generated magnetic fields have minimal effect on the overall range of high energy particles. On the other hand, as one starts to look at the lower energy particles, one begins to see a reduction in range. For the 1 keV cases, you see a factor of 2-3 reduction in range as particles are even seen to go in the reverse direction of the beam. The collisional enhancement of filament hopping discussed previously can even be seen from this plot by observing the relatively longer range and path-length of the 1 keV particle in the collisional simulation compared to the same case in the collisionless simulation. Also shown in **Fig. 6.18(b)** is the path-length as a function of time from which one can see more

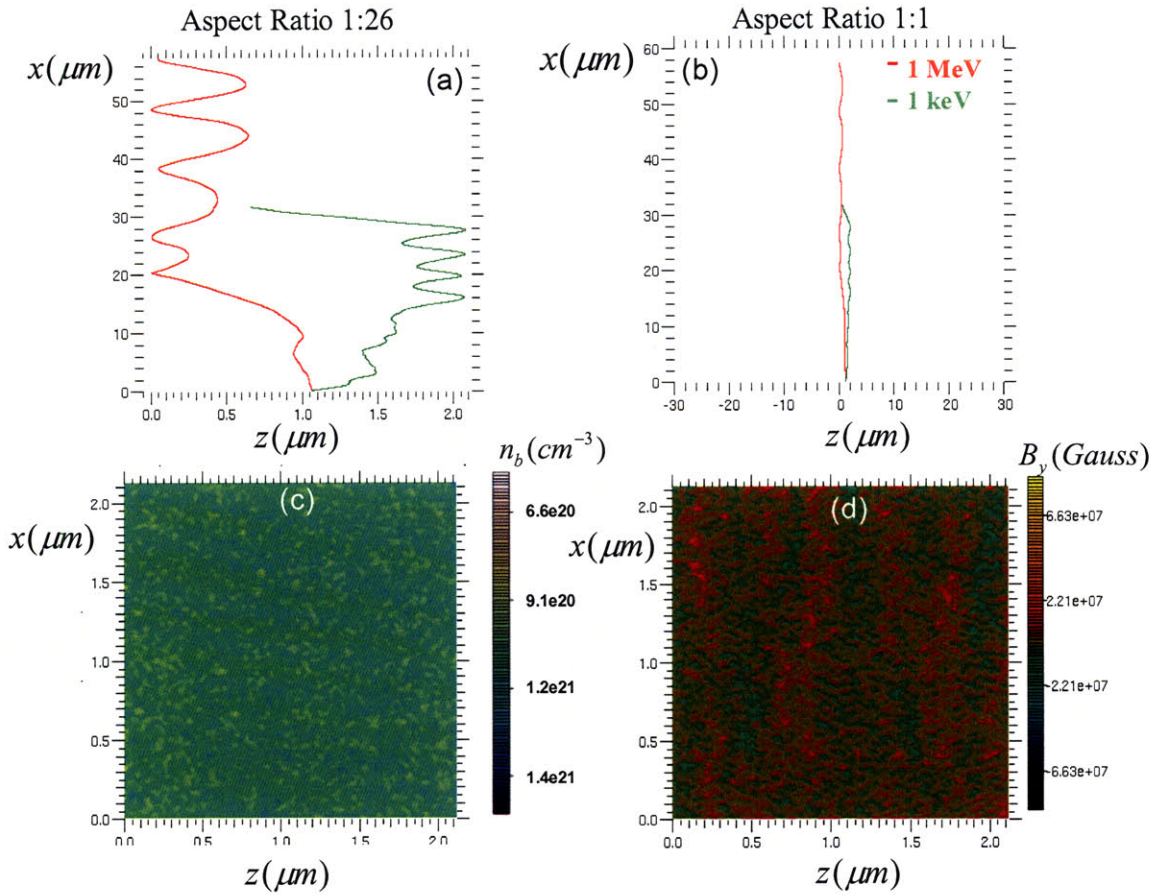

Fig.6.19. Particle orbits of tracer particles injected with energies of E_k = 1 MeV and 1keV for the collisionless case C (β_b = 0.76; T_b = 531keV) plotted with an aspect ratio of 1:26(a) and 1:1(b) and the beam density(c) and magnetic field(d) at $\omega_p t$ = 500.

clearly the overall effect of collisions. For high energy electrons, collisions have virtually no effect, but for low energy particles, the path-length becomes enhanced, as one would expect. A similar set of trajectories were also injected into simulation cases C and D using the relatively hotter fit parameters of (β_b = 0.76; T_b = 531 keV). Shown in **Fig. 6.19** are similar plots of the particle trajectories for the collisionless case C for aspect ratios of 1:26 and 1:1. Overall, one can see from these two plots similar features that were identified in the relatively colder cases, A and B, the only difference being that they have been reduced to some degree. For example, one can see in **Fig.6.19(a)** that the tracer particles are not immediately dragged into the filaments that coalesce due to the reduced saturated magnetic field level of the instability. Instead, they travel for a brief time in the initial direction of the beam before any substantial magnetic field effects occur that can alter their path. In addition, **Fig. 6.20(b)** indicates that the

orbits of higher energy particles are clearly straighter than in the cold case due to the reduced level of the instability generated magnetic field and filamentation. Although there is still some evidence of particle trapping and transverse motion within the minimal amount of filamentation that does exist, it is significantly reduced from that of the cold case, which can be seen most clearly by comparing **Figs. 6.16(b)** and **6.19(b)**. Furthermore, the transverse motion that does occur is on a larger scale due to the increased wavelength of the maximum growing mode at high temperature.

Like the previous set of cases, we injected a similar set of tracer particles into the collisional case D for the purposes of comparison. As one can see from **Fig.6.20**, the features are similar to the collisionless case C with relatively straighter paths due to reduced filamentation. Similar information can be gained from the path-length plots of the hot beam shown in **Fig.6.21**, as was done for the cold cases, for both the collisional and collisionless

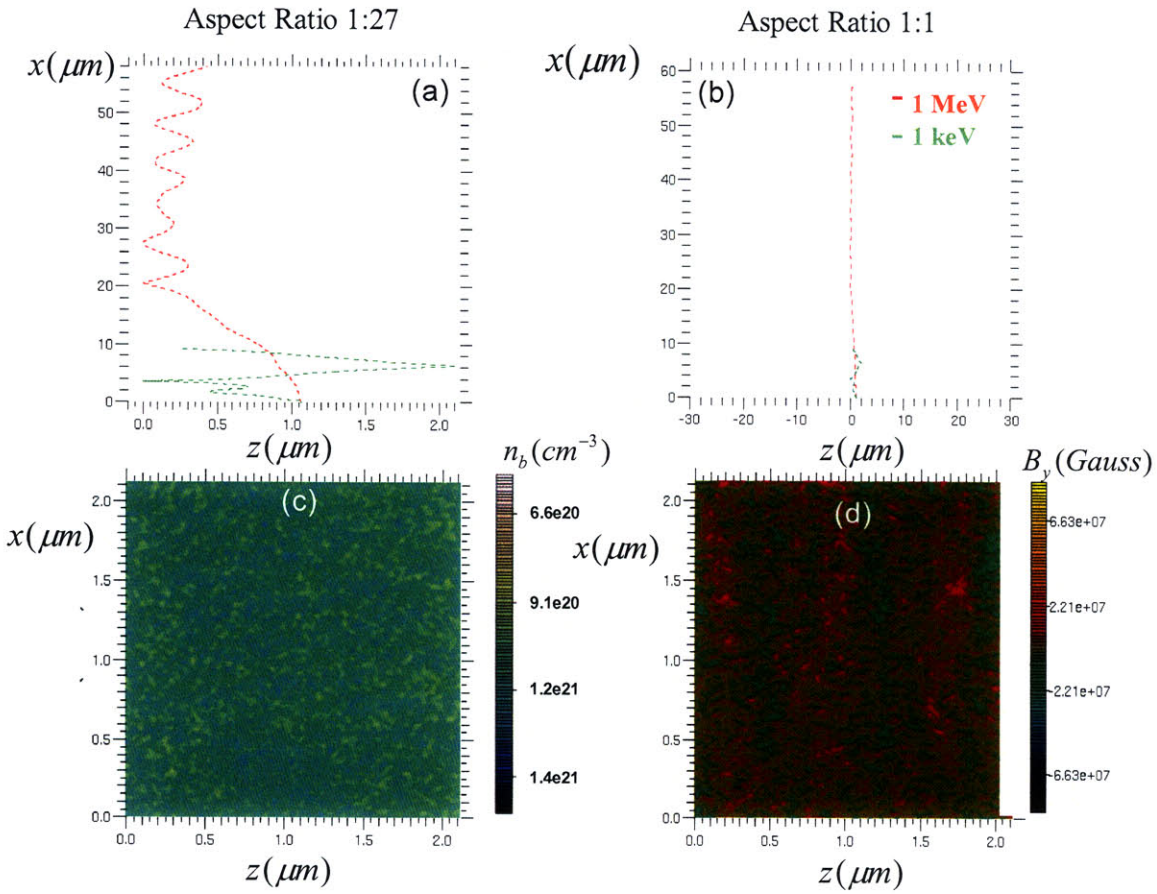

Fig.6.20. Particle orbits of tracer particles injected with energies of E_k = 3MeV, 1MeV, 100 keV, and 1keV for the collisional case D (β_b = 0.76; T_b 531keV) plotted with an aspect ratio of 1:27 (a) and 1:1 (b) and the beam density(c) and magnetic field(d) at $\omega_p t$ = 500.

simulations. What is immediately apparent from these plots is the increase in path-length compared to the cold case. In addition, the high energy particles have slopes very near 1.0, suggesting that the instability- generated magnetic fields have an insignificant effect on the particle range, even more so than the cold case discussed previously. However, what is interesting is the comparison of the 1keV cold cases with the 1keV hot cases with and without collisions. In the cold cases, the collisional range is greater than the collisionless range due to the ability of collisions to enhance "filament hopping" by scattering particles out of the potential well that would have otherwise been confined within the filaments, limiting their overall range. However, in the hot cases, the collisional range is actually less than the collisionless range. In these cases, there is less filamentation and lower magnetic fields, which result in less trapping, so collisions simply result in the usual meandering path for low energy electrons, while the collisionless trajectories are relatively straight.

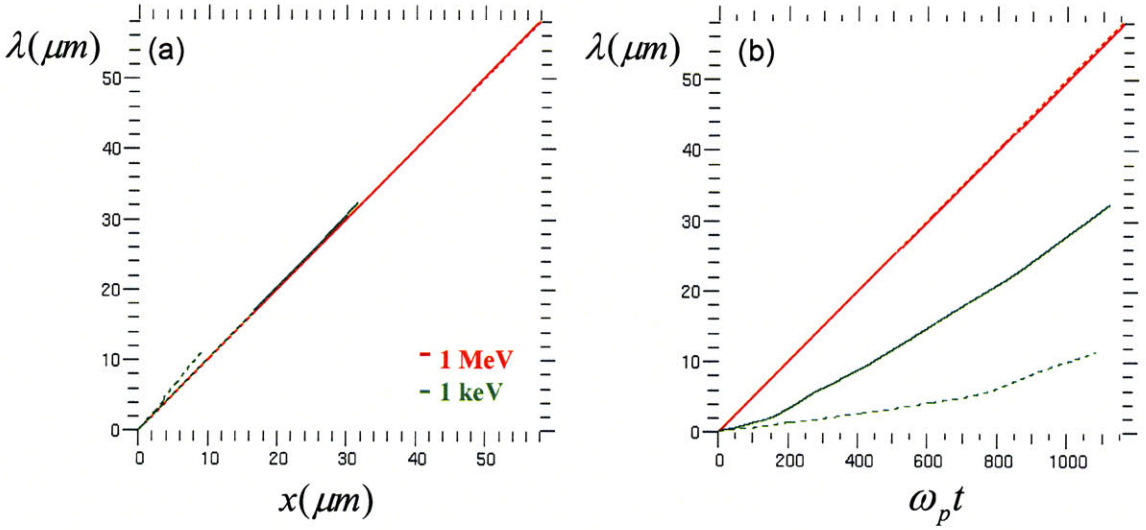

Fig.6.21. Path-length of particles for a range of energy injected into the collisionless case (solid line) and the collisional case (dotted line) plotted versus the vertical distance x (a) and versus time for cases C and D.

6.6 The Filament Hopping Phenomenon

In the previous section, it was shown that the hot electron trajectories for the chosen equilibrium models are, for the most part, relatively straight and electrons are guided along by the filaments that are produced. Furthermore, an interesting phenomenon was also observed in which electrons occasionally hopped between nearby filaments. For those particular simulations which modeled the longitudinal dimension of the beam and one of its transverse dimensions, we attributed this filament hopping phenomenon to a random process in which particles would escape the filament when they happened to reach an opening (absence of a magnetic vortex) where the magnetic field was lower and then became vulnerable to the magnetic field produced by a nearby filament. At that point, they are then subsequently dragged into its potential well. Although this is an accurate explanation for some hopping events, recent simulations of this beam-plasma equilibrium in the purely transverse direction also revealed filament hopping. This suggested that it is not a purely longitudinal effect associated with the wave-particle resonance

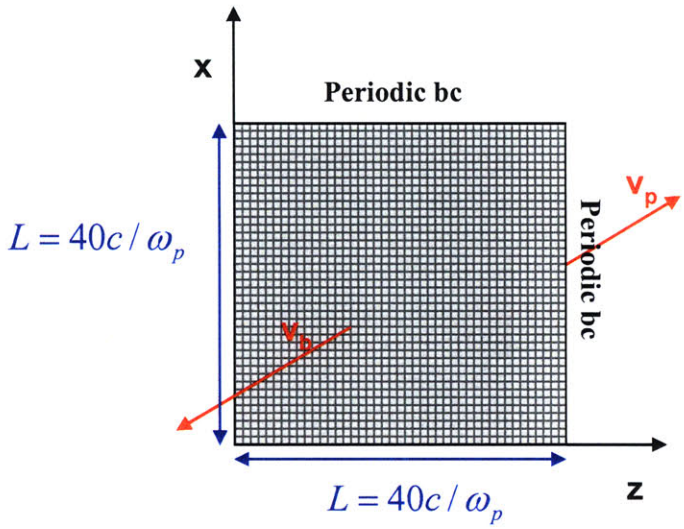

Fig. 6.22. Geometry of a transverse beam-plasma equilibrium simulation in LSP to illustrate filament hopping.

along the beam. As a result, we chose to investigate this phenomenon in more detail with purely transverse simulations.

Shown in **Fig. 6.22** is a schematic of the transverse simulation geometry used to model the same equilibrium beam-plasma problem discussed previously using LSP's explicit PIC scheme. The primary difference between this simulation and those discussed previously is that the beam drift is in the y-direction, as opposed to the x-direction. The same $40c/\omega_p$ x $40c/\omega_p$ simulation grid has been used in x and z directions with periodic boundary conditions on each edge. The relatively colder collisionless equilibrium case of T_b = 5keV, β_b = 0.94, and $\alpha = n_b/n_p$ = 0.1 has been used due to the increased filamentation and more clearly observable filament hopping events. The usual resolution parameters of 100 particles-per-cell, 20 time-steps per plasma period, and 31 cells per wavelength were used.

To better understand the mechanism behind the filament hopping phenomenon, we injected tracer particles with a directed energy of 1 MeV in the beam (y) direction in the center of the grid at (z = 1.06μm, x = 1.06 μm). As was mentioned previously, tracer particles do not contribute or affect the electromagnetic fields in the simulation itself, but behave like test particles in that they only "feel" the effects of the fields. Shown in **Fig. 6.23** are the results for this particular simulation. In **Fig. 6.23(a)**, the trajectory of a randomly chosen tracer particle has been plotted in black on the simulation grid with the initialization point highlighted by the red dot and two filament hops (A and B) highlighted with blue dots. The corresponding beam density has been plotted in **Fig. 6.23(b)**. As one can see from these two plots, the confined, overlapping circular lines of the trajectory will overlay exactly onto the filaments plotted in **Fig.6.23(b)**, which illustrates how the magnetic fields produced by the filaments (shown in **Figs. 6.23(c,d)**) act to confine the hot electrons. However, occasionally the particles do exit the filament, as shown in **Fig. 6.23(a)** by the hop from the filament at the far right to the one in the center (labeled as hop A) and then the hop from the filament at the center to the one at the bottom edge (labeled as hop B).

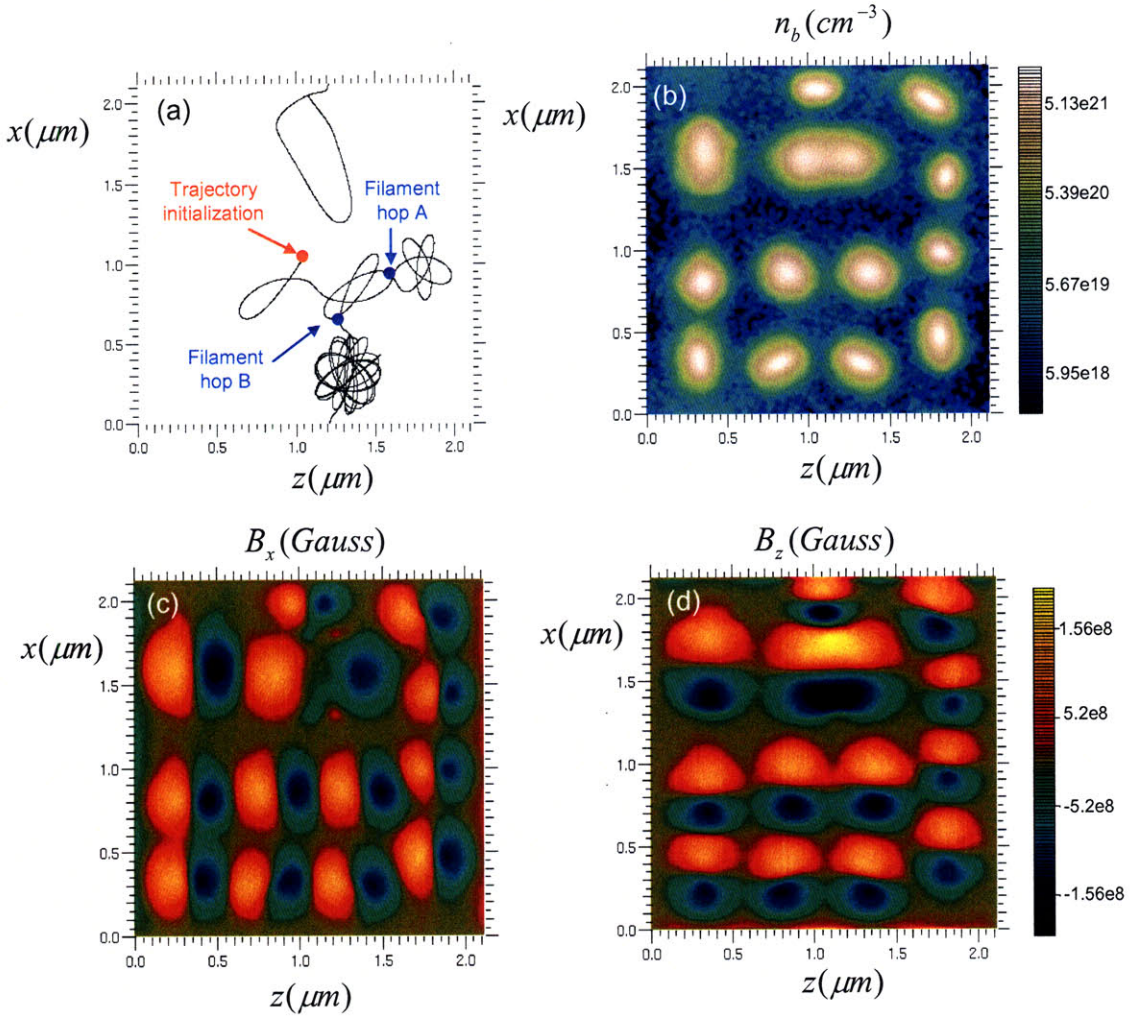

Fig.6.23. Trajectory of a 1 MeV tracer particle (a) and the beam density (b) and transverse magnetic fields (c,d) midway through the simulation at 750 $\omega_p t$.

To investigate more precisely what is causing these filament hopping events, it suffices to compute the electric and magnetic forces acting on this particular tracer particle in the transverse plane. Shown in **Fig. 6.24** are the x and z-direction electric and magnetic forces for each hopping event around the time that the particle relocates to a different filament. The electric forces, *FEx* and *FEz*, have been computed as $-qEx$ and $-qEz$, respectively, and the magnetic forces, *FBx* and *FBz*, have been computed as $-qv_y \, x \, Bz$ and $-qv_y \, x \, Bx$, respectively. For ease of viewing, forces in the x-direction have been plotted as solid lines and those in the z-direction have been plotted as dashed lines. It was determined from position data that hop A occurred between 712-714 $\omega_p t$ and hop B occurred between 773-775 $\omega_p t$. These time frames

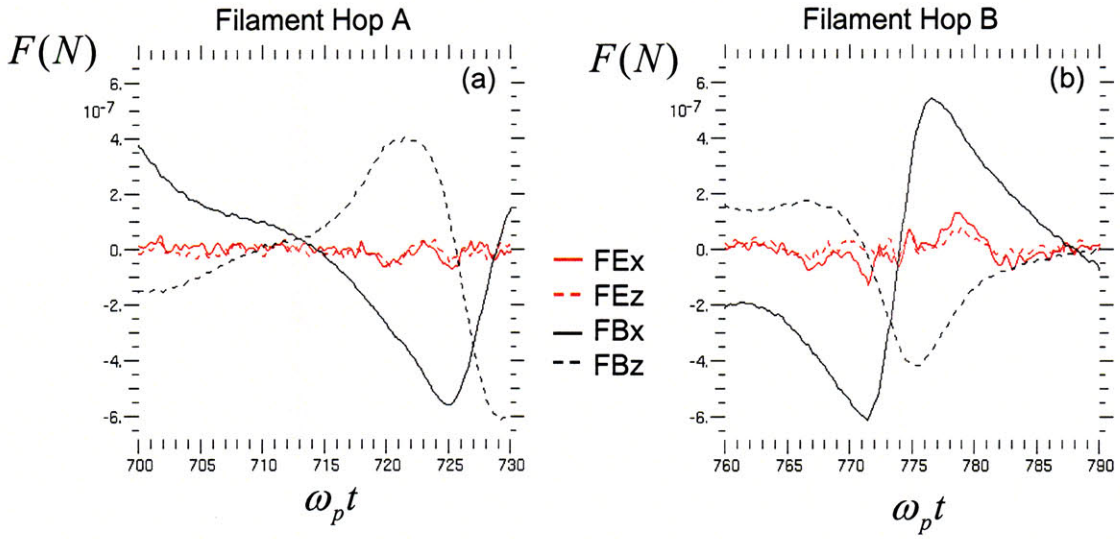

Fig.6.24. Summary of transverse electromagnetic forces acting on a 1 MeV tracer particle for filament hop A (a) and filament hop B (b) with the time frame of the hop shown in grey.

have been overlaid in grey in the figure. In general, the magnetic forces acting on the particle appear to be substantially larger than the electric forces. However, what is immediately obvious from this figure is that the hopping events occur at points of minimum force. More specifically, in **Fig. 6.24(a)**, the hop occurs in the z-direction so the forces of interest would be those plotted as dashed lines. Within the time frame of the grey region, these forces are at a minimum (near zero). A similar situation exists for hop B in **Fig. 6.24(b)**. This hop occurs in the x-direction so the forces of interest would be those plotted as solid lines, which are also at a minimum during the time frame of that the hop occurs.

In sum, we can conclude from these results that the filament hopping phenomenon is a random effect that can occur while a particle is guided along or confined by filaments. As it rattles around within the filament, it may find a point in space where the electromagnetic forces are relatively weak and allow it to escape the filament. However, because the magnetic forces of surrounding filaments are relatively strong, it becomes vulnerable to these forces and is quickly pulled into the potential well of a filament nearby where the process continues.

6.7 Conclusions

In sum, these results allow us to answer the ultimate question as to whether instabilities are of any concern for fast ignition. The simulations outlined in this section indicate that only relativistic beams that are born with a relatively low temperature will result in filamentation that will be of any concern. However, because the fit discussed in Chapter 5 contains a temperature much higher than this ($T_b \sim 531$ keV), filamentation will be virtually insignificant, even when the hot electrons are born in a region where the beam-to-plasma density ratio may be relatively large, i.e., $\alpha \sim 0.1$. Because this value of α is expected to be dramatically reduced due to the reduced transport distance created by the cone target, filamentation will be even less of a concern. Furthermore, the analysis of particle orbits suggests that even for the $\alpha = 0.1$ case, instability generated magnetic fields have minimal effect on particle orbits, suggesting that their path is relatively straight and their range is, for the most part, unaffected by instabilities. So one can assume from these results that instabilities can be safely neglected for most fast ignition conditions, especially in the high density region of the plasma corona. This is good news not only for fast ignition, but also for PIC modelers who would otherwise need to resolve these instabilities at great computational expense.

Chapter 7

Summary of Results and Concluding Remarks

Given the importance of relativistic electron transport for the fast ignition scenario, a complete understanding of the transport issues and possible hindrances is essential for evaluating the viability of this inertial confinement scheme. The goal of this thesis was to address these issues by investigating the three main phases of the electron transport process: hot electron generation in the cone and the extent of confinement along the cone surface, linear instability growth of the counter-streaming beam and plasma return current in the outer plasma corona, and the nonlinear saturated state of the counter-streaming beam and plasma return current in the inner plasma corona. Ultimately, the question we are interested in answering is how transport issues such as surface confinement and beam instabilities affect the efficiency of hot electron transport to the compressed fuel core.

Central to recent fast ignition target designs has been an embedded guiding cone into the usual spherical target, which has been included with the hope that it will keep a corridor open that is relatively free of coronal plasma during the fuel implosion and to also minimize the beam

propagation distance to avoid subsequent transport issues. Early work showed that this embedded cone also had the advantage that it could help to confine and guide electrons along its inner wall. However, the degree of this confinement and guiding has been a subject of debate in recent years as a result of a number of inconsistencies that have arisen in experimental and analytical results. Given the importance of this issue for target design purposes, we performed both integrated-explicit and hybrid-implicit PIC simulations of cone and slab geometries with laser parameters similar to early published results to investigate these inconsistencies. In sum, we have found that substantially fewer hot electrons (8-12%) are guided along the cone wall than what has been previously reported (50-100%), suggesting that surface confinement is only a minor effect. In doing so, we were able to link this discrepancy to the idea of "escaping electrons," which refers to significant differences in the measured (escaping) hot electron spectrum with respect to the original birth spectrum due to the generation of strong electrostatic self-fields. By characterizing the escaping distribution, rather than the distribution along the actual surface, we were able to achieve better agreement (~35%) with the experimental measurements of surface escape electrons. However, we did discover from simulations of different target geometries that the measured escape distribution outside of the target depends on the target shape, rather than the initial birth distribution. In fact, we found the surface fraction of escape electrons to be independent of the angular orientation of the initial birth distribution from injecting electrons isotropically within the target, along the target surface, and normal to the target surface. In sum, what these results suggest is that hot electron transport along the cone surface is only a minor effect and that the laser incidence angle is a minimal concern for design considerations. Furthermore, this result is significant for the characterization of experimental measurements in that the distribution that is measured is down-shifted in energy and significantly harder than the initial birth distribution.

During the second phase of hot electron transport in the outer plasma corona, the hot electron beam draws a return plasma current that establishes an approximately charge and current neutral equilibrium. During this equilibrium phase, the counter-streaming nature of this beam-plasma system makes it vulnerable to a number of micro-instabilities, namely, the two-stream, Weibel, and filamentary instabilities that inhibit transport. These instabilities will evolve through a linear growth phase, followed by a nonlinear saturated state. Because these states are intimately coupled, a thorough understanding of the linear growth regime was needed to

investigate the nonlinear regime. The goal of this thesis was to investigate the combined effects of the shape of the initial equilibrium distribution, as well as collisions, on these phases, neither of which have been examined in great detail. The specific form of the beam distribution has, for the most part, eluded researchers up to this time. Theoretical distributions whose temperature and drift parameters were loosely tied to those measured from experiments have been used for instability growth calculations, as well as computational modeling. However, this study has demonstrated that the structure of the distribution, as well as collisions, can strongly affect instability growth. We chose to examine how the instability growth rates depend on various assumed initial equilibrium distributions, each with varying degrees of analytical difficulty: the relativistic waterbag, the relativistic Maxwellian (Jöttner), and the low-temperature approximation to the relativistic Maxwellian (saddle-point approx.). We compared our results with a more physically based distribution obtained by fitting data from a 2D explicit PIC simulation which appeared to be best modeled with a Jöttner distribution. For all distributions of interest, collisions were found to have the ability to both suppress and enhance growth for the filamentary instability, while they only suppress growth for the two-stream instability. For the filamentary instability, collisions were found to create an unusual "kink" in the growth rate that forces the normally purely growing filamentary instability to transition to a growing/oscillating state, with the oscillation frequency increasing with K. For wave numbers less than the location of the kink, collisions appear to enhance growth, while for wave numbers greater than the location of the kink, collisions damp growth. Although collisions alone do not appear to be capable of damping the filamentary instability, an increase in beam temperature can achieve damping. Ultimately, what we wished to acquire from these calculations was the instability growth rates of the Jöttner distribution fit from the 2D explicit PIC simulation. Overall, we found that maximum growth appears to be dominated by the filamentary instability with finite collision frequency at low K ($K < 1$) and by the two-stream instability in the collisionless limit at high K ($K > 1$). However, the growth rates of both were, in general, very low due to the high temperature of the fit and were found to be dramatically reduced as the beam-to-plasma density ratio, $\alpha = n_b/n_p$, is reduced. The implications of this result are that the micro-scale instabilities in this regime do not need to be resolved for fast ignition considerations, which is very appealing for modelers utilizing the popular hybrid implicit schemes that are becoming more widely available. Finally, it should be noted that the LSP code demonstrated good agreement

with the growth rates calculated from analytical theory, giving an important vote of confidence for the code's extrapolation into the nonlinear regime.

The final phase of electron transport is, in many ways, the most important for fast ignition because it is this phase that will dictate how efficiently the hot electrons will transport the laser energy to the dense fuel core for ignition. Because the instability generated magnetic fields grow at a relatively rapid rate of the order of the plasma frequency before they finally saturate, they will have a significant influence on beam transport. It was determined from previous work that the process of magnetic trapping is responsible for saturating the magnetic fields following the linear growth stage. With this in mind, the goal of this work was to understand the effects of the parameters of the initial beam-plasma state (i.e., temperature, drift, background density) and collisions on magnetic trapping and the ensuing saturated magnetic field amplitude. In sum, our results allowed us to answer the ultimate question as to whether instabilities are of any concern for fast ignition. The simulations indicated that only relativistic beams that are born with a relatively low temperature will result in filamentation and magnetic field amplitudes that will be of any concern. Because the fit parameters taken from an explicit PIC simulation of the laser plasma interaction predict a temperature much higher than this ($T_b \sim$ 531 keV), filamentation will be virtually insignificant, even when the hot electrons are born in a region where the beam-to-plasma density ratio may be relatively large, i.e., $\alpha \sim 0.1$. Because this value of α is expected to be dramatically reduced due to the reduced transport distance created by the cone target, filamentation will be even less of a concern. Furthermore, the analysis of particle orbits suggested that even for the $\alpha \sim 0.1$ case, instability generated magnetic fields have minimal effect on particle orbits, suggesting that their path is relatively straight and their range is, for the most part, unaffected by instabilities. So we can assume from our results that instabilities can be safely neglected for fast ignition conditions, especially in the high density region of the plasma corona. This is good news not only for fast ignition, but also for PIC modelers who would otherwise need to resolve these instabilities at great computational expense.

Based on these results, PIC modelers have essentially been given the vote of confidence to continue using the popular hybrid-implicit PIC scheme, such as that utilized by LSP and is becoming more widely available, to model the fast ignition electron transport problem. Because this scheme utilizes larger temporal and spatial resolution, colder, more dense plasmas can be

modeled without great computational expense. In addition, the LSP code is continually being upgraded, the most recent improvements being the new collision model and a laser package that is still in the testing stages. With these capabilities, future work could include using LSP to perform fully-integrated modeling work of the laser-plasma interaction and hot electron transport to the high-density compressed fuel core.

Appendix A

Multi-dimensional Electromagnetic Explicit Particle-In-Cell Algorithm

The explicit algorithm utilized by LSP, also known as the leap-frog algorithm, consists of a 3D-3V electromagnetic scheme developed by Langdon and Lasinski for use in a code known as Zohar [75]. For simplicity, the 2 1/2-D scheme will be outlined in the paragraphs that follow. To begin, the electromagnetic fields are advanced using two of the standard Maxwell's equations

$$\frac{\partial \vec{B}}{\partial t} = -c\nabla \times \vec{E} \tag{A.1}$$

$$\frac{\partial \vec{E}}{\partial t} = c\nabla \times \vec{B} - 4\pi\vec{J} \tag{A.2}$$

The final two equations are not directly used in the advance but are satisfied through initial condition, i.e.,

$$\nabla \cdot \vec{E} = 4\pi\rho \tag{A.3}$$

$$\nabla \cdot \vec{B} = 0. \tag{A.4}$$

It is conventional for this scheme to separate the field components into independent modes consisting of the transverse electric mode, with components E_z, B_x, and B_y, and whose equations are expressed as

$$\frac{\partial B_x}{\partial t} = -\frac{\partial E_z}{\partial y} \tag{A.5}$$

$$\frac{\partial B_y}{\partial t} = \frac{\partial E_z}{\partial x} \tag{A.6}$$

$$\frac{\partial E_z}{\partial t} = \frac{\partial B_y}{\partial x} - \frac{\partial B_x}{\partial y} - J_z, \tag{A.7}$$

and the transverse magnetic mode, with components B_z, E_x, and E_y, whose equations are expressed as

$$\frac{\partial B_z}{\partial t} = -\left(\frac{\partial E_y}{\partial x} - \frac{\partial E_x}{\partial y}\right) \tag{A.8}$$

$$\frac{\partial E_x}{\partial t} = \frac{\partial B_z}{\partial y} - J_x \tag{A.9}$$

$$\frac{\partial E_y}{\partial t} = -\frac{\partial B_z}{\partial x} - \frac{\partial B_x}{\partial y} - J_y. \tag{A.10}$$

Finally, these transverse mode equations can be finite-differenced to form centered difference equations in both the time and space domain; namely,

TM mode:

$$\frac{B_{z_{i,j}}^{n+1/2} - B_{z_{i,j}}^{n-1/2}}{\Delta t} = -\frac{E_{y_{i+1/2,j}}^{n} - E_{y_{i-1/2,j}}^{n}}{\Delta x} + \frac{E_{x_{i,j+1/2}}^{n} - E_{x_{i,j-1/2}}^{n}}{\Delta y} \tag{A.11}$$

$$\frac{E_{x_i,j+1/2}^{n+1} - E_{x_i,j+1/2}^{n}}{\Delta t} = \frac{B_{i.j+1}^{n+1/2} - B_{z_{i,j}}^{n+1/2}}{\Delta y} - J_{x_{,j+1/2}} \tag{A.12}$$

$$\frac{E_{y_{i+1/2,j}}^{n+1} - E_{x_{i+1/2,j}}^{n}}{\Delta t} = -\frac{B_{z_{i+1,j}}^{n+1/2} - B_{z_{i,j}}^{n+1/2}}{\Delta x} - J_{y_{i+1/2,j}} \tag{A.13}$$

TE mode:

$$\frac{B^{n+1/2}_{x_{i+1/2,j+1/2}} - B^{n-1/2}_{x_{i+1/2,j+1/2}}}{\Delta t} = -\frac{E^{n}_{z_{i+1/2,j}} - E^{n}_{z_{i-1/2,i}}}{\Delta y} \tag{A.14}$$

$$\frac{B^{n+1/2}_{y_{i,j}} - B^{n-1/2}_{y_{i,j}}}{\Delta t} = \frac{E^{n}_{z_{i+1/2,j}} - E^{n}_{z_{i-1/2,j}}}{\Delta x} \tag{A.15}$$

$$\frac{E^{n+1}_{z_{i+1/2,j}} - E^{n}_{z_{i+1/2,j}}}{\Delta t} = \frac{B^{n+1/2}_{y_{i,j+1}} - B^{n+1/2}_{y_{i,j}}}{\Delta x} - \frac{B^{n+1/2}_{x_{i+1/2,j+1/2}} - B^{n+1/2}_{x_{i+1/2,j+1/2}} - B^{n+1/2}_{x_{i-1/2,j+1/2}}}{\Delta y} - J_{z_{i+1/2,j}} \tag{A.16}$$

The charge and current density are interpolated from the grid using particle positions and velocities with the common linear area weighting function described in Chapter 3, i.e.,

$$\rho_{n+1} = \sum_{s} q_s \sum_{p} S(\vec{X}_j - \vec{x}_{n+1}) \tag{A.17}$$

$$\vec{J}_{n+1/2} = \sum_{s} \frac{q_s}{2} \sum_{p} \vec{v}_{n+1/2} \left(S(\vec{X}_j - \vec{x}_n) + S(\vec{X}_j - \vec{x}_n) \right), \tag{A.18}$$

where j refers to the grid location, S refers to the shape factor or weighting function that relates the particle location to the spatial grid at X_j, and these quantities are summed over each of the particles, p, for a given species, s.

The final step consists of pushing the particles with fields interpolated from the grid. The scheme commonly used for advancing particles is referred to as the Boris Pusher [76]. The basic idea consists of first finite-differencing the relativistic equation of motion, i.e.,

$$\frac{p^{n+1/2} - p^{n-1/2}}{\Delta t} = \frac{q}{m} \left(E^n + \frac{1}{c} \frac{p^{n+1/2} + p^{n-1/2}}{2\gamma^n} \times B^n \right) \tag{A.19}$$

where

$$B^n = \frac{B^{n+1/2} - B^{n-1/2}}{2}. \tag{A.20}$$

The novelty of this scheme relies on splitting the momentum update into two electrostatic accelerations and an intermediate magnetic rotation. The electrostatic accelerations are defined by

$$p^- = p^{n-1/2} + \frac{\Delta t}{2}\frac{q}{m}E^n \tag{A.21}$$

$$p^{n+1/2} = p^+ + \frac{\Delta t}{2}\frac{q}{m}E^n \tag{A.22}$$

where

$$\left(p^+\right)^2 + (p^-)^2 = 0, \tag{A.23}$$

and after substitution, the full finite difference equation becomes

$$\frac{p^+ - p^-}{\Delta t} = \frac{q}{mc}\frac{p^+ - p^-}{2\gamma^n} \times B^n. \tag{A.24}$$

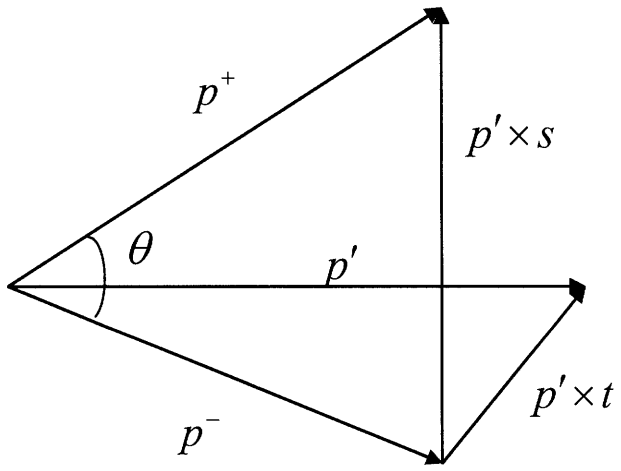

Fig. A.1. Vector diagram of variables used for the Boris pusher magnetic rotation [77].

The basic idea behind this method consists of first computing p^- from the old momentum and half the electric impulse. Then equation A.24 can be used to perform the rotation necessary for computing p^+. A common procedure for performing this rotation consists of using the vector diagram outlined above in **Fig.A.1**. As one can see from the diagram, an intermediate variable defined as p' is first computed, i.e.,

$$p' = p^- + p^- \times t \tag{A.25}$$

where t is the angle of rotation defined as

$$t = \frac{qB\Delta t}{2\gamma mc} = -\tan\frac{\theta}{2}. \tag{A.26}$$

With p', one can then compute p^+ from

$$p^+ = p^- + p' \times s, \tag{A.27}$$

where s is defined as

$$s = \frac{2t}{1+t^2} = 2\sin\frac{\theta}{2}\cos\frac{\theta}{2}. \tag{A.28}$$

Like all simulation algorithms, the explicit scheme is subject to nonphysical numerical instabilities that can are attributed to the use of finite differenced equations, rather than the full continuous partial differential equations. One can determine the numerical stability of the scheme by examining simple electromagnetic plane waves in vacuum [37]. For simplicity, the details of this calculation will be omitted, but the dispersion relation for the finite difference scheme in 2D leads to a well-known criteria known as the Courant condition[78] that is required for numerical stability, i.e.,

$$\frac{1}{c^2\Delta t^2} > \frac{1}{\Delta x^2} + \frac{1}{\Delta y^2}. \tag{A.29}$$

In essence, the Courant condition states that explicit schemes are limited to small time steps in order to ensure numerical stability [78].

Appendix B

Multi-dimensional Electromagnetic Implicit Particle-In-Cell Algorithm

LSP utilizes a 3D-3V direct implicit algorithm originally developed by Hewett and Langdon [79]. This scheme comprises the following finite-differenced field equations:

$$\vec{E}_{n+1} - \vec{E}_n = c\Delta t \nabla \times \vec{B}_{n+1/2} - 4\pi \vec{J}_{n+1/2} \tag{A.30}$$

$$\vec{B}_{n+1/2} - \vec{B}_{n-1/2} = -c\Delta t \nabla \times \vec{E}_n \tag{A.31}$$

$$\vec{B}_{n+1} - \vec{B}_{n+1/2} = -\frac{1}{2} c\Delta t \nabla \times \vec{E}_{n+1} \tag{A.32}$$

where

$$\vec{E}_n = \frac{1}{2}\left(\vec{E}_{n+1} + \vec{E}_{n-1}\right). \tag{A.33}$$

Like the explicit scheme, the charge and current density source terms can be expressed in terms of the particle weighting functions on the grid as

$$\rho_{n+1} = \sum_s q_s \sum_p S(\vec{X}_j - \vec{x}_{n+1}) \tag{A.34}$$

$$\vec{J}_{n+1/2} = \sum_s \frac{q_s}{2} \sum_p \vec{v}_{n+1/2} \left(S(\vec{X}_j - \vec{x}_n) + S(\vec{X}_j - \vec{x}_n)\right) \tag{A.35}$$

where j refers to the grid location, S refers to the shape factor or weighting function that relates the particle location to the spatial grid at X_j, and these quantities are summed over each of the particles, p, for a given species, s.

The particles are advanced by finite-differencing the equation of motion as

$$\vec{x}_{n+1} = \vec{x}_n + \Delta t \vec{\mathrm{v}}_{\mathrm{n}} \tag{A.36}$$

$$\vec{v}_{n+1/2} = \vec{v}_{n-1/2} + \Delta t\left[\vec{a}_n + \frac{1}{2}(\vec{v}_{n+1/2} + \vec{v}_{n-1/2}) \times \frac{q}{mc}\vec{B}_n(\vec{x}_n)\right] \tag{A.37}$$

where

$$\vec{a}_n = \frac{1}{2}\left(\vec{a}_{n-1} + \frac{q}{m}\vec{E}_{n+1}(\vec{x}_{n+1})\right) \tag{A.38}$$

and n refers to a specified time step.

The essence of the direct implicit method, as explained in Chapter 3, is to first push the particles assuming that the advanced electric field is zero, i.e., $\vec{E}_{n+1}(\vec{x}_{n+1}) = 0$. The advanced particle positions and velocities derived from this initial assumption are denoted with a tilde ($\tilde{}$) and are given as

$$\tilde{v} = \tilde{v}_{n-1/2} + \Delta t\left[\vec{a}_{n-1} + \frac{1}{2}(\tilde{v} + v_{n-1/2}) \times \frac{q}{mc}\vec{B}_n(\vec{x}_n)\right] \tag{A.39}$$

$$\tilde{x} = \tilde{x}_n + \Delta t\tilde{v} \,. \tag{A.40}$$

The source terms, $\tilde{\rho}$ and $\tilde{J}$, as well as the implicit susceptibility and magnetization tensors, are then recomputed at this new tilde level using the corresponding particle positions and velocities at this level, $\tilde{x}$ and $\tilde{v}$. The new electric field term, $\vec{E}_{n+1}$, remains to be determined and must be done iteratively using the ADI (alternating direct implicit) method that involves a large matrix

inversion. With the new electric field, the source terms can be recomputed at the advanced time step, leading to

$$\rho_{n+1} = \tilde{\rho} - \nabla \cdot \vec{\tilde{\chi}} \cdot \vec{E}_{n+1} \tag{A.41}$$

$$\vec{J}_{n+1/2} = \tilde{J} + \frac{1}{\Delta t} \vec{\tilde{\chi}} \cdot \vec{E}_{n+1} - c\nabla \times \vec{\tilde{\zeta}} \cdot \vec{E}_{n+1}, \tag{A.42}$$

where the implicit susceptibility tensor, $\vec{\tilde{\chi}}$, and the magnetization tensor, $\vec{\tilde{\zeta}}$, are derived respectively as

$$\vec{\tilde{\chi}}(X_j) = \sum_s \frac{q_s^2 \Delta t^2}{4m_s} \tilde{\rho}_s(\vec{X}_j)\left[\vec{I} + \vec{R}_s(\vec{X}_j)\right] \tag{A.43}$$

$$\vec{\tilde{\zeta}}(\vec{X}_j) = \sum_s \frac{q_s^2 \Delta t^2}{8m_s c} \vec{J}_s^+(\vec{X}_j) \times \left[\vec{I} + \vec{R}_s(\vec{X}_j)\right] \tag{A.44}$$

In these expressions, $\vec{I}$ refers to the identity matrix and $\vec{R}$ is a rotation created by the magnetic field. The details for these derivations have been omitted for brevity but can be found in reference [79]. Finally, the particles are then advanced a second time with correction terms, represented by

$$\delta\vec{v} = \frac{\Delta t}{2}\left[\frac{q}{m}\vec{E}_{n+1}(\vec{\tilde{x}}) + \delta\vec{v} \times \frac{q}{mc}\vec{B}_n(\vec{x}_n)\right] \tag{A.45}$$

$$\vec{x}_{n+1} = \vec{\tilde{x}} + \Delta t \delta\vec{v} \tag{A.46}$$

$$\vec{v}_{n+1/2} = \vec{\tilde{v}} + \delta\vec{v}\,. \tag{A.47}$$

It should be noted that the original developers of LSP chose to neglect the final magnetization term in the advanced current density, i.e.,

$$-c\nabla\times\vec{\vec{\zeta}}\cdot\vec{E}_{n+1}, \tag{A.48}$$

with the justification that it becomes small in high density regimes. However, in common simulations where this claim is not valid, whether it be in simple simulations or at plasma-vacuum boundaries, this can lead to appreciable error with spuriously large magnetic fields. A fix for this problem has yet to be implemented, but it is currently under investigation [80].

Appendix C

Loading of Particle Momentum Distributions

Theoretical distributions were loaded into the LSP code using a technique commonly referred to as the method of univariate inversion [81]. In order to apply this technique, the three dimensional distribution must either possess some type of symmetry and/or must be separable such that it can be reduced to a function of a single variable. Because of this restriction, it is convenient to first load distributions into the drifting frame of the relativistic beam, where the distributions are predominantly symmetric in one or more dimensions. The normalized momentum in the beam frame will be defined as $\tilde{u}'$ and the normalized momentum distribution function in this frame as $F(\tilde{u}')$. The basic idea behind this loading technique involves sampling from a given distribution by using its cumulative distribution function. By definition, the cumulative distribution function can be expressed as

$$P(u') = \int_0^{u'} d\tilde{u}' F(\tilde{u}'), \tag{A.49}$$

where $P(u')$ is the probability that a particle has a momentum between 0 and u'. Because this probability ranges between [0,1), one can first sample from a uniformly distributed distribution between [0,1) to randomly select a u'_r. This u'_r can then be reinserted into equation A.49 as

$$u'_r = \int_0^{u'} d\tilde{u}' F(\tilde{u}'). \tag{A.50}$$

This equation can then be solved for u' analytically or via interpolation on a grid ranging from 0 to some maximum value set for $\tilde{u}'$ [82].

A.C.1 Saddle Point Approximation

The normalized distribution of the saddle point approximation in the drift frame of the beam takes the rather simple form

$$F_b(u') = \frac{1}{\gamma_b m^3 c^3 \left(2\pi\gamma_b T_b^*\right)^{3/2}} e^{\frac{-1}{T_b^*}\left[\frac{u_x'^2+u_y'^2}{2\gamma_b}+\frac{u_y'^2}{2\gamma_b^3}\right]}. \tag{A.51}$$

Not only is this form separable, but it also takes a form similar to the non-relativistic Maxwellian, which has a cumulative distribution function that is easily computable analytically. The Cartesian components in the beam frame are then expressed as

$$u_x' = \sqrt{2\gamma_b T_b^*}\, InvErf\left[2u_{r,x}' - 1\right] \tag{A.52}$$

$$u_y' = \sqrt{2\gamma_b T_b^*}\, InvErf\left[2u_{r,y}' - 1\right] \tag{A.53}$$

$$u_z' = \sqrt{2\gamma_b^3 T_b^*}\, InvErf\left[2u_{r,z}' - 1\right] \tag{A.54}$$

where $u_{r,x}'$, $u_{r,y}'$, and $u_{r,z}'$ are random numbers between [0,1) sampled from a uniform distribution and *InvErf[ ]* is the standard inverse error function. Finally, transforming to the laboratory frame, these components become

$$u_x = \sqrt{2\gamma_b T_b^*}\, InvErf\left[2u_{r,x}' - 1\right] \tag{A.55}$$

$$u_y = \sqrt{2\gamma_b T_b^*}\, InvErf\left[2u_{r,y}' - 1\right] \tag{A.56}$$

$$u_z = \gamma_b\beta_b + \sqrt{2\gamma_b^3 T_b^*}\, InvErf\left[2u_{r,z}' - 1\right]. \tag{A.57}$$

A.C.2 Jüttner Distribution

The normalized distribution of the Jüttner distribution in the drift frame of the beam takes the form

$$F_b(u') = \frac{1}{4\pi m^4 c^2 \gamma_b T_b^* K_2(1/\gamma_b T_b^*)} e^{\frac{-1}{T_b^*}\sqrt{1+u'^2}}, \tag{A.58}$$

where $u' = \sqrt{u_x'^2 + u_y'^2 + u_z'^2}$ is the radial momentum. Because of the spherical symmetry in this frame, one can write the cumulative distribution function equivalent to equation A.50 as

$$u'_{r,r} = \frac{1}{\gamma_b T_b^* K_2(1/\gamma_b T_b^*)} \int_0^{u'} d\tilde{u}' \tilde{u}'^2 e^{\frac{-1}{\gamma_b T_b^*}\sqrt{1+\tilde{u}'^2}} \quad . \tag{A.59}$$

An analytical solution to this integral is rather difficult so it suffices to compute it numerically on a grid for interpolation. Ideally, the integral would extend from [0,∞); however, to provide for better efficiency, given the large number of particles to be loaded, one can choose a maximum cutoff value for the grid. There are a number of ways this cutoff can be chosen, but one simple way consists of first locating the peak value of the radial distribution, which occurs at

$$u'_p = \sqrt{2\gamma_b^2 T_b^{*2} + 2\gamma_b T_b^* \sqrt{1+\gamma_b^2 T_b^{*2}}} \quad . \tag{A.60}$$

Using the value of the radial distribution at the peak, $F(u'_p)$, one can then define the cutoff by the criteria

$$F(u'_{\max}) = 10^{-p} F(u'_p), \tag{A.61}$$

where p is a specified tolerance, such as 3. So in sum, the distribution can be sampled by choosing a random number between [0,1), interpolating on the grid of the integral of the radial distribution between [0,u_{max}), and finally using the trapezoidal rule to get a refined value for the radial momentum in the beam frame, u'_r. The orthogonal and azimuthal angles are sampled similarly by first sampling from a uniform distribution from [0,1) to get $u'_{r,\theta}$ and $u'_{r,\varphi}$. However, a scaling must then be applied to ensure that there is uniform distribution over a three dimensional sphere, i.e.,

$$u'_\theta = \cos^{-1}(2u'_{r,\theta} - 1) \tag{A.62}$$

$$u'_\varphi = 2\pi u'_{r,\varphi}. \tag{A.63}$$

Finally, the beam frame momentum components can be re-expressed in Cartesian coordinates as

$$u'_x = u'_r \sin u'_\theta \cos u'_\varphi \tag{A.64}$$

$$u'_y = u'_r \sin u'_\theta \sin u'_\varphi \tag{A.65}$$

$$u'_z = u'_r \cos u'_\theta , \tag{A.66}$$

and using the Lorentz transformation, the laboratory frame components are expressed as

$$u_x = u'_x \tag{A.67}$$

$$u_y = u'_y \tag{A.68}$$

$$u_z = \gamma_b (u'_z + \beta_b \sqrt{1 + u'^2_x + u'^2_y + u'^2_z}) . \tag{A.69}$$

A.C.3 Relativistic WaterBag Distribution

The normalized distribution of the relativistic waterbag distribution in the drift frame of the beam takes the form

$$F_b = \frac{3}{4\pi\gamma_b (\hat{\gamma}'^2 - 1)^{3/2} m^3 c^3} \Theta[\hat{\gamma}' - \gamma'] \tag{A.70}$$

where $\gamma' = \sqrt{1 + u'^2_x + u'^2_y + u'^2_z}$ and $\hat{\gamma}' = \sqrt{5\gamma_b T_b^* \frac{K_3(1/\gamma_b T_b^*)}{K_2(1/\gamma_b T_b^*)} + 1}$. One can greatly simplify the loading for this distribution function by recognizing that the in three dimensions, the distribution represents an ellipsoid with transverse symmetry in the x and z directions. Furthermore, the reduced 1D distribution function in the z-direction can be re-expressed as second degree polynomial, i.e.,

$$F(u_z) = const * u^2_{\perp m}, \quad u_{zl} \le u_z \le u_{zr} \tag{A.71}$$

where $u_{\perp m}$ is defined as the parabolic boundary of the distribution defined as

$$u_{\perp m} = \sqrt{\hat{\gamma}^2 + 2\beta_b \hat{\gamma} u_z - \frac{u_z^2}{\gamma_b^2} - 1}, \tag{A.72}$$

which extends from the left edge at

$$u_{zl} = \gamma_b \beta_b \hat{\gamma}' - \gamma_b \sqrt{\hat{\gamma}'^2 - 1} \tag{A.73}$$

and to the right edge at

$$u_{zr} = \gamma_b \beta_b \hat{\gamma}' - \gamma_b \sqrt{\hat{\gamma}'^2 - 1}\,. \tag{A.74}$$

So given these simplifications, one can first load the momentum in the z-direction and then load the transverse momenta in the x- and y-directions within a transverse disk.

To formulate the cumulative distribution function in the z-direction, a function must be derived that can be mapped to a uniformly distributed random number between [0,1). Because of the parabolic fall off in the z-direction, one can derive the function

$$F(\bar{u}_z) = \frac{3}{4}\left(1 - \bar{u}_z^2\right) \tag{A.75}$$

where $\bar{u}_z$ is the scaled momentum

$$\bar{u}_z = \frac{u_z - (u_{zr} - u_{zl})/2}{(u_{zr} - u_{zl})/2} \tag{A.76}$$

and

$$\int_{-1}^{1} d\bar{u}_z F(\bar{u}_z) = 1\,. \tag{A.77}$$

Finally, the cumulative distribution function can be expressed as

$$\hat{u}_{r,z} = \int_{-1}^{\bar{u}_z} d\bar{u}_z F(\bar{u}_z), \tag{A.78}$$

where $\hat{u}_{r,z}$ is a random number between [0,1). This expression results in the 3rd degree polynomial

$$\bar{u}_z^3 - 3\bar{u}_z + 2(2\hat{u}_z - 1) = 0\,, \tag{A.79}$$

which has only one physical root for $\bar{u}_z$. This root can be expressed in terms of an angular variables, i.e.,

$$\bar{u}_z = -\cos(\varphi/3) + \sqrt{3}\sin(\varphi/3), \tag{A.80}$$

where

$$\varphi \equiv ArcTan\left[-\hat{p}, \sqrt{1-\hat{p}^2}\right] \tag{A.81}$$

and

$$\hat{p} \equiv 2\hat{u}_z - 1. \tag{A.82}$$

With the z-direction momentum loaded, one can then load the x- and y-direction momenta uniformly into a disk with

$$\sqrt{u_x^2 + u_y^2} \le u_{\perp m}. \tag{A.83}$$

After choosing random numbers $\hat{u}_{r,r}$ and $\hat{u}_{r,\theta}$ from uniformly distributed distributions between [0,1), the x- and y-direction momenta can then be expressed as

$$u_x = u_{\perp m}\sqrt{\hat{u}_{r,r}}\cos(2\pi\hat{u}_{r,\theta}) \tag{A.84}$$

$$u_y = u_{\perp m}\sqrt{\hat{u}_{r,r}}\sin(2\pi\hat{u}_{r,\theta}) \tag{A.85}$$

and

$$u_{\perp m} = \sqrt{\hat{\gamma}^2 + 2\beta_b\hat{\gamma}u_z - \frac{u_z^2}{\gamma_b^2} - 1}. \tag{A.86}$$

Bibliography

[1] Energy Information Administration, International Total Primary Energy Production, 2004, http://www.eia.doe.gov/emeu/international/energyproduction.html.

[2] K. S. Krane, *Introductory Nuclear Physics* (John Wiley & Sons, New York, 1988).

[3] W. M. Stacey, *Fusion: An Introduction to the Physics and Technology of Magnetic Confinement Fusion* (John Wiley & Sons, New York, 1984).

[4] Atzeni and Meyer-ter-Vehn, *The Physics of Inertial Fusion* (Oxford University Press, Oxford, 2004).

[5] J. Nuckolls, L. Wood, A. Theissen, and G. Zimmerman, Nature 239, 139 (1972).

[6] J. Lindl, Phys. Plasmas 2, 3933 (1995).

[7] M. Tabak, J. Hammer, M. Glinsky, W. L. Kruer, S. C. Wilks, J. Woodworth, E. M. Campbell, and M. D. Perry, Phys. Plasmas 1, 1626 (1994).

[8] P. Gibbon, *Short Pulse Laser Interactions With Matter, An Introduction* (Imperial College Press, London, 2005).

[9] G. A. Mourou, C. P. J. Barty, and M. D. Perry, Physics Today 24, 398 (1998).

[10] D. Strickland and G. Mourou, Op. Commun, 56, 219 (1985).

[11] D. E. Spence, P. N. Kean, and W. Sibbell, Opt. Lett. 16, 42 (1991).

[12] S. C. Wilks et al., Phys. Plasmas, 8, 542 (2000).

[13] M. Allen, *Ion Acceleration from the Interaction of Ultra-Intense Lasers with Solid Foils*, Diss. Univ. of Cal., Berkeley, (2004).

[14] A. G. Litvak, Sov. Phys. JETP, 30, 344 (1970).

[15] C. E. Max et al., Phys. Rev. Lett., 33, 209 (1974).

[16] P. Sprangle et al., Phys. Rev. Lett., 67, 2021 (1987).

[17] A. E. Siegman, *Lasers* (University Science Books, Mill Valley, CA, 1986).

[18] E. A. Startsev and C. J. McKinstrie, Phys. Rev. E, 55, 7527 (1997).

[19] D. Bauer et al., Phys. Rev. Lett., 75, 4622 (1995).

[20] S. C. Wilks et al., Phys. Rev. Lett., 69, 1383 (1992).

[21] S. C. Wilks et al., IEEE Trans. Plasma Sci., 21, 120 (1993).

[22] M. D. Rosen, Pages 160-170 of E. M. Campbell (ed), *Femtosecond to Nanosecond High-Intensity Lasers and Applications*, Vol. 1229 (1990).

[23] G. J. Pert, Phys. Rev. E, 51, 4778 (1995).

[24] V. L. Ginzburg, *The Propogation of Electromagnetic Waves in Plasmas*, Pergamon Press, New York (1964).

[25] W. L. Kruer, *The Physics of Laser Plasma Interactions*, (Addison-Wesley, New York, 1988).

[26] F. Brunel, Phys. Rev. Lett., 59, 52 (1987).

[27] F. Brunel, Phys. Fluids, 31, 2714 (1988).

[28] P. Gibbon and A. R. Bell, Phys. Rev. Lett., 68, 1535 (1992).

[29] D. W. Forslund et al., Phys. Rev. Lett., 39, 284 (1997).

[30] F. N. Beg et al., Phys. Plasmas, 4, 447 (1997).

[31] A. R. Bell et al., Plasma Phys. Control, Fusion, 39, 653 (1997).

[32] E. S. Weibel, Phys. Rev. Lett. 2, 83 (1959).

[33] H. Alfvén, Phys. Rev., 55, 425 (1939).

[34] G. A. Askar'yan et al., JETP Letters, 60, 251 (1994).

[35] J. M. Dawson, Phys. Fluids, 5, 445 (1962).

[36] D. R. Welch et al., Nucl. Inst. Meth., Phys. Res. A 464, 134 (2001).

[37] C. K. Birdsall and A. B. Langdon, *Plasma Physics via Computer Simulation*, (Institute of Physics Publishing, Bristol, 1991).

[38] C. K. Birdsall and D. Fuss, J. Comput. Phys., 36, 1 (1980).

[39] Y. Sentoku, A. Kemp, M. Bakeman, R. Presura, T. Cowan, Bull. Am. Phys. Soc., 50, 139 (2005).

[40] T. Tajima, *Computational Plasma Physics: With Applications to Fusion and Astrophysics* (Addison-Wesley Publishing Company, Inc., Redwood City, 1989).

[41] B. I. Cohen et al., J. Comput. Phys., 46, 15 (1982).

[42] D. R. Welch, *Hybrid Implicit Algorithms for IPROP and LSP*, MRC/ABQ-R-1942 (1999).

[43] M. E. Jones et al., J. Comput. Phys., 123, 169 (1996).

[44] W. M. Manheimer et al., J. Comput. Phys., 138, 565 (1997).

[45] D. P. Grote (2008) [Discussion on Manheimer collision model] (Personal communication, 26 February 2008).

[46] B. I. Cohen et al., Phys. Plasmas, 13, 022705 (2006).

[47] T. Nakamura et al., Phys. Rev. Lett., 93, 265002 (2004).

[48] Y. T. Li et al., Phys. Rev. Lett., 96, 165003 (2006).

[49] H. Ruhl, *Introduction to Computational Methods in Many Body Physics* (Rinton Press, Princeton, New Jersey, 2005).

[50] E. Fill, Phys. of Plasmas, 12, 052704 (2005).

[51] E. S. Weibel, Phys. Rev. Lett. 2, 83 (1959).

[52] S. A. Bludman and K. M. Watson, Phys. Fluids 3, 747 (1960).

[53] K. Molvig, Phys. Rev. Lett. 35, 1504 (1975).

[54] P. H. Yoon and R. C. Davidson, Phys. Rev. A 35, 2718 (1987).

[55] F. Califano, F. Pegoraro, S. V. Bulanov, Phys. Rev. E 56, 963 (1997).

[56] A. Bret, M.-C. Firpo, C. Deutsch, Phys. Rev. E 70, 046401 (2004).

[57] L. Gremillet, D. Benisti, E. Lefebvre, A. Bret, Phys. Plasmas, 14, 04074 (2007).

[58] P. Norreys, R. Allott, R. J. Clarke, J. Collier, D. Neely, S. J. Rose, M. Zepf, M. Santala, A. R. Bell, K. Krushelnick, A. E. Dangor, N.C. Woolsey, R. G. Evans, H. Habara, T. Norimatsu, R. Kodama, Phys. Plasmas, 7, 3721 (2000).

[59] S.P. Hatchett, D. Clark, M. Tabak, R.E. Turner, C. Stoeckl, R.B. Stephens, H. Shiraga, K. Tanaka, *Hydrodynamics of conically guided fast ignition targets*,

Fusion Science and Technology, 49, 327 (2006).

[60] O. Buneman, Phys. Rev. 115, 503 (1959).

[61] F. N. Beg, A. R. Bell, A. E. Dangor, C. N. Danson, A. P. Fews, M. E. Glinsky, B. A. Hammel, P. Lee, P. A. Norreys, and M. Tatarakis, Phys. Plasmas 4, 447 (1997).

[62] P. L. Bhatnagar, E. P. Gross, M. Krook, Phys. Rev., 94, 511 (1954).

[63] P.C. Clemmow and J. P. Dougherty, *Electrodynamics of Particles and Plasmas*, (Perseus Books, New York, 1989) 311.

[64] F. Jüttner, Ann. Phys. 34, 856 (1911).

[65] C. Deutsch, A. Bret, M. –C. Firpo, P. Fromy, Phys. Rev. E, 72 026402 (2005).

[66] B. F. Lasinski, A. B. Langdon, B. C. McCandless, C. H. Still, M. Tabak, R. P. J. Town, Bull. Am. Phys. Soc., 50, 288 (2005).

[67] W. M. Manheimer, Phys. of Fluids, 14 579 (1971).

[68] R.C. Davidson, D. A. Hammer, I. Haber, and C. E. Wagner, Phys. of Plasmas, 15, 317 (1972).

[69] F. Califano, F. Pegoraro, S.V. Bulanov, A. Mangeney, PRE, 57, 7048 (1998).

[70] F. Califano, R. Prandi, F. Pegoraro, S.V. Bulanov, PRE, 58, 7837 (1998).

[71] F. Califano, F. Pegoraro, S.V. Bulanov, PRL, 84, 3602 (2000).

[72] F. Califano, N. Attico, F. Pegoraro, G. Bertin, S.V. Bulanov, PRL, 86, 5293 (2001).

[73] F. Califano, T. Cecchi, C. Chiuderi, Phys. of Plasmas, 9, 451 (2002).

[74] T. Okada and K. Ogawa, Phys. of Plasmas, 14, 072702 (2007).

[75] A. B. Langdon and B. F. Lasinski, Meth. Comput. Phys., *Electromagnetic and Relativistic Plasma Simulation Models*, Meth. Comput. Phys., 16, 327-366, B. Alder, S. Fernbach, M. Rotenberg, and J. Killeen, eds. (Academic, New York, 1976).

[76] J. P. Boris and R. Lee, J. Comput. Phys. 4, 552 (1969).

[77] C. Ren, *Introduction to Particle-in-Cell Method in Plasma Simulations*, High Energy Density Physics Summer School, University of California, Berkeley (2005).

[78] R. Courant, K. Friedrichs and H. Lewy, *Über die partiellen Differenzengleichungen der mathematischen Physik*, Mathematische Annalen, 100, no. 1, 32 (1928).

[79] D. W. Hewett and A. B. Langdon, J. Comput. Phys 72, 121 (1987).

[80] D. J. Larson, Memo to the PIC/LSP theory group, Lawrence Livermore National Laboratory, Livermore, CA, 28 May 2008.

[81] M. H. Kalos and P. A. Whitlock, Monte Carlo Methods (Wiley-Interscience, United States of America, 1986).

[82] S. M. Lund (2006) [Informal notes on the loading of the Jüttner, saddle point, and relativistic waterbag distributions] (Personal Communication, October 2006).